



Technische Universität München  
Fakultät für Physik

Abschlussarbeit im Masterstudiengang Physik

Comparison between measured radiation levels and FLUKA simulations at CHARM and in the LHC tunnel of P1-5 within the R2E project in Run 2

Vergleich zwischen gemessenen Strahlungswerten und FLUKA-Simulationen bei CHARM und im LHC-Tunnel von P1-5 innerhalb des R2E-Projekts in Run 2

Daniel Prelipcean

*Supervisor at CERN:* Dr. Giuseppe Lerner  
*Supervisor at TUM:* Apl. Prof. Dr. rer. nat. habil. Hubert Kroha

München, 25. Juli 2021



# Contents

<b>1</b>	<b>Introduction</b>	1
<b>2</b>	<b>The Large Hadron Collider</b>	3
2.1	The CERN accelerator complex	3
2.2	The Large Hadron Collider	5
2.3	LHC performance and operation	6
2.3.1	Luminosity	6
2.3.1.1	Beta function	7
2.3.1.2	Crossing angle	7
2.3.2	Center of mass energy	8
2.3.3	Operational cycles of the LHC	9
2.4	Beam loss mechanisms	10
2.4.1	Luminosity burn-off	11
2.4.2	Beam-residual gas interactions	11
2.4.3	Beam-machine interactions	11
2.4.4	Beam-beam effects	12
2.5	LHC luminosity achievements	12
2.6	Luminosity driven losses at the experimental interaction points	16
2.6.1	Long straight sections	16
2.6.2	Dispersion suppressor	18
2.6.3	Shielded alcoves	18
2.6.4	Arc region	19
<b>3</b>	<b>Radiation Effects on Electronics</b>	21
3.1	The radiation to electronics project at CERN	21
3.2	LHC availability and R2E performance	23
3.3	Radiation effects on electronics	23
3.3.1	Cumulative effects	24
3.3.1.1	Total ionizing dose	24
3.3.1.2	Displacement damage	25
3.3.2	Single-event effects	26
3.3.2.1	Particle fluence	27
3.3.2.2	High energy hadrons	28

3.3.2.3	Thermal energy neutrons . . . . .	30
3.3.2.4	R-factor . . . . .	30
3.3.2.5	Limitations . . . . .	31
<b>4</b>	<b>Monitoring and Calculation . . . . .</b>	<b>33</b>
4.1	The monitoring and calculation working group at CERN . . . . .	33
4.2	Radiation monitors employed at the LHC . . . . .	33
4.2.1	Beam loss monitors . . . . .	34
4.2.2	Radiation monitors . . . . .	35
4.2.3	Optical fibre sensor . . . . .	36
4.3	FLUKA simulations . . . . .	37
4.3.1	The Monte Carlo method for simulations of radiation-matter interactions . . . . .	37
4.3.2	FLUKA physics models and capabilities . . . . .	38
4.3.3	FLUKA usages . . . . .	39
4.3.4	Geometry construction tools . . . . .	40
4.3.5	Simulation uncertainties . . . . .	41
<b>5</b>	<b>CHARM Facility Simulations and Comparison with Data . . . . .</b>	<b>43</b>
5.1	The CHARM facility . . . . .	43
5.2	FLUKA simulation of the CHARM facility . . . . .	46
5.3	Similarities between CHARM and the accelerator environment at the LHC . . . . .	46
5.4	Radiation monitors calibration benchmarks . . . . .	46
5.4.1	Beam loss monitor benchmark . . . . .	46
5.4.2	RadMON benchmark . . . . .	49
5.4.2.1	Fluence results . . . . .	49
5.4.2.2	TID results with two-step simulation approach . . . . .	53
5.4.3	Optical fibre benchmark . . . . .	57
<b>6</b>	<b>LHC Environment Simulations and Comparison with Data . . . . .</b>	<b>61</b>
6.1	Radiation source - luminosity driven interaction points . . . . .	61
6.1.1	Second step simulations . . . . .	65
6.1.2	Particle distributions . . . . .	66
6.2	Selected time periods of LHC operation . . . . .	70
6.3	Measured data . . . . .	72
6.4	Total ionizing dose results . . . . .	74
6.4.1	Beam loss monitor benchmark . . . . .	74
6.4.1.1	Single step simulation: LSS + DS (half-cells 8+9) . . . . .	75
6.4.1.2	Two-step simulation approach: DS + ARC . . . . .	78
6.4.1.3	Joint simulations of LSS and DS . . . . .	79
6.4.2	Optical fibre benchmark . . . . .	82
6.4.3	RadMON RADFETs benchmark . . . . .	84

6.5	SEU induced effects in RadMONs results . . . . .	86
6.5.1	Shielded alcoves RadMONs benchmark . . . . .	89
6.5.2	Tunnel RadMONs benchmark . . . . .	89
6.6	Agreement levels for FLUKA radiation level specifications . . . . .	92
6.7	Uncertainties and limitations . . . . .	92
6.7.1	Integrated luminosity scaling . . . . .	93
6.7.2	Thermal neutron sensitivity . . . . .	93
6.7.3	Geometry mismodelling . . . . .	93
6.7.4	Approximations due to statistical convergence . . . . .	93
6.7.5	Energy deposition dependency on simulated material . . . . .	94
6.8	Discussion and future work . . . . .	95
<b>7</b>	<b>Conclusions</b> . . . . .	97
<b>A</b>	<b>Particle accelerators and colliders</b> . . . . .	99
A.1	Motivation . . . . .	99
A.2	Acceleration methods and the radio frequency cavity . . . . .	100
A.3	Relevant quantities in accelerator physics . . . . .	101
A.4	General features at circular colliders . . . . .	102
<b>B</b>	<b>LHC interaction regions and sources of radiation</b> . . . . .	105
B.1	IR4: Radio frequency system . . . . .	105
B.2	IR3 and IR7: Collimation systems . . . . .	105
B.3	IR6: Beam dump systems . . . . .	107
<b>C</b>	<b>Example of a request for radiation level studies</b> . . . . .	109
C.1	Quench protection system system . . . . .	109
<b>Bibliography</b>	. . . . .	111
<b>List of Abbreviations</b>	. . . . .	121



# Chapter 1

## Introduction

This thesis aims to benchmark the measured values of the radiation monitors employed at the European Organisation for Nuclear Research (CERN), focusing on the Large Hadron Collider (LHC), for Radiation to Electronics (R2E) applications with their simulated values using the FLUKA Monte Carlo code. In the following, a brief introduction of each chapter is provided. This work has been carried out in the context of the Radiation to Electronics (R2E) project and the Monitoring and Calculation Working Group (MCWG) in order to assess the level of agreement between the measured values with the simulation predictions, of particular importance in feasibility studies for future accelerators and radiation levels specifications in areas where measurement are not available. This thesis has been written such that each chapter can be read independently.

The LHC is the largest and most powerful accelerator in the world, hosted at CERN. The LHC generates very high energy collisions (up to  $\sqrt{s} = 14$  TeV in the center-of-mass frame) at the interaction points (IP), giving rise to very rare events, used to study the fundamental laws of nature. To generate the exotic events measured by the experiments, two particle beams (mostly protons) are accelerated in opposite directions in the LHC. The LHC and its characteristics are described in Chapter 2.

The LHC operation creates a complex radiation field not only inside the interaction region caverns, but also in the collider tunnels and the shielded alcoves. The experiments at the interaction points are exposed to a hostile environment. In particular, the integrated flux of high-energy hadrons in the multi-MeV range and above affects detector and accelerator electronic devices. Commercially off-the-shelf (COTS) are not always suitable, as they are not specifically designed or tested for such high radiation levels. The significant risk of electronics failures require the careful evaluation of the radiation levels and their effect on all electronics systems installed in the entire CERN accelerator complex. This together with the study and coordination of mitigation options represents the scope of the Radiation to Electronics (R2E) project described in Chapter 3.

A comprehensive overview of the radiation background distribution at the LHC has been achieved within R2E project in the monitoring and calculation working group (MCWG), described in Chapter 4. On one hand, the radiation levels are measured by deployed radiation monitors, and on the other hand, radiation levels and predictions for the radiation monitor values are estimated using particle transport code relying on Monte Carlo methods, in particular the FLUKA code. These simulations proved to be indispensable tools for mapping the complex radiation field in different regions of the LHC

machine. The predictions are cross-checked with the measured values provided by the online radiation monitoring system for the LHC machine and the experimental caverns. This benchmarking of the simulations with the measurements data is essential and represents the main scope of this work.

A facility that has been extensively employed for radiation benchmark studies is the CERN High Energy AcceleratoR Mixed-field (CHARM) facility described in Chapter 5. It can be used to test electronics in a radiation environment very similar to the various locations in the CERN accelerator complex. Owing to the medium geometry of the CHARM facility, it can be simulated in less computational time compared to the LHC. Considering the CHARM facility as a more controlled and better understood environment, it is used to quantify the systematic uncertainty of the radiation monitors in radiation fields similar to the LHC accelerator environment.

The main results are presented in Chapter 6, consisting of a comprehensive set of radiation monitors benchmarks for the tunnels and shielded alcoves on the right side of the interaction points IP1 (ATLAS detector) and IP5 (CMS detector). Detailed radiation composition spectra for several locations along the LHC tunnel are also provided. Considering the complexity and scale of the simulations as well as the variety of LHC operational parameters used for the measured data, the global agreement of a factor of 2 or much better for selected benchmarks is considered to be good.

# Chapter 2

## The Large Hadron Collider

This chapter showcases the technological marvel of the Large Hadron Collider (LHC) [1], the largest accelerator in the world and the last chain in the CERN Accelerator complex [2]. It accelerates particles in its two beams circulating in opposite directions and collides them at the centres of four experimental interaction points (IP): ATLAS (IP1) [3], ALICE (IP2) [4], CMS (IP5) [5] and LHCb (IP8) [6]. The other four insertion regions (IR) deal with acceleration (IR4), momentum and betatron cleaning (IR3, 7) and dump (IR6). The key figures of merit describing the accelerator are its center of mass energy designed up to an energy of 7 TeV for protons (however, in practice it has been used at a nominal energy of 6.5 TeV for Run 2) and delivered luminosity, almost  $200 \text{ fb}^{-1}$  since its operation to date.

### 2.1 The CERN accelerator complex

The CERN accelerator complex [2] (see Figure 2.1) consists of a succession of machines, experiments and accelerators with increasing beam energies by a factor of  $\approx 30$  at each step. To date, it is composed of eight accelerators, two decelerators, the transfer lines which interconnect them and various facilities hosting experiments covering topics within the fields of particle physics, nuclear physics (e.g. ISOLDE [7]) and antimatter (e.g. ALPHA [8]), among others. Part of them are built on the surface, but the largest ones (e.g. the LHC) have been constructed underground.

While a number of the accelerators only supply particles to the experiments (e.g. LHC), others are used also as injectors, accelerating particles for larger accelerators. Mostly, the operation of the CERN accelerator complex uses protons, albeit some runs are dedicated to ions of: lead (Pb), argon (Ar), or xenon (Xe) atoms.

To provide some key operational figures, a total approximative number of  $13 \cdot 10^{20}$  protons were accelerated within the complex during Run 2 (2015-2018), from which the LHC used less than 0.084% and achieved  $16 \cdot 10^{15}$  proton-proton collisions at 13 TeV. Most of these particles that enter the accelerator complex are delivered to the ISOLDE (61.45%) and nTOF [9] (14.30%) facilities. Approximately 14% of the particles are used for operating tests or are not suitable to be used (triggering beam dumps, losses, etc.) [10, 11].

At such high energies, only the loss of a little fraction of the beam particles could damage the accelerator

or the detector equipment, which is the focus of Chapter 3. Safe operation of the accelerators requires correct operation of several systems specially designed for machine protection. Some of them are aimed at monitoring the beam characteristics, such as beam size, beam position or beam lifetime.

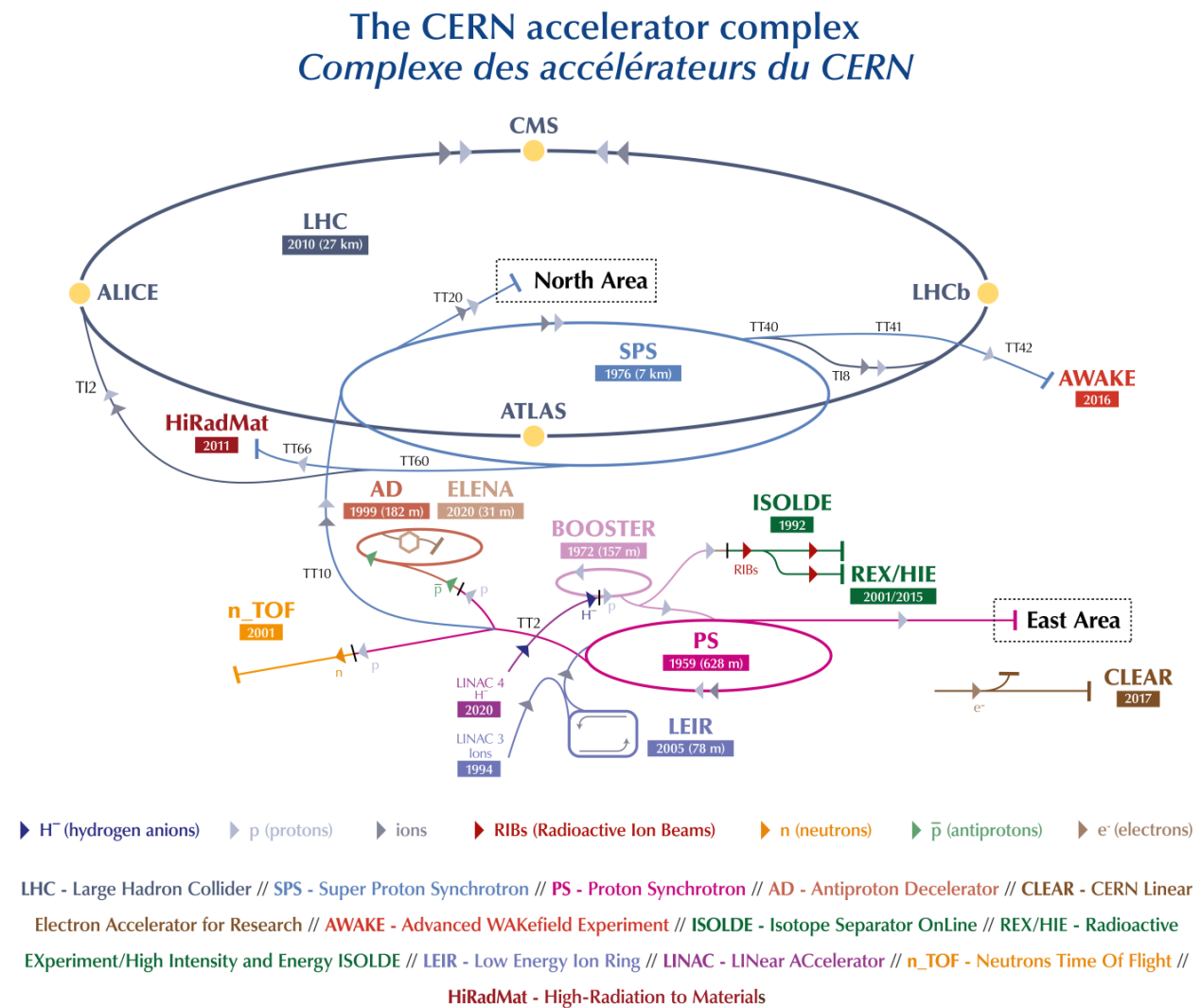


Figure 2.1: CERN accelerator complex [2]

## 2.2 The Large Hadron Collider

The LHC is a circular particle accelerator and collider, the largest in the world and the last stage in CERN's accelerator complex. The LHC beamline was built in the already existing tunnel of the large electron-positron (LEP) accelerator [12], with a fixed circumference of 26 658.883 m. LHC can accelerate particles up to a design energy of 7 TeV, which corresponds to 99.999 99 64 % of the speed of light, before directing them into collision.

The LHC accelerator layout (see Figure 2.2) can be divided based on the 8 insertion regions (IR) into octants [1]. An octant starts in the centre of an arc and continues to the centre of the next arc clockwise. Therefore, the IR corresponds to the middle of the octant where it is located. IR1 lies within Octant 1, and it corresponds to the interaction point (IP) of the ATLAS experiment. The rest of the IRs and octants are numbered from 1 to 8 following the direction of beam 1 (clockwise). The octants can be further divided into: (i) the long-straight-sections (LSS), which neighbour the insertion region and is responsible of guiding the beam into collision for the interaction points or to perform momentum cleaning, acceleration or dump; (ii) the dispersion suppressor (DS), that hosts the first curved portion of the accelerator next to the LSS leading into the (iii) ARCs, defined as the part of the ring occupied by 23 regular beamline elements called arc half-cells. The LHC arc cell has been designed to optimize the maximum integrated dipole field along the LHC arc using the minimum number of magnet interconnections.

The main functions of the LHC are performed by the following elements:

**Injection** from the SPS is performed via two transmission lines.

**Acceleration** is done in IR4 with the utilisation of radio-frequency (RF) cavities that provide longitudinal focusing of the particles in bunches and acceleration.

**Colliding** is carried out at the centre of four experiments: ATLAS (IP1), ALICE (IP2), CMS (IP5) and LHCb (IP8).

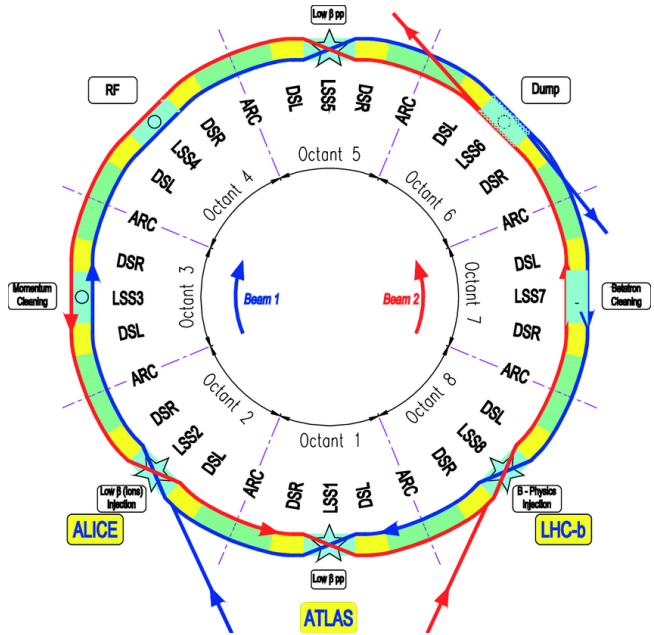


Figure 2.2: LHC Layout. Beam 1 and 2 are indicated in blue and red respectively. The collision points are indicated with stars. Beam 1 (blue line) is injected upstream of IP2 (TI2) and beam 2 (red line) upstream of IP8 (TI8). [1]

**Collimation** is performed in both IR3 and IR7. In IR3 the beams are cleaned with respect to too large longitudinal oscillation amplitudes (momentum cleaning), whereas in IR7 with respect to too large transverse oscillation amplitudes (betatron cleaning).

**Extraction** is realised in IR6. Due to the amount of energy stored in the beams, the LHC needs to have a dedicated beam abort system in order to dispose the beams in a safe manner. Each ring has their own extraction system – fast rising extraction magnets direct the beams into dedicated lines with massive dump blocks at the end where the beams are absorbed.

**Bending** is achieved by 8.3 T superconducting dipoles in the arcs and, in addition to just curving the beam, it is also necessary to perform **focusing** by quadrupoles, because protons are electrically charged and the particle beam diverges if left on its own.

## 2.3 LHC performance and operation

The basic working principles of an accelerator are described in more detail in Appendix Chapter A, while here the concepts of interest for this thesis are summarised.

Luminosity and the center of mass energy are the two key figures of merit at a particle collider. In order to explore new physics, one attempts to observe rare events (i.e. with small branching ratios) involving potentially heavy new particles. While the center of mass energy is the limiting factor the mass of the produced particles, the luminosity determines the collision rate, and hence, the available statistics for a given period of time.

### 2.3.1 Luminosity

As observing more events per time increases the statistical significance of rare events, the integrated luminosity delivered to the experimental interaction points is considered the key figure of merit for the performance of a collider. The luminosity  $\mathcal{L}$  is defined as the ratio of the number of detected events  $N$  in a certain time  $t$  to the interaction cross-section  $\sigma$ :

$$\mathcal{L} = \frac{1}{\sigma} \frac{dN}{dt} \quad (2.1)$$

The integrated luminosity is then the integral of the luminosity with respect to time:

$$\mathcal{L}_{int} = \int \mathcal{L} dt \quad (2.2)$$

which is measured in barns (symbol:  $b$ ), a metric unit of area equal to  $10^{-28} \text{ m}^2$  ( $100 \text{ fm}^2$ ). It is used in all fields of high energy physics to express the cross sections of scattering processes, and is best

understood as a measure of the probability of interaction between particles. A barn  $b$  is approximately the cross-sectional area of a uranium nucleus.

For the case of LHC, the proton-proton cross section in bunch collisions is estimated to be  $\sigma_{pp_{inel}} = 79.3 \pm 0.6$  (exp.)  $\pm 1.3$  (lum.)  $\pm 2.5$  (extrap.) mb [13]. For practical applications like this thesis, it is approximated to 80 mb.

There are a couple of accelerator physics parameters, which have an impact on the delivered luminosity. Within our scope, we shall only recall a selection below:

### 2.3.1.1 Beta function

The motion of the particle bunches in the transverse planes is dominated by magnetic fields. Their equation of motion along the circular path of the accelerator can be solved using the *linear optics approximation*, keeping only the dipolar and quadrupolar terms, for which a summary is given in Ref. [14]. Within this treatment, one defines a beta function  $\beta(s)$  as a function related to the transverse beam size  $\sigma(s)$  of the particle beam at the location  $s$  along the nominal beam trajectory via:

$$\sigma(s) = \sqrt{\epsilon \cdot \beta(s)} \quad (2.3)$$

where  $\epsilon$  is the root mean square (RMS) geometrical beam emittance, which is normally constant along the trajectory when there is no acceleration, and the beam is assumed to have a Gaussian shape such that  $\sigma(s)$  is its normal width.

The value of the beta function at an interaction point (IP) is then referred to as  $\beta^*$  ("beta star"). Usually, the beta function is adjusted such that it has a local minimum at these IP in order to minimize the beam size, which will maximise the interaction rate. The aperture of the beam line elements (e.g. the focusing magnets) around the IP limit in practice how small  $\beta^*$  can be actually adjusted to. The analytical calculations [14] yield an inverse linear relationship between the integrated luminosity  $\mathcal{L}_{int}$  and beta star  $\beta^*$  as:

$$\mathcal{L}_{int}(\beta^*) \approx \frac{1}{\beta^*} \quad (2.4)$$

### 2.3.1.2 Crossing angle

In colliders with many particle bunches, it is necessary to collide the beams at a crossing angle  $\alpha$  in between them in order to avoid unwanted collisions outside of the nominal collision points (see Figure 2.3). The transverse plane in which the crossing angle is applied is commonly designated as the crossing plane and the perpendicular one is referred to as the separation plane.

The ratio of the luminosity under a crossing angle  $\mathcal{L}_{xing}$  to the luminosity without  $\mathcal{L}_0$  it is called the

geometric factor:

$$\mathcal{F} = \frac{\mathcal{L}_{xing}}{\mathcal{L}_0} \approx \left( 1 + \alpha^2 \frac{\sigma_{s,1}^2 + \sigma_{s,2}^2}{\sigma_{xing,1}^2 + \sigma_{xing,2}^2} \right)^{-0.5} \quad (2.5)$$

with the assumptions that the crossing angle is small ( $2\alpha \ll 1$ ) and the bunch lengths  $\sigma_{s,i}$  largely exceeds the transverse beam size  $\sigma_{xing,i} \ll \sigma_{s,i}$ .

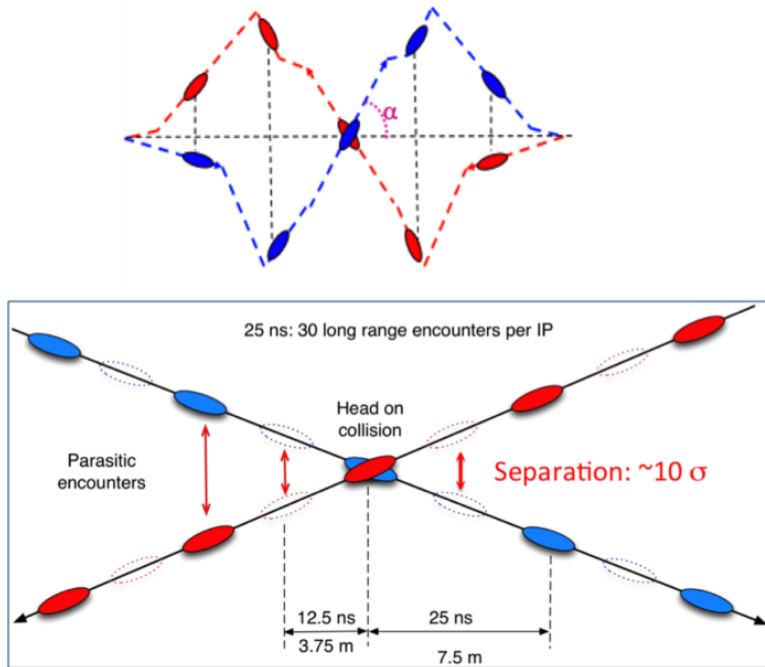


Figure 2.3: The crossing angles are an essential feature of the machine set-up. They have to be big enough to reduce the long-range beam-beam effect. [15]

### 2.3.2 Center of mass energy

The center of mass energy  $E_{cm}$  (or  $\sqrt{s}$ ) of two relativistic particles with four-momenta  $\mathbf{p}$  and  $\mathbf{q}$  colliding is given by:

$$E_{cm} = \sqrt{s} = \sqrt{(p_\mu + q_\mu) \cdot (p^\mu + q^\mu)} \quad (2.6)$$

For colliding beam experiments, where two particles of energy  $E$  collide head-on (i.e.  $p = (E, p_x, p_y, p_z)$  and  $q = (E, -p_x, -p_y, -p_z)$ ), the center of mass energy is:

$$E_{cm} = \sqrt{s} = 2E \quad (2.7)$$

For the LHC machine with nominal (design) beam energy  $E = 6.5$  (7) TeV, this translates into a center of mass energy of  $\sqrt{s} = 13$  (14) TeV.

### 2.3.3 Operational cycles of the LHC

In order to accelerate and collide the bunches at such high energies, the beam cycle (also called fill) time of the LHC machine is rather long. As injection and collision energies differ and 2-in-1 magnets are used, first both rings need to be filled, then the energy is ramped up from injection to collision, and finally the beams are brought into collisions at the interaction points. At the end, they are finally extracted. The typical operational cycle of the LHC is illustrated in figure 2.4. The different phases of each operational cycle are labelled as beam mode [16].

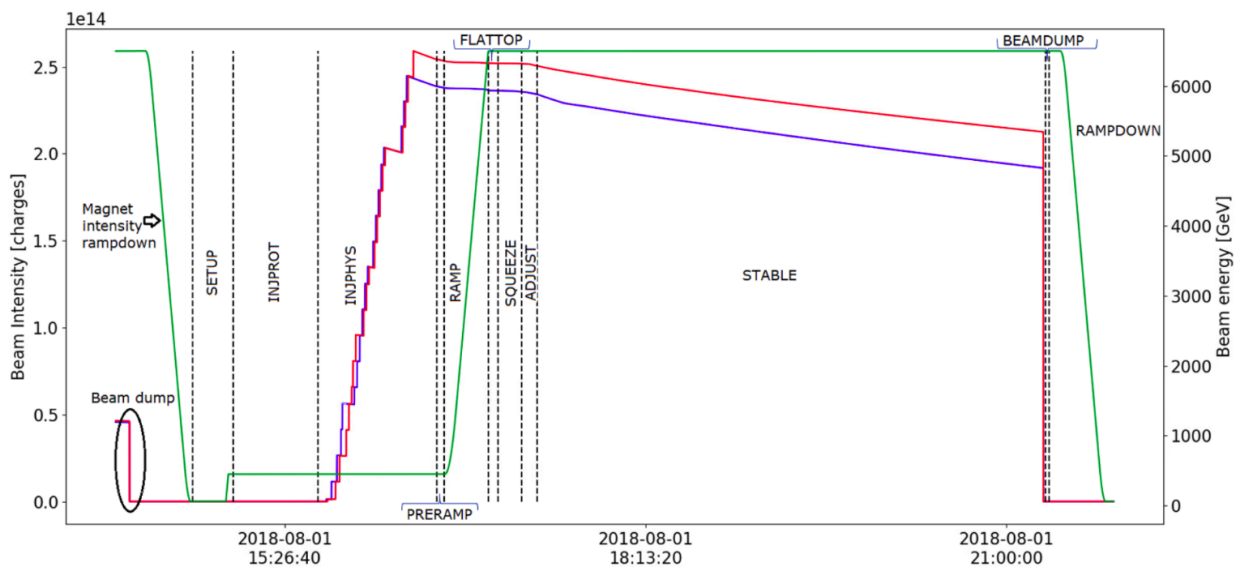


Figure 2.4: The LHC Beam Cycle of a nominal LHC fill (shown here, fill #7006). The intensity of beam 1 and beam 2 is represented in blue and orange, respectively, while the energy of the beams is represented in green. The dashed black lines represent the moments of time in which the beam mode is changed. The name of each beam mode is placed between two dashed black lines: it represents the period of time in which that beam mode is present. [17]

There are in total 19 beam modes, however the most relevant one for the interaction points (IP) where collisions occur is the STABLE BEAMS mode: This signals the experiments that conditions are stable and the beams can be continuously collided, thereby producing luminosity and collision data. Only a limited set of commissioned and well understood machine manipulations (such as luminosity optimization or levelling, explain in Section 2.5) are allowed in STABLE BEAMS.

Ultimately, a beam dump will either be programmed by the operators at the designated end of a fill

(due to beam intensity being to low for efficient luminosity production) or be triggered by a machine protection element in case of a technical problem. Once the decision to remove the beam is made, the LHC beam dump system extracts the beam within 3 turns [1].

The beams typically (and ideally) stay in collisions in STABLE BEAMS for about 10 to 20 h. However, unwanted premature dumps may occur, thereby limitting the LHC performance. The motivatiaton for these dumps vary from radiation to electronics (R2E) failures to protecting the machine due to unwanted high beam losses, since the immense amount of energy stored in the LHC beams makes them highly destructive. The total energy in each beam at top energy (6.5 TeV) is approximately 300 MJ<sup>1</sup>. Even a small loss of the beam particles could damage machine elements or generate a quench in the superconducting magnets. At top energy, losses on the level of 30 mJ/cm<sup>3</sup>, by a local transient loss of  $4 \cdot 10^7$  protons would produce a quench on the superconducting magnet coil [1].

## 2.4 Beam loss mechanisms

Various physical mechanisms can lead to beam losses in particle accelerators. While some losses are unavoidable, as a result of the standard operation of the machine, some losses can be caused by failures of accelerator systems or wrong beam manipulations and should be avoided.

Whenever a particle leaves its stable trajectory, it will be lost on either the collimators or the beam screen. Some of the machine operational parameters and settings of the accelerator have direct impacts on the losses, e.g. a collimator opening apertures determine the losses downstream.

Owing to the high energy and intensity of the LHC beams, even the loss of a small fraction of the beam is capable of causing significant energy depositions, large enough to generate a local increase of the temperature. If the temperature increases in a super conducting element beyond the critical temperature, the superconductor transitions to a normal conductor (it quenches), and an ohmic resistance (re)appears. In order to protect the accelerator, the beam dump is then triggered. In the best case scenario, a quench of an LHC magnet would cause a downtime in the order of hours, but in case of damage, the downtime could be in the order of months in order to replace the damaged magnet [18, 19].

There are many beam loss mechanisms that are can occur and are observed in the LHC, which are summarized below (in addition to the scattering amongst the beam particles or beam instabilities).

---

<sup>1</sup>This result can be obtained with a simple calculation:  $E_{beam} = 2556 \text{ bunches} \cdot 1.15 \cdot 10^{11} \text{ particles per bunch} \cdot 6.5 \text{ TeV per particle}$ , which is approximately as energetic as a 400-ton train, like the German IC, travelling at 140 km/h.

### 2.4.1 Luminosity burn-off

As it can be seen in Figure 2.4, the luminosity is not constant over time during STABLE BEAMS mode, owing to the collisions that lead to a burn-off loss of particles:

$$k \frac{dN_{1,2}(t)}{dt} = -\sigma_{inel} n_{ip} \mathcal{L}(t) \quad (2.8)$$

where  $\sigma_{inel}$  is the inelastic cross-section of the colliding particle,  $k$  is the number of bunches and  $n_{ip}$  is the number of collision points. Assuming momentarily that the burn-off as the only mechanism that affects the initial luminosity  $\mathcal{L}_0$ , its time behaviour [20] is given by:

$$\mathcal{L}(t) = \frac{\mathcal{L}_0}{\left(1 + t\sigma_{inel} n_{ip} \frac{\mathcal{L}_0}{N_0 k}\right)^2} \quad (2.9)$$

where in addition  $N_0$  is the initial bunch intensity.

Collision debris from inelastic collisions at the interaction point (IP), that no longer conform with LHC requirements, is lost downstream (hundreds of meters away) of the experiments causing locally the highest radiation levels in the accelerator. These losses scale around the IP scale with the delivered integrated luminosity of the experiment [21] and are considered not to be observed in the arc sections, but only in the long straight section (LSS) and dispersion suppressor (DS), and represent the main source of radiation for this thesis.

### 2.4.2 Beam-residual gas interactions

The vacuum in the LHC is not perfect and some residual gas molecules are present in the beam pipes. Some particles in the beams interact with these molecules, resulting in continuous loss of particles that is roughly constant along the accelerator. It is expected that these losses scale linearly with integrated intensity and residual gas density [21]. They are most relevant in the arc regions.

### 2.4.3 Beam-machine interactions

Before reaching the LHC tunnel, the beam particles typically interact with machine elements, such as collimators, absorbers, or magnets. This occurs throughout the LHC accelerator, both for the experimental caverns (collision products) and in the IRs where no collisions are produced, where beam-machine interactions (e.g. collimation) can be seen as the primary source of radiation.

#### 2.4.4 Beam-beam effects

During collisions, particle bunches interact amongst each other and may gain a momentum transfer to the transverse plane. One source is their mutual perturbation via their electromagnetic fields. The resulting forces are highly non-linear and result in a wide spectrum of consequences for beam dynamics [22]. Assuming round Gaussian beams with standard deviation  $\sigma$ , this beam-beam kick can be described by:

$$\Delta r' = -\frac{1}{r} \frac{2r_0 N}{\gamma_{rel}} \left[ 1 - \exp \left( -\frac{r^2}{2\sigma^2} \right) \right] \quad (2.10)$$

where  $r$  is the distance from the opposing beam,  $r_0 = e^2 / 4\pi\epsilon_0 mc^2$  is the classical electron radius,  $N$  is the number of particles per bunch and  $\gamma_{rel}$  is the relativistic factor.

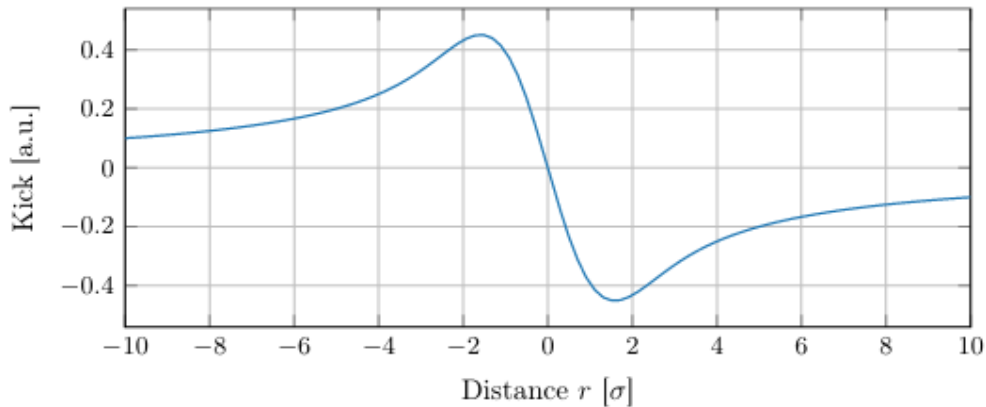


Figure 2.5: The beam-beam kick for round Gaussian beams [14]

### 2.5 LHC luminosity achievements

One of the most important challenges in the LHC operation is delivering the maximum integrated luminosity to the experiments. The first luminosity delivered to the experiments was in 2010. After an initial operation (Run 1) for three years, the LHC was shut down in 2013-2014 for major upgrades and maintenance work: the long shutdown 1 (LS1). The machine was re-commissioned in 2015, and the subsequent three years (Run 2) were dedicated to luminosity production. So far, almost  $200 \text{ fb}^{-1}$  have been delivered to the ATLAS and CMS experiments (see Table 2.1 and Figure 2.6).

The LHC has been performing proton acceleration and proton-proton collisions during Run 1 (2011-2013) and Run 2 (2015-2018), with an increasing performance through the years (see Figure 2.6). A further increase is expected in Run 3 (expected for 2022-2024), as well as for the High-Luminosity LHC project (2027-onwards). The beam energy currently reaches up to 6.5 TeV (with future planning

to be used at 7 TeV in Run 3 and High Luminosity LHC), with up to 2 556 bunches per beam and, on average, and  $1.15 \cdot 10^{11}$  particles per bunch (achieved during Run 2).

Finally, besides protons, several other particles species and/or test runs have been used. For a summary of the LHC Run 2 performance, see Table 2.1.

The increase in the total delivered luminosity is mainly due do the increase in instantaneous luminosity. However, the event pile-up  $\mu$  (the average number of interactions per crossing of bunch pair) subsequently increases as well [14]. The maximum acceptable pile-up (65 particle interactions per bunch-crossing for ATLAS and CMS, 0.1 for ALICE and 1.5 for LHCb) is limited by the capabilities of the experimental detectors to identify all primary vertexes and to assign the detected secondary particles to the correct primary/event. Above a certain limit, the data quality is degraded up to an extent where the recorded data becomes unusable for certain physics analyses.

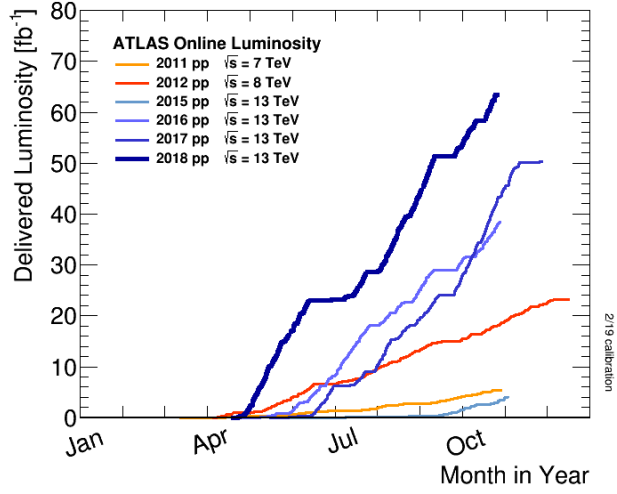


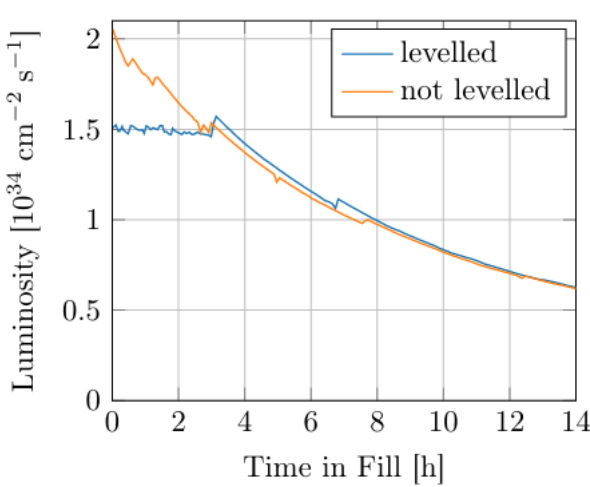
Figure 2.6: Delivered Luminosity versus time for 2011-2018, proton-proton ( $pp$ ) data only. Cumulative luminosity versus day delivered to ATLAS during stable beams and for high energy  $pp$  collisions. [23]

In order to fulfill the needs for all experiments, it is necessary to actively control the instantaneous luminosity during operation. Such a luminosity algorithm is called *levelling*. It takes the measured luminosity of an experiment and uses one or more machine parameters to reduce the instantaneous luminosity to the target communicated by an experiment reducing the pile-up accordingly. Possible machine parameters used for this purpose are: closed orbit separations (separation factor), the crossing angles  $\alpha$  (geometric factor  $\mathcal{F}$ ) or the  $\beta^*$  (beamsize at the IP), and their impact can be seen in Figure 2.7.

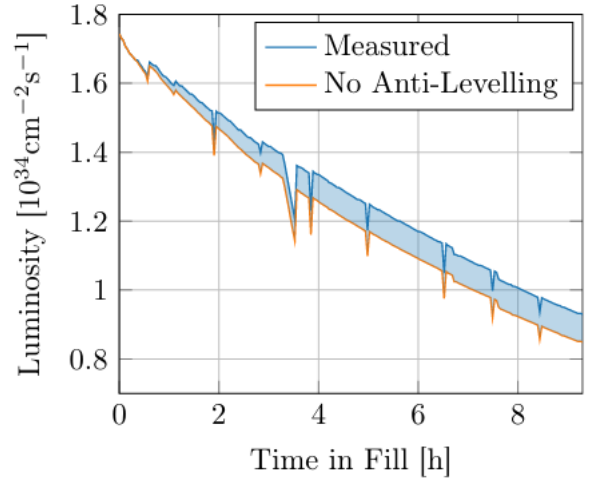
Conversely, the same parameters can be changed to increase the instantaneous luminosity to exploit the machine, and this procedure is called *anti-levelling*. This is employed during the fill as the luminosity burn-off reduces the instantaneous luminosity below the pile-up threshold. For the scope of this thesis, all these changes have an impact on the radiation levels produced in the LHC tunnels.

Table 2.1: Total delivered luminosities per year for each interaction point (IP) for each particle species. The data has been collected from Ref. [23] (ATLAS) and Ref. [24] (CMS)

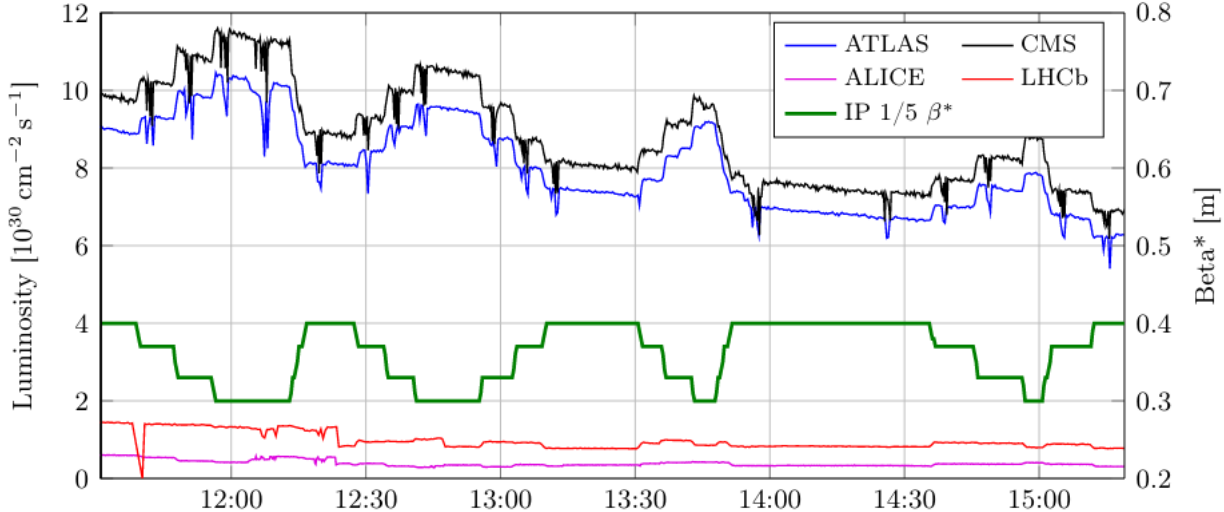
Run	Year	Data set	IP1/ATLAS	IP5/CMS
Run 1	2010	$pp @ \sqrt{s} = 7 \text{ TeV}$	48.1 $\text{pb}^{-1}$	44.96 $\text{pb}^{-1}$
		Pb-Pb @ $\sqrt{s}_{NN} = 2.76 \text{ TeV}$	9.69 $\mu\text{b}^{-1}$	
	2011	$pp @ \sqrt{s} = 7 \text{ TeV}$	5.46 $\text{fb}^{-1}$	6.1 $\text{fb}^{-1}$
		Pb-Pb @ $\sqrt{s}_{NN} = 2.76 \text{ TeV}$	166 $\mu\text{b}^{-1}$	184.07 $\mu\text{b}^{-1}$
	2012	$pp @ \sqrt{s} = 8 \text{ TeV}$	22.8 $\text{fb}^{-1}$	23.3 $\text{fb}^{-1}$
		$p\text{-Pb} @ \sqrt{s}_{NN} = 5.02 \text{ TeV}$	31.2 $\text{nb}^{-1}$	36.14 $\text{nb}^{-1}$
Run 2	2013	$pp @ \sqrt{s} = 2.76 \text{ TeV}$		5.61 $\text{pb}^{-1}$
		$pp @ \sqrt{s} = 13 \text{ TeV} (50 \text{ ns})$	102.2 $\text{pb}^{-1}$	28.7 $\text{pb}^{-1}$
		$pp @ \sqrt{s} = 13 \text{ TeV} (25 \text{ ns})$	3.88 $\text{fb}^{-1}$	4.31 $\text{fb}^{-1}$
		$pp @ \sqrt{s} = 5.02 \text{ TeV}$	26.1 $\text{pb}^{-1}$	5.02 $\text{pb}^{-1}$
	2015	Pb-Pb @ $\sqrt{s}_{NN} = 5.02 \text{ TeV}$	0.51 $\text{nb}^{-1}$	0.5946 $\text{nb}^{-1}$
		$pp @ \sqrt{s} = 13 \text{ TeV}$	38 $\text{fb}^{-1}$	41.58 $\text{fb}^{-1}$
		$p\text{-Pb} @ \sqrt{s}_{NN} = 8.16 \text{ TeV}$	170 $\text{nb}^{-1}$	188.34 $\text{nb}^{-1}$
		$p\text{-Pb} @ \sqrt{s}_{NN} = 5.02 \text{ TeV}$	0.44 $\text{nb}^{-1}$	0.53 $\text{nb}^{-1}$
	2016	$pp @ \sqrt{s} = 13 \text{ TeV}$	49 $\text{fb}^{-1}$	49.79 $\text{fb}^{-1}$
		Xe-Xe @ $\sqrt{s}_{NN} = 5.44 \text{ TeV}$	1.97 $\text{nb}^{-1}$	
		$pp @ \sqrt{s} = 5.02 \text{ TeV} (\mu = 2)$	273 $\text{pb}^{-1}$	341.29 $\text{pb}^{-1}$
		$pp @ \sqrt{s} = 13 \text{ TeV} (\mu = 2)$	150 $\text{pb}^{-1}$	
	2017	$pp @ \sqrt{s} = 13 \text{ TeV}$	62.1 $\text{fb}^{-1}$	67.86 $\text{fb}^{-1}$
		$pp @ \sqrt{s} = 13 \text{ TeV} (\mu = 2)$	213 $\text{pb}^{-1}$	
		Pb-Pb @ $\sqrt{s}_{NN} = 5.02 \text{ TeV}$	1.78 $\text{nb}^{-1}$	1.8 $\text{nb}^{-1}$



(a) Comparison of LHC fill 6358 (non-levelled test fill) to LHC fill 6360 (levelled)



(b) Quasi-continuous crossing angle anti-levelling test in LHC fill 6061. The crossing angle is gradually reduced in small steps of  $1 \mu\text{rad}$ .



(c) Luminosity from the LHC experiments during  $\beta^*$  anti-levelling test fill 6424

Figure 2.7: Luminosity Levelling algorithm methods. [14]

## 2.6 Luminosity driven losses at the experimental interaction points

One can classify the insertion regions (IR) into two categories based on the dominant source of interaction. At the four experimental interaction points, the radiation is mainly dominated by the collisions themselves, hence the scaling factor employed in such areas is the total delivered luminosity  $\mathcal{L}_{int}$ . At the other four insertion regions, the radiation field is dominated by the beam interactions with the machine elements or the residual gas, and the relevant scaling factor is generally taken to be the beam intensity, possibly combined with other parameters. The former is further explained here, while for a summary of the latter, please consult Appendix Chapter B.

The four LHC experiments (ATLAS/IP1, ALICE/IP2, CMS/IP5 and LHCb/IP8) share similarities both in the radiation they produce and in the beamline elements located in the tunnel. They consist in particle detectors placed around the point where the two beams intersect and the particle bunches collide.

ATLAS and CMS are the high-luminosity general purpose experiments, which imply the highest radiation levels in the nearby LHC tunnel and hence the priority of this thesis. For the majority of the LHC operation, they are employed at the maximum luminosity possible, meaning with the beams colliding at a minimal  $\beta^*$  (e.g. 30 cm in 2017).

LHCb is a low-luminosity experiment for B-physics, which is a special field within the domain of particle physics that focused on the study of the properties of B hadrons, which contain at least one bottom quark. In the present operation, its  $\beta^*$  is as high as 10 m. Its radiation environment, especially in light of the LHCb upgrade, has been studied in References [25, 26].

The ALICE experiment is dedicated to heavy ion operations, which are accelerated to lower energies leading into a less intense radiation shower in the tunnel that has not been studied yet. Its  $\beta^*$  is kept at 10 m, similarly to LHCb.

The exact location and machine parameters differ from experiment to experiment, but in general the beamline elements are placed as described below.

### 2.6.1 Long straight sections

The insertion regions around IP1 and IP5 are schematically shown in Figure 2.8. The insertions are (almost) symmetric with respect to the interaction point IP, where the beam particles are squeezed before entering the detector to increase the chances of collisions with particles coming from the opposite direction. Three quadrupoles (Q1, Q2, Q3) are used for this purpose, forming a system called an inner triplet (IT), which tightens the beam, making it approximatively 12.5 times narrower, from a transversal size of 0.2 mm, down to 16  $\mu\text{m}$  across, thereby minimizing the  $\beta^*$ . There is one IT on each side of the four experimental caverns.

As well as sharing the beam pipe (vacuum chamber), the two counter-rotating beams share the triplets in the experimental IRs, ranging from 0 to approximatively 147 m into the LSS, where the beams are separated/recombined by a pair of separation/recombination dipoles (D1 and D2) which join the

## 2.6 Luminosity driven losses at the experimental interaction points

design orbits of the two rings. They are located left and right from the triplet magnets (IT), and bring the two beams onto a colliding orbit at the interaction point and then separate them again beyond the collision point. They are also used as in several insertions where they are needed to change the beam separation from/to the nominal 194 mm in the LHC arcs. Next to the ALICE and LHCb detectors, IR2 and IR8 also contain the injection systems for beam 1 and beam 2 coming from the super proton synchrotron (SPS). After the D1, the separation needs to be ensured by an additional crossing angle. The crossing plane is vertical in IP1 (and IP2) and horizontal in IP5 (and IP8).

Moreover, collimators (see Appendix Chapter B.2 for more details about their role) are placed along the beamline to protect beam elements downstream of the collimators. For example, around the high luminosity LHC experiments in IP1/5, physics debris collimator absorbers, known as target collimator long (TCL) are employed in order to protect the cold magnets in the dispersion suppressor (DS) region (from 269 m onwards) from products of proton-proton collisions, such that magnet quenches from overheating are avoided. There are three such collimators, numbered according to the half-cell they are placed in (TCL4, 5 and 6), which can be operated at different aperture sizes for stronger/weaker collimation. The collimators settings are predefined as either "closed" or "open" aperture, with the exact gap distance remaining constant over one year of operation. However, during individual fills of the LHC, the TCLs have been switched from open to closed, or vice-versa.

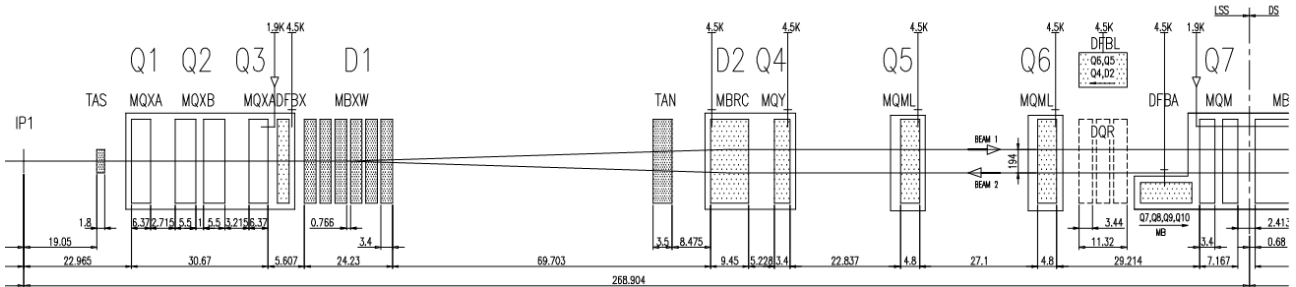


Figure 2.8: LSS layout of beam elements for the insertion region to the right of IP1 [1]. Dimensions and distances (bottom) are given in meters. Cryogenic temperatures (top) are given in Kelvin.

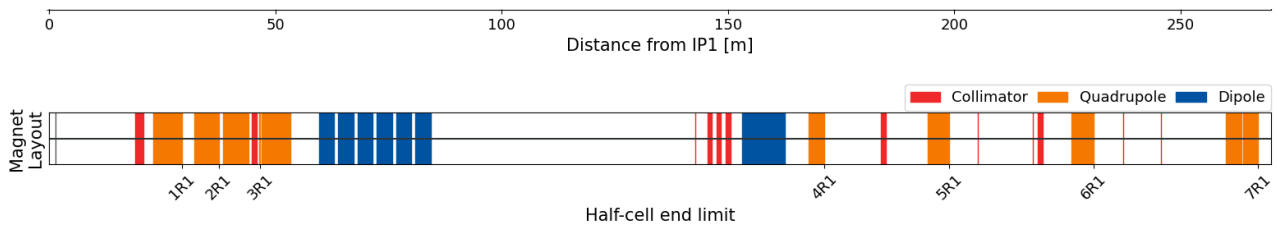


Figure 2.9: LSS layout of beam elements

The final beamline element of interest in the scope of this thesis are the roman pots [27] (called pots because the detectors are housed in cylindrical vessels). They represent is an important tool to measure the total cross section of two particle beams in a collider. The first generation of roman pot (RP) was used in the measurement of the total cross-section of proton-proton inter-actions in the intersecting storage rings (ISR) [28]. Roman pots are placed ideally as close to the beamline as possible, such that they capture the accelerated particles scattered at very small angles. They can either be used (or not), in which case they act as local shielding by absorbing some of the radiation. The roman pots in ATLAS are called ALPHA [29], and those in CMS belong to the TOTEM [30] experiment.

### 2.6.2 Dispersion suppressor

The dispersion suppressor (DS) consists of the first bending magnets and also adjusting the beam optics from the LSS leading into the LHC arc. It consists of four cells of superconducting magnets. Given that they are the closes to the interaction point, they suffer the most radiation damage among all cold magnets, and therefore special attention has been given to them: the TCL6, when used, reduced the radiation levels by a factor of 20, and a quench protection system (QPS) [31] has been added to monitor the instantaneous losses to avoid heating of the magnets.

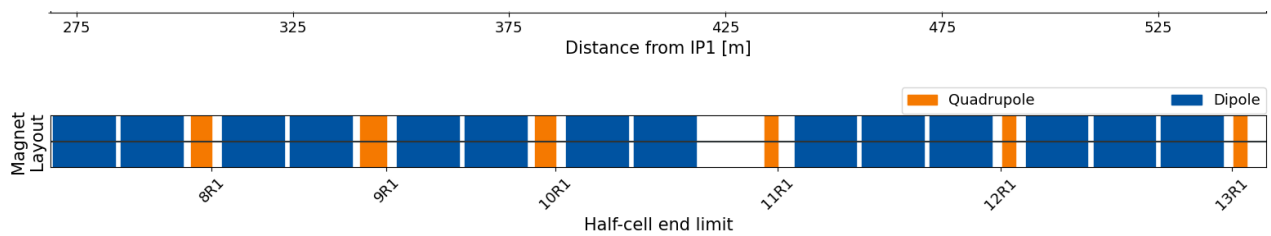


Figure 2.10: DS layout of beam elements

### 2.6.3 Shielded alcoves

The LHC tunnel areas next to the high luminosity IPs and parts of the DS have radiation levels that are in general too large to be able to host electronics systems based on commercial off-the-shelf (COTS) components. Therefore, shielded service galleries (commonly referred to as shielded alcoves) were constructed the nearby the tunnels to place the necessary hardware. The shielded alcoves have different names and are numbered with respect to the IR they are neighbouring: UJ (junction chamber) and UL (liaison gallery between underground works) zones are heavily shielded areas near the collision points, and the RRs are lightly shielded (40 cm of concrete) almost at the border between the LSS and the DS (from 240 to 260 m). A schematic representation of the RadMON location in the UJ, UL and RR alcoves and their vicinity is shown in Figures 2.11 for the area right of IP1.

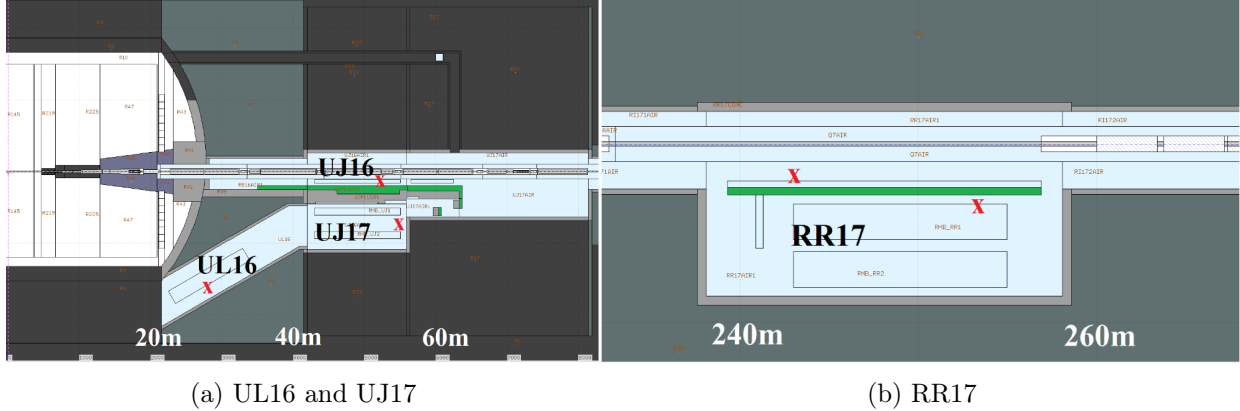


Figure 2.11: FLUKA top-view geometry of the LHC layout right of IP1, indicating the (a) UL/UJ and (b) RR shielded alcoves, as well as the radiation monitors (RadMONs), marked with red crosses. The distance to the IP is included. The layout is slightly different for IP5. [32]

#### 2.6.4 Arc region

The LHC arc cell has been optimized for a maximum integrated dipole field along the arc with a minimum number of magnet interconnections. They consist of standard focusing and defocusing (FoDo) cells (see Figure 2.12), which consist of equidistant, upright horizontally focusing (QF) and horizontally defocusing (QD) quadrupoles of the same strength. The space between the QF and the QD is taken by the main 8.3 T bending dipoles and corrector magnets. Stronger 11 T magnets were planned to be put in IR7 only in specific positions during the long shutdown 2 (LS2), but this has been delayed.

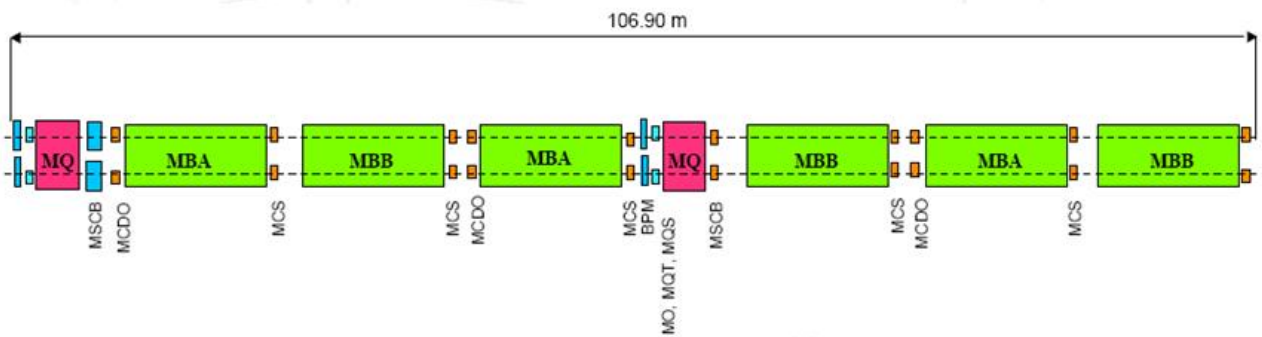


Figure 2.12: Schematic of an LHC cell [1]. “MBA/B” are the bending dipoles, “MQ” are the focusing quadrupoles (both superconducting). The smaller magnets in between are dipolar (orbit), quadrupolar (tune) and higher order correctors.



# Chapter 3

## Radiation Effects on Electronics

Beam losses generate a radiation environment capable of severe damage to the electronics. The main task of the radiation to electronics R2E project is to minimize the accelerator downtime by minimizing failures due to electronic equipment. While the physics discoveries require larger integrated luminosities for better statistics and higher center-of-mass energies to probe experimentally unknown territories, the entire large hadron collider (LHC) machine, in particular its electronics, are taking a toll. During the operation of the accelerator, several beam loss mechanism occur, which create a prompt radiation field along the LHC. This mixed radiation field consists of both hadrons with wide energy spectra from 0.025 eV (thermal neutrons) up to hundreds of GeV, as well as electromagnetic components. The prompt radiation damage is two-fold: (i) accelerated ageing of the exposed elements, which results in a reduced lifetime, and (ii) single-event effects in the electronics, which might lead to premature beam dumps. The interest for the R2E project is both to asses the current radiation levels impacting the electronics for the existing machines in the CERN accelerator complex and to estimate the future levels for the upcoming accelerators, e.g. High Luminosity LHC (HL-LHC) [32]. Therefore, the knowledge of the dose distribution and of the components of the radiation field are of paramount importance to R2E, as they are relevant in choosing the correct position for the elements in order to optimise their lifespan [21] and in reducing interruptions in the accelerator operation caused by electronics failures.

### 3.1 The radiation to electronics project at CERN

The radiation to electronics (R2E) project has the main responsibility to mitigate the issue of premature beam dumps due to electronics failures caused by radiation. It assists LHC operations and equipment groups with assessments of radiation-induced failures in electronics of accelerator components (see Figure 3.1), in order to minimize all risks of radiation-induced failures at CERN accelerators, starting with the LHC. Mitigation techniques can consist of the (re)placement of shieldings and repositioning of equipment, as well as the upcoming radiation hardness assurance (RHA) procedure for electronics systems.

Modern high-energy hadron accelerators demand a significant number of electronic components being placed close to the beam-line and to the experiments. The LHC requires superconducting technologies (at low temperatures), efficient collimation systems as well as precise and fast monitoring of the

operational parameters of the machine. This implies more complex electronics for control, steering and powering, which can contain up to thousands of commercially off-the-shelf (COTS) units, such as power converters (carrying the necessary currents from the external supplies into the magnets), the quench protection system (QPS) (protecting the superconducting equipment from incidents (quenches) caused by excessive heat) or the vacuum and beam instrumentation, just to name a few.

The LHC radiation showers that originate from a primary nuclear interaction (e.g. proton on machine element, like the collimators) produce cascades of secondary particles, predominantly hadrons (such as protons, neutrons, kaons, pions, etc.). The shower then develops into both: i) an electromagnetic component (mainly from fast  $\pi^0 \rightarrow \gamma\gamma$  decay) and ii) a hadronic component. Decaying charged kaons and pions lead to weaker interacting particles, such as muons and neutrinos. The radiation profile (both in terms of intensity and composition) greatly varies based on several parameters: the energy of the primary interaction, the distance travelled and the amount of shielding material.

Regarding the radiation tolerance of readout electronics, the LHC experiments take advantage of valuable knowledge gained by the development of various space and defence applications for which the space agencies have databases with radiation-hard electronic components. The radiation background on electronic devices in the LHC detectors is quite similar with the one from the Van Allen belt and this allow assessing the devices behaviour as well as semiconductor fabrication technology feasibility. [33]

The assessment of radiation damage to electronics is a complex process and requires for the source term a detailed description of the full particle energy spectra, as well as a clear characterization of the calculated quantities used to predict radiation damage. The information is provided to the responsible for the equipment and is to be used as design criteria for the new equipment to be installed in the respective locations. [34]

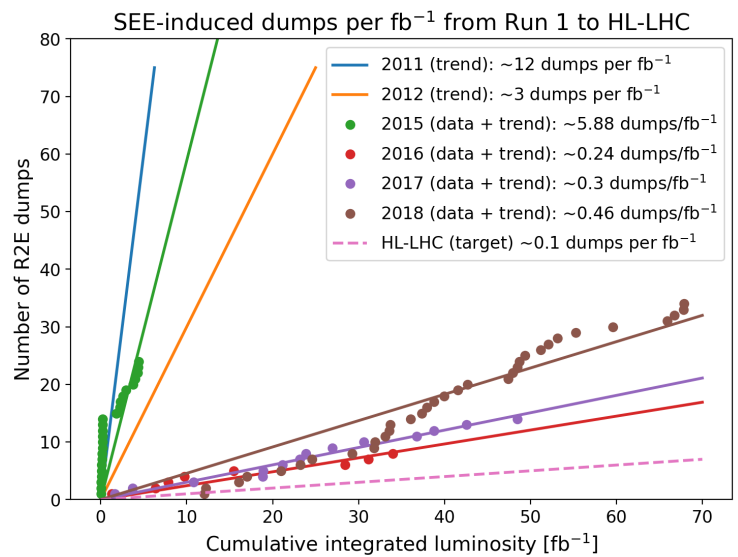


Figure 3.1: R2E related (single event effect induced) dumps per  $\text{fb}^{-1}$  from Run 1 to HL-LHC

## 3.2 LHC availability and R2E performance

As previously described, a key figure of merit quantifying the performance of the LHC is the integrated luminosity delivered to its high-luminosity experiments ATLAS and CMS, expressed in inverse femtobarns ( $\text{fb}^{-1}$ ) and proportional to the number of collisions in the interaction points (IP). As a consequence, it is useful to measure the R2E performance by counting the number of R2E-induced beam dumps per unit  $\text{fb}^{-1}$ , where a smaller figure corresponds to a milder impact on the production of LHC collisions. Similarly, the performance targets of the R2E project are defined by performing modelling studies of the LHC availability [35] and deriving the maximum number of R2E-induced beam dumps per unit  $\text{fb}^{-1}$  that are compatible with keeping the resulting loss of integrated luminosity below a reference threshold (typically 1% of lost luminosity out of the total delivered).

There have been several mitigation measures, implemented during Run 1 (2010-2012) and especially during long shutdown 1 (LS1, 2013-2014). Consequently, radiation effects on electronics (R2E) causing equipment failures leading to LHC beam dumps and/or machine downtime has been sufficiently low as to yield a minor impact on the accelerator performance. During Run 2 (2015-2018) the R2E related failures per unit of integrated luminosity have successfully stayed below the objective value of 0.5 events/ $\text{fb}^{-1}$ , except the 2015 run dedicated to machine commissioning. However, during 2018, a mild increase in the failure rate has raised the attention of the R2E project. This increase was linked to the increased radiation levels in the dispersion suppressors (DS) of the ATLAS and CMS experimental insertions, affecting the quench protection system (QPS) located underneath the superconducting magnets in the LHC tunnel (from 269 to 340 m)[36].

The number of beam dumps induced by R2E faults is shown in Figure 3.1 as a function of the cumulative integrated luminosity for the LHC in Run 1 (with trend lines from Ref. [37]) and in Run 2 (for which the single R2E-induced dumps are shown individually, as further described in the next section). A similar R2E performance is also targeted for the upcoming LHC Run 3, during which the performance of the LHC is expected to further improve compared to Run 2, both in terms of beam intensity and annual integrated luminosity. In addition, Figure 3.1 includes the 0.1 dumps/ $\text{fb}^{-1}$  target for the HL-LHC upgrade, determined by means of machine availability simulations as described above. To be able to meet this ambitious target, the electronic systems are required to follow a dedicated radiation hardness assurance (RHA) procedure [32, 38], where the radiation environment is taken into account already in the early phases of the system development.

## 3.3 Radiation effects on electronics

Focusing on quantifying radiation-induced damage to electronics, the damage mechanisms that take place in the presence of various radiation fields can be classified in the two main categories discussed in the next paragraphs.

### 3.3.1 Cumulative effects

Cumulative effects take place through a continuous exposure to radiation that is happening during the active lifetime of the electronics, causing permanent damages and thus, making them out of specification. In cases like this, the effect is permanent and a power reset does not solve the problem.

#### 3.3.1.1 Total ionizing dose

When charged particles and photons penetrate a medium, they interact with electrons in the atomic shells, possibly leading to ionisation, which in semiconductors can be considered as electron - hole pairs creation. The total ionizing dose (TID) is a quantity used to describe this cumulative ionisation effect. The main issue with TID is the gradual performance deterioration of the circuits that can potentially lead to system failures. Presented in different units depending on the application, the most common one is the radiation absorbed dose (rad) and the one used in this thesis is the international system unit (ISU), gray (Gy), where  $1 \text{ Gy} = 100 \text{ rad} = 1 \text{ J/kg}$ .

The TID impacts the conductive properties of the material, such as leakages or threshold voltage shifts. In microelectronics, TID defects imply the accumulation of trapped charges in the field oxides of the circuit. As ionization occurs, electron-hole pairs are formed in the material (e.g. silicon dioxide  $\text{SiO}_2$ ). Not all of the pairs recombine, but some of them move due to the applied electric field. Owing to their much higher mobility, electrons can exit the oxide leading to trapped holes in defect centers in the oxide volume. Furthermore, this process can activate other defects at the oxide interfaces. TID causes device degradation mainly via creation of defects and charge buildup. Some examples include:

- **Threshold voltage shifts:** Charge buildup is caused by holes trapped in the bulk of the oxide. These charges could alter the gate oxide of metal-oxide-semiconductor (MOS) transistors electric fields, leading to a change in its I-V characteristics. Most important is the shift of the power-ON (threshold) voltage which is negative for n-channel (NMOS) and positive for p-channel MOS (PMOS). As a result, a device might become unresponsive to some commands as it might be “blocked” on a specific state.
- **Increased leakage current:** In NMOS transistors, the interface and free leakage paths could be reversed due to the charges that might create an image charge in the semiconductor. These parasitic leakage currents increased power consumption and exhibit degraded timings.
- **Amplifier gain degradation:** TID-induced damage in bipolar transistors usually manifests as a reduction in bipolar gain with increasing total dose exposure. The device requires more supplied power in order to compensate for gain degradation.
- **Dark signal in camera sensors:** As a direct effect of charging the gate oxides, electrostatic potential is generated in pixels which shifts and gets “un-pinned”. This results in thermally generated charges that are not suppressed anymore. This manifests as an increased noise background and is observed in both and complementary MOS (CMOS) and charge-coupled devices (CCD), leading to a compromised dynamical range of the imager.

When it comes to qualifying a device for TID, it is usually done via an accelerated-life test approach, as it is not feasible to expose it over the years they will be employed at CERN. In order to reach reasonable running times of the qualifying experiments, the accelerated testing is done at substantially higher dose rates than in the accelerator environment. However, this assumption that the component reaches its end-of-life depending only on the total dose has been proven wrong in practice for a specific family of device.

In particular, bipolar devices suffer more detrimental the effects at lower dose rate. This phenomenon is called enhanced low dose rate sensitivity (ELDRS) and is a serious risk to consider when designing power distribution systems and their shielding. For example, CERN considers a factor of 5 margin when specifying radiation leveles due to ELDRS.

Usually, the low dose radiation rate is considered to be less than or equal to  $100 \mu\text{Gy}/\text{s}$ . Compared to it, high dose rate testing at  $100 \text{ Gy}/\text{s}$  takes only to 28 hours.

To provide some context, the difference between different levels of TID qualification levels, commercially off-the-shelf (COTS) devices are typically rated below  $100 \text{ Gy} (\text{SiO}_2)$ , radiation-tolerant devices below  $1 \text{ kGy} (\text{SiO}_2)$  whereas radiation-hardened devices above  $100 \text{ kGy} (\text{SiO}_2)$ .

### 3.3.1.2 Displacement damage

Generally, structural damage (e.g. atomic rearrangement) on the crystal lattice of devices by non-ionizing energy loss in the material caused by high energy particles (e.g. neutrons) is called displacement damage (DD). This can lead to crystal imperfections, e.g. lattice atoms displaced to defect locations and vacant lattice sites. When this occurs, the electrical properties at the defect's region get modified by the creation of new energy states within the energy band gap region of the semiconductor. This effect is increasingly detrimental with the increase in the number of defects. The defects can play a role in various undesired ways: charge traps, recombination centres, generation centres of thermal charge and more other.

Compared to TID, displacement damage dose (DDD) comprise all non-ionizing dose effects on a device, and can be referred to as total non-ionizing dose (TNID). In general, the TNID effects are independent of the flux or the device biasing and consists of an increased defect concentration throughout the device bulk. In the following, a summary of DD effects on electronic devices is presented:

- **Gain degradation:** Due to the recombination centres created by DD, the minority charge carriers will have a shorter lifetime. This leads to an increased input bias current that is necessary, thereby leading to a reduction in gain.
- **Gate-oxide breakdown:** In extreme cases, the accumulation of DD defects may result in a short in the insulating layer in the gate oxide bulk. Locally, this could melt the region and destroy the structure.
- **Charge traps and hot pixels on camera sensors:** Image sensors (CCD, CMOS etc.) are particularly affected by DD via various mechanisms. In some cases, defect clusters in the pixel

array could act as regions with increased dark signal, leading to distinctly bright spots in images. In other cases, defects could act as traps for photogenerated charge, thereby reducing the charge transfer efficiency leading to signal streaks in the image.

### 3.3.2 Single-event effects

Stochastic events caused by energy deposition by one highly energetic particle in a sensitive volume (e.g. a memory cell) are called single event effects (SEEs). In order to ensure the reliability of semiconductor devices (and electronics, in general) in the harsh accelerator environment, the equipment should be tested for both TID and SEE. However, testing for the SEE performance of a device is more complicated than for the TID hardness; this is mainly due to the increasing complexity of modern digital devices, the different manifestations of these effects and the fact that testing for SEEs takes place during radiation exposure while TID testing does not.

SEEs are classified in hard (destructive) or soft (non-destructive), based on whether the device can resume nominal operation after a power cycle. Soft errors consists of: single event upset (SEU), single event transient (SET) and single event functional interrupt (SEFI), while hard errors consist of: single event latch-up (SEL), single event burnout (SEB), single event snapback (SESB), single-event dielectric rupture (SEDR), single event gate rupture (SEGR) and single event burnout (SEB) [39]. The severity or harshness of SEEs is given by the effect type from the aforementioned ones and depends on how critical the system is for operation.

For example, in digital devices, information is sent/stored as bits. A type of SEE is the single event upset (SEU), which can flip the bit to its opposite value thereby altering the information.

The SEE can be produced:

- directly, caused by particles with high linear energy transfer (LET), e.g. heavy ions. The SEE is generated by direct ionisation along the particle path within the device. In this case, the more convenient energy loss metric is not particle energy but the LET, which is the rate of energy loss per unit length on a material. However, this scenario is not relevant for the LHC as only a negligible amount of high-LET ions actually reach electronic equipment.
- indirectly, the dominant source of SEEs at the LHC, caused by neutral or low-LET particles, predominantly hadrons.

Indirect ionisation can be further subdivided based on its root cause into those induced by high energy hadrons (HEH) and thermal-energy neutrons (THN), which shall be described in detail in the following sections. The total number of SEEs is then defined as the product of fluence ( $\Phi$ , in units of  $\text{cm}^{-2}$ ) and cross section ( $\sigma$ , in  $\text{cm}^2$ ), as:

$$N_{SEE} = \Phi_{THN}\sigma_{THN} + \Phi_{HEH_{eq}}\sigma_{HEH_{eq}} \quad (3.1)$$

As mentioned, the radiation hardness assurance (RHA) consists also in an SEE qualification approach,

based on the characterization of two cross sections: (i) 20-MeV protons (or equivalents fluxes at high-energy) and (ii) thermal neutrons with a kinetic energy of at least 0.025-eV, and it is schematically shown in figure 3.2.

Compared to TID, the implication is different as a single particle is capable of creating an observable effect in the device regardless of the irradiation history. For this reason, one is interested in evaluating the fluence of HEHs impacting the electronics.

### 3.3.2.1 Particle fluence

The mean free path  $\lambda$  denotes the average distance travelled by a particle in a material before an interaction, while its inverse  $\Sigma$  is the probability of interaction per unit distance, also called macroscopic cross section. Both  $\lambda$  and  $\Sigma$  are not only material dependent, but they also vary depending on the particle type and energy. For a stream of particles, that we shall assume to be identical, the number of interactions  $R$  occurring in a given time interval is equal to the total distance travelled  $l$  times the probability per unit distance  $\Sigma$ . For  $N$  particles:

$$R = Nl\Sigma \quad (3.2)$$

The reaction rate is then the derivative of this quantity:

$$\dot{R} = N \frac{dl}{dt} \Sigma = Nv\Sigma \quad (3.3)$$

where  $v$  is the average particle velocity. Assuming that the density of particles at spatial position  $r$  is  $n(r, v) = dN/dV$ , the reaction inside a volume element  $dV$  is:

$$\frac{d\dot{R}}{dV} = n(r, v)v\Sigma \quad (3.4)$$

The quantity  $\dot{\Phi}(r, v) = n(r, v)v$  is known as fluence rate or flux density, with dimensions of  $[m^{-3} m/s]$   $= [m^{-2}/s]$ . The time integral of the flux density yields the fluence:

$$\Phi(r, v) = n(r, v)dl \quad (3.5)$$

In practice, the fluence is measured in particles per  $cm^2$  and it describes the density of particle tracks. Computationally, it represents a track length estimation as:

$$\dot{\Phi}(v)dt = n(v)vdt = \frac{dN(v)}{dV} \frac{dl(v)}{dt} dt = \lim_{\Delta V \rightarrow 0} \frac{\Sigma_i l_i(v)}{\Delta V} \quad (3.6)$$

### 3.3.2.2 High energy hadrons

Hadrons are composite subatomic particles, made out of quarks (and antiquarks), such as protons, neutrons and pions. The high energy hadrons (HEH) term is employed in the R2E context to designate hadrons carrying enough energy to induce SEEs, usually in the order of MeVs through indirect ionisation. In general, charged hadrons under 20 MeV are considered not capable to generate SEEs, either due to their very low energy deposition or because they can not simply go through the component package. The 20 MeV limit does not have a universal physical mechanism, but depends on the device, and recent research [40] even points to a 1.5-3 MeV acute sensitivity for modern electronics.

Nevertheless, neutrons can still induce SEEs even at lower energies, and for this reason there is an energy dependent Weibull distribution for intermediate energy neutrons (0.2-20 MeV) and a function decreasing as  $E^{-1/2}$  for thermal neutrons, as expected for processes dominated by neutron capture<sup>1</sup>, as described in the next section.

The SEE response as a function of energy is assumed to be a Weibull function at 20 MeV as regards charged hadrons. The values of the Weibull parameters for the response function is device-specific (see Table 3.1 for typical values for R2E devices).

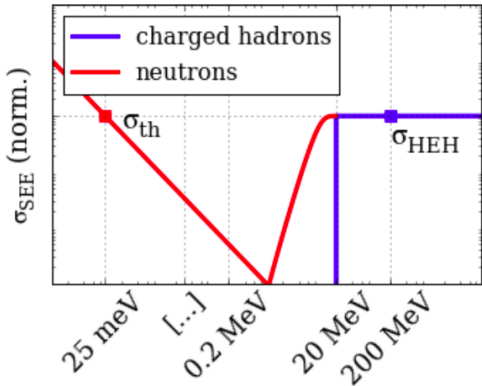


Table 3.1: SEE cross section and Weibull parameters of 32Mbit ISSI and 4Mbit Toshiba static random-access memory (SRAM).

	$\sigma_{\text{HEH}}^{\text{sat}}$ [cm <sup>2</sup> /bit]	$E_{\text{th}}$ [MeV]	$W$ [MeV]	$s$
Toshiba	$6.6 \cdot 10^{-14}$	0.2	9.25	3.02
ISSI	$1.4 \cdot 10^{-14}$	0.01	14.05	0.82

Figure 3.2: Charged hadrons and thermal neutrons cross sections as a function of the energy. [41].

Given their high energy, the local shielding mitigation technique is not effective. Moreover, they are more abundant in the LHC tunnel as compared to the shielded alcoves, where most electronics racks are located. For the case of protons, the energy deposition normally occurs via nuclear interactions, resulting in recoil ions which ionise the neighbourhood of the impact location. The response for a given

<sup>1</sup>An interpretation of this behaviour is: at thermal energies, the faster the neutron is the smaller its capture probability is until a point where other multiple mechanisms are activated and the cross section starts again to raise. Beyond the 20 MeV of energy threshold, hadrons have roughly a constant (independent from the energy) probability to be captured.

device is then convoluted with the mixed-field spectra, yielding the expected operational SEE rate, given as the HEH equivalent (HEHeq) fluence. More details concerning this approach can be found in Ref. [42]. Nevertheless, we summarise here the main equations.

The sum of the differential flux of hadrons above 20 MeV is defined as the high-energy hadron (HEH) flux and measured in  $\left[ \frac{\text{particles}}{\text{cm}^2 \cdot \text{s}} \right]$ .

$$\Phi_{HEH} = \int_{20\text{MeV}}^{\infty} \sum_{i=1}^{\text{hadron species}} \frac{d\phi_i(E)}{dE} dE = \int_{20\text{MeV}}^{\infty} \frac{d\phi_{HEH}(E)}{dE} dE \quad (3.7)$$

The fluence  $\left[ \frac{\text{particles}}{\text{cm}^2} \right]$  is obtained by integrating the flux over time:

$$\Phi_{HEH} = \int_{t_0}^{t_1} \int_{20\text{MeV}}^{\infty} \frac{d\phi_{HEH}(E)}{dE} dEdt = \int_{t_0}^{t_1} \phi_{HEH} dt \quad (3.8)$$

The high energy hadron equivalent flux considers the intermediate energy neutron contributions, defined as follows:

$$\phi_{HEHeq} = \int_{0.2\text{MeV}}^{20\text{MeV}} \frac{d\phi_n(E)}{dE} \cdot \sigma(E) dE + \int_{20\text{MeV}}^{\infty} \frac{d\phi_{HEH}(E)}{dE} dE \quad (3.9)$$

with the HEH equivalent fluence (HEHeq):

$$\Phi_{HEHeq} = \int_{t_0}^{t_1} \phi_{HEHeq} dt \quad (3.10)$$

with the general Weibull fit expression:

$$\sigma(E) = \sigma_{sat} \cdot \left( 1 - \exp \left[ - \left( \frac{E - E_{th}}{W} \right)^s \right] \right) = \sigma_{sat} \cdot w(E) \quad (3.11)$$

with typical values for the saturated cross sections  $\sigma_{sat}$ , threshold energy  $E_{th}$ , scale parameter  $W$  and shape parameter  $s$  in Table 3.1.

### 3.3.2.3 Thermal energy neutrons

Thermal energy neutrons (THN) with  $E \approx 0.25$  eV are responsible for soft SEEs only, e.g. through the  $^{10}B(n,\alpha)$  neutron capture reaction, as illustrated in Figure 3.3 and Ref. [43]. This process is typically more abundant in the shielded alcoves compared to the LHC tunnel and the R-factor (described in the next section) is meant to differentiate amongst such regions.

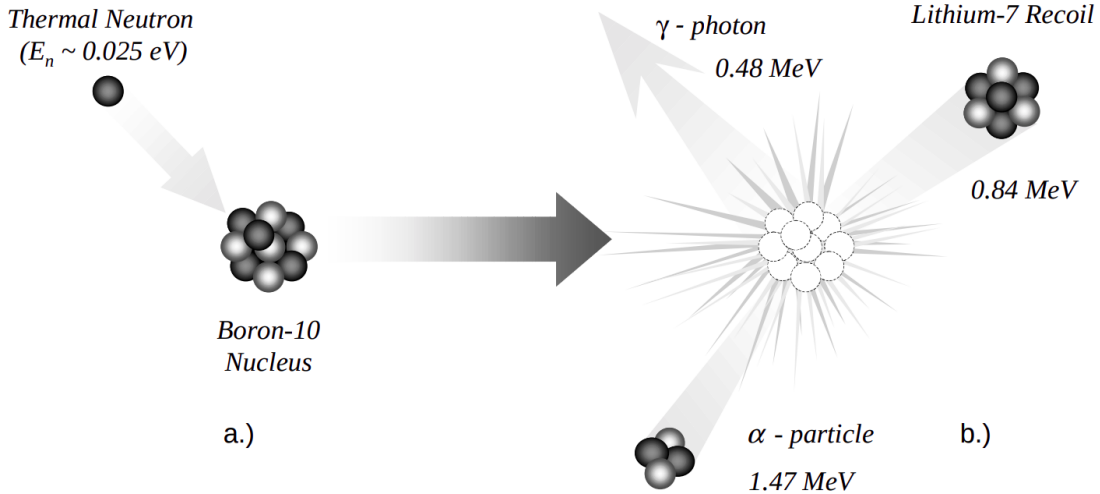


Figure 3.3: a)  $^{10}B$  nuclear fission with a thermal neutron, b) reaction products: photon,  $^7\text{Li}$  and the  $\alpha$  particle that will induce the SEU. [43].

The thermal neutron fluence is computed from the neutron flux  $\phi_{THN}$  with a weight equal the inverse of the square root of the energy  $w(E) = E^{-1/2}$ , leading to the first decreasing curve of Figure 3.2. This definition includes not only the 0.025 eV neutrons, but a wider spectrum:

$$\phi_{THN} = \int_0^{\infty} \sigma_{THN} \cdot w(E) \cdot \frac{d\phi_n(E)}{dE} dE \quad \Phi_{THN} = \int_{t_0}^{t_1} \phi_{THN} dt \quad (3.12)$$

### 3.3.2.4 R-factor

Another quantity usually investigated in the scope of R2E is the so-called risk factor (R-factor), a dimensionless quantity that expresses how many thermal neutrons relative to HEHeq are present as:

$$R = \frac{\Phi_{THN}}{\Phi_{HEHeq}} \quad (3.13)$$

Using this definition, one can invert equation 3.1 to estimate the HEHeq fluence from the number of SEU counts:

$$\Phi(HEH) = \frac{N_{SEU}}{R \cdot \sigma_{THN} + \sigma_{HEH}} \quad (3.14)$$

All LHC locations (both tunnel and shielded alcoves) are defined using the R-factor in order to assess whether the electronic component can survive in the radiation environment. The R-factor is evaluated either from experimental data (where radiation monitors were deployed) or from simulations, and is given in Table 3.2 [44].

Table 3.2: List of R-factors for the areas of interest for this thesis

Area	R-factor
Tunnel	1.5
RRs shielded	5
UJs shielded	10
ULs	10

### 3.3.2.5 Limitations

This HEHeq approach to estimate the SEEs presents the following limitations:

- The assumption that the HEH cross-section  $\sigma_{HEH}$  is constant at high energies is an approximation not always hold, as already indicated for pions in Ref. [45].
- The HEH cross section may depend on the hadron type. For example, pions have a cross section peak around 150 MeV, unlike protons, implying that the SEE rate can depend on the composition of the radiation field. The present consideration assumes that each hadron species contributes equally to the SEEs (see equation 3.7).
- It is important to assess the related risk of the neglected SEEs induced by direct ionisation from low-energy charged particles (such as electrons, muons, protons).
- The cross sections  $\sigma_{THN}$  and  $\sigma_{HEH}$  used for computing number of SEEs in equation 3.1 are measured in radiation test campaigns in specific conditions (energy, particle type), which can differ from the accelerator environment.



# Chapter 4

## Monitoring and Calculation

The analysis process leading to proposed radiation to electronics (R2E) mitigation techniques includes the monitoring of measured radiation levels (where monitors are available) and calculations based on detailed Monte Carlo simulations as well as comparisons (i.e. benchmarks) between the two, which is the scope of this thesis.

### 4.1 The monitoring and calculation working group at CERN

The purpose of the monitoring and calculation working group (MCWG) within the radiation to electronics (R2E) project is to provide to users or equipment owners the radiation levels in their desired locations. To address such requests, the aim is to understand the complexity and heterogeneity of the LHC radiation environment, as well as to identify the regions which are most affected by beam losses and should be followed up with the help of radiation monitoring systems. Example solutions of such requests are presented in Appendix Chapter C.

The LHC status is stored (in real-time, as well as for offline purposes), in the logging database (LDB) [46]. Raw meta-data from the LHC detectors (and more in general, for all the experiments) are available via Timeseries Information Masteing: Browsing, Extraction and Rendering (TIMBER) [47] and can be accessed using the CERN Accelerators Logging Service (CALS), and recently with its upgrade, the new CALS (NXCALS) [48]. This meta-data includes valuable quantities such as the delivered luminosity or beam intensity, as well as measurements for the radiation monitors.

For the analysis done within this thesis, the radiation monitor data is retrieved from TIMBER and post-processed (data filtering, curation, etc.) offline, as it is done for example for the beam loss monitor (BLM) dose rates in Ref. [49].

### 4.2 Radiation monitors employed at the LHC

The radiation monitoring sensors at the LHC consist of: over 400 radiation monitors (RadMON) and 4000 beam loss monitors (BLM). For Run 3 (but already for the interaction point IP1 in 2018 of Run

2), passive measurements done with the optical fiber detectors will also be used, with the advantage of a continuous spatial resolution for the detected radiation.

#### **4.2.1 Beam loss monitors**

Machine protection has driven the design and implementation of the beam loss monitor (BLM) system [50–52], with approximately 4 000 detectors placed along the accelerator. The BLMs are energy deposition detectors, that detect particle showers caused by the beam losses.

BLMs are capable of measuring total ionizing dose (TID) rates with a good time resolution of 40  $\mu\text{s}$  (one LHC turn is 89  $\mu\text{s}$ ), and acting on losses in 80  $\mu\text{s}$  to trigger beam dumps for critical losses to protect the machine equipment against unintended energy deposition, thereby preventing magnet quenches and damage of machine components.

Ideally, all the injected particles are used for collisions during stable beams operation. However, as explained in Chapter 2, part of them is lost along the machine and the BLM system aims to measure the loss pattern throughout the LHC. By observing the local aperture restrictions, system failures and other effects limit the performance of the LHC. In addition to the protective role, the BLM system is exploited (in offline analysis) for measurements and optimization of the accelerator, as they are employed to study the causes of the beam losses [21, 53], as is the scope of this thesis.

Beam losses can have different time duration [17]. Accordingly, the losses are measured and registered in 12 different moving windows known as running sums (RS), ranging from 40  $\mu\text{s}$  (the BLM time resolution) up to approximately 83.8 s. If the integrated TID exceeds a predefined value, a beam dump is triggered.

Simulations are performed to analyze the development of the particle showers initiated by lost protons in the most likely loss locations. It allows to determine the most suitable number and positions of the BLM detectors [54]. To summarise, there are BLM detectors placed after each set of collimators and quadrupole magnets. Other BLM detectors are located in the injection and dump insertions to monitor losses induced by system failures, or other special cases.

The detectors are placed outside the element they are "protecting", approximately 1 m downstream of the most likely loss locations, as it corresponds to the location of the particle shower maxima. Therefore, the signal given by the detectors is generated by the energy deposition of the particle showers, which is linear with the primary losses. This detector distribution has proven to be the optimal one to localize the losses as well as to distinguish between the two beams [54].

It is essential to correlate the BLM signal, generated from the detection of the shower particles, to the primary beam lost protons. This is often calculated considering different loss scenarios (see Section 2.4 and Appendix Chapter B) via simulation techniques. These simulations are also used to determine the energy deposition in the machine components from lost protons. Depending on the loss scenario beam losses are expected to be either very small, as at the magnets quench levels, or very large, as at the collimation or dump interaction regions (IR).

The main detector type of the LHC BLM system is an ionization chamber (IC), of which there are approximately 3 600 monitors. They are made of a stainless steel cylindrical tube, 50-cm long, and with a diameter of 9 cm, leading to an active volume of 1.5 l filled with  $N_2$  at an overpressure of 100 mbar. The chamber contains parallel aluminium electrodes plates with a thickness of 0.5 mm equally spaced by 0.5 cm that are alternatively used as high voltage and signal electrodes. A voltage of 1.5 kV is applied between the electrodes, which generates an electric field of 3 kV/cm inside the chamber.

In regions where higher losses are expected, two other types of monitors, secondary emission chambers (SEM) and little ionizing chamber (LIC), are installed in order to achieve a higher dynamic range and cover the risk of saturation of the ICs electronics.

Both SEMs and LICs have the same geometry and design as the ICs, but their chambers are shorter (approximately 10-cm long) and have only 3 electrodes: the middle one is the signal electrode and the other two are the high voltage ones. The LICs have in general the same properties as the ICs, but their reduced volume makes them approximately 60 times less sensitive. In contrast, in the SEM detectors the signal electrode is made of titanium to enhance the emission of secondary electrons. Additionally, the SEM chamber is under vacuum, with a pressure below  $10^{-7}$  bar, making it approximately  $3 \cdot 10^4$  times less sensitive than the IC detectors [52]. Considering ICs, LICs and SEMs there are approximately 4 000 BLM detectors in total located in the LHC.

The ICs and LICs convert the particle shower caused by mislead protons into an electric current by the principle of ionization. The charged shower particles ionize the  $N_2$  gas inside the chamber as they traverse it. The high electric field applied between the electrodes causes the resulting electrons and ions to drift to the corresponding electrode. This movement induces a signal current with amplitude proportional to the beam loss rate.

The principle of the signal generation in SEM chambers is slightly different. It is based on the secondary electron emission from solids. The path followed by a charged particle through the signal electrode, made of titanium, causes secondary electrons to escape from its surface layers. They are subsequently drifted away as a result of the high voltage applied to the bias electrodes, which induces the signal current [55].

#### 4.2.2 Radiation monitors

In total, roughly 400 radiation monitors (RadMONs) [56] are placed in strategic locations around the LHC tunnel and its adjacent shielded areas to monitor the radiation field relevant to radiation induced failures in LHC electronics [57]. The RadMON detectors provide measured data on the total ionizing dose (TID) by means of RadFETs, displacement damage (DD) by the means of p-i-n diodes and high energy hadron equivalent (HEEq) fluence (for particle energies above 20 MeV) by counting single event upsets (SEU) of SRAM memories.

The RadMON was developed at CERN in the engineering (EN) department. The first generation of RadMON deployed in the LHC (referred to as V5) has 9 radiation sensors on the board: 2 radiation sensitive p-channel MOSFETs (RadFETs) with different oxide thicknesses (100 nm, 400 nm and 1000

Table 4.1: RadMON V5 cross sections for high energy hadrons and thermal energy neutrons

Bias [V]	$\sigma_{THN}$ [cm <sup>2</sup> /bit]	$\sigma_{HEH}$ [cm <sup>2</sup> /bit]
5	$3.1 \cdot 10^{-15}$	$3.0 \cdot 10^{-14}$
3	$1.7 \cdot 10^{-13}$	$7.0 \cdot 10^{-14}$

nm) for the TID measurements, 3 photodiodes in series for the measurements of 1 MeV equivalent neutron fluence and a Toshiba SRAM memory to measure the cumulative fluence of hadrons with energy higher than 20 MeV (HEHeq) and thermal energy neutrons (THN) through different voltage settings. [57]

Obsolescence of several components used for the RadMON V5, feedback from the on-field usage of the monitor in Run 1 of LHC operation (2010-2012), and, in particular, new monitoring requirements lead to the launch of a new design of the RadMON (referred to as V6) [56], which aims at resolving issues and limitations experienced with the previous version. The main developments are: higher radiation tolerance (more than 200 Gy, as opposed to the 80 Gy for V5), modular architecture for easy replacement of parts and updates, remote configurability and improved measurement accuracy. On the sensor side, the RadFETs and the pins are the same as for V5, but the Toshiba SRAMs are now paired with 4 chips of Cypress 40 nm SRAM, which are insensitive to thermal neutrons. The use of two memories with different sensitivities to thermal neutrons allow the direct evaluation of the R-factor.

The RadMONs can be operated at two different voltage settings in order to achieve different sensitivities to both thermal neutrons and high-energy hadrons. The Toshiba memories become significantly more sensitive to thermal neutrons when it operates a 3 V bias voltage compared to 5 V, as indicated by the cross section from Table 4.1. All the RadMONs deployed in the tunnel are biased at 5 V and an *R* factor of 1.5 is considered. Reports on RadMON measurements can be found for p-p (proton) runs in Ref. [58], while for the Pb-Pb and p-Pb runs in Ref. [44].

Regarding the position of the RadMONs, the locations are not exactly the same in all the cells and points. All the RadMon installed in the tunnel are reported on CERN's "GIS machine map" (Machine/Equipment/RadMons) [59, 60]. In the ARC regions, the RadMONs are placed under the interconnection between the last bending magnet (quadrupole) of a given cell (where usually the electronic equipment are placed) and are deployed until cell 21. The RadMon in the shielded areas unfortunately are not included in the machine map, but their exact locations are collected in the drawings in the CERN database, and readily reported in the Appendix of Ref. [58].

### 4.2.3 Optical fibre sensor

Within the radiation to electronics (R2E) project, a distributed dosimetry sensor based on radiation sensitive optical fibers (OFs) allowing to perform online and distributed dosimetry measurements has been developed. Presently, it is deployed in the proton synchrotron booster (PSB) [61] and proton

synchrotron (PS) with LS2 plans to deploy in SPS and LHC dispersion suppressor (IP1, IP5 and IP7), and it had already been installed in IP1 DS in 2018.

The OF radiation sensor of choice is a p-doped OF privately produced by iXBlue Photonics [62], investigated the accelerator environment usage in Ref. [63, 64]. The interest in this technological solution is not only thanks to the possible cost/performance advantages, but also to the technical benefits with respect to the point dosimetry systems currently employed at CERN. The optical fibre allows to perform online and distributed dosimetry measurements, and it is well adapted to be employed in long accelerators, running parallel to the beamline. It provides a linear map of the cumulated radiation dose with a spatial resolution of 1 m [65].

## 4.3 FLUKA simulations

FLUKA [66–68] (FLUktuierende KAskade) is a general multi-purpose particle interaction and transport Monte Carlo code that is capable to handle a wide variety of radiation sources. It can produce and transport neutrons from thermal energies and all other particles from 1 keV upwards to cosmic ray energies. It is applied in different fields [34], and in the context of this thesis, it is employed to calculate the radiation levels resulting from proton-proton collisions at LHC energies and proton-target collisions at the CERN high energy accelerator mixed field (CHARM) facility. Regarding its physics models, it correctly describes the entire hadronic and electromagnetic particle cascade initiated by secondary particles from TeV energies. An essential feature is that it provides direct scoring capabilities to estimate in detail the possible risk of radiation damage to electronics: total ionizing dose (TID), high energy hadron (HEH and HEHeq) and thermal energy neutron (THN) fluences.

### 4.3.1 The Monte Carlo method for simulations of radiation-matter interactions

The Monte Carlo (MC) method is a technique of numerical analysis, based on sequences of random numbers used to obtain sample values for the variables for a given problem. The calculation process used in MC is an artificial construct, usually a computer program that is mathematically equivalent to the problem being analysed [69]. Compared to traditional methods with converging efficiency of  $1/\sqrt{N}$ , MC converges with  $1/\sqrt{N}$ , thereby being more efficient when the dimension of the problem is larger than 2. MC is now used routinely in many different fields, from the simulation of complex physical phenomena such as radiation transport in the earth atmosphere to the simulation of the esoteric sub-nuclear processes in high-energy physics experiments.

Particle transport is described analytically by the Boltzmann equation. It can be seen as a balance equation in phase space: the increment of particle phase-space-density is equal to the sum of all “production terms” (such as particle production, sources, decay and “in-scattering”) minus the sum of all “destruction terms” (such as decay, “out-scattering” and absorption), at any phase-space-point.

Solutions of different type can be explored: at a number of (real or phase) space points, averages over (real or phase) space regions, projected on selected phase space hyper-planes, stationary or time-

dependent. Once the problem is defined, the random walk of the particles through the problem geometry can be executed.

Before the explicit computations for the simulation can begin, the user must define the problem, usually consisting of the following steps [69]:

1. Geometry and material definition.
2. Source terms (e.g. a proton beam with a specific position, energy, time and direction of travel).

The Monte Carlo code (in this case FLUKA) will handle the:

1. Random sampling of the outcome of physical events according to an appropriate probability distribution.
2. All the secondaries from the same primary are transported before a new history is started.
3. Computation of the response: the results of the random walk are used to calculate the quantity of interest and its statistical uncertainty.

The values of the random variables are distributed according to a probability distribution function.

The main assumptions of the particle transport MC that allow it to be used in the radiation-matter scenario are:

- static, isotropic, homogeneous and amorphous media (and geometry).
- transported particles do not interact with each other.
- particles do interact with individual molecules/nuclei/atoms (this assumption is invalid at low energies, especially for neutrons).
- Markovian process: the fate of a particle depends only on its actual properties, not on previous events or histories.
- material properties are not affected by particle reactions.

The accuracy and reliability of a MC code depends on the models or data on which the probability distribution functions are based. Instead, the statistical precision of the results depends on the number of histories and its convergence can be accelerated by “biasing” techniques.

### **4.3.2 FLUKA physics models and capabilities**

An overview of the FLUKA physics models can be found in its online manual and references [66]. A very short summary will be given here to highlight the main interactions of interest for this thesis.

The main source of radiation in the LHC tunnel around the interaction points (in this thesis, IP1 and IP5) are collision debris from the interaction point. Therefore, we distinguish first between hadron-

hadron interactions at the IP and hadron-nucleon interaction along the tunnel, both categories being simulated by different event generators depending on the energy (and projectile). For inelastic hadron-hadron interactions:

- For momentum  $< 20 \text{ TeV}/c$  and  $> 5 \text{ GeV}/c$ : dual parton model (DPM) [70]
- Momentum from lower particle threshold to  $5 \text{ GeV}/c$ : Resonance production and decay model [71]

The inelastic hadron-nucleon interactions:

- Momentum  $< 20 \text{ TeV}/c$  and  $> 5 \text{ GeV}/c$ : Glauber-Gribov multiple scattering followed by generalized intranuclear cascade (GINC)
- Below  $5 \text{ GeV}/c$  for nucleons, anti-nucleons and pions; below  $1.5 \text{ GeV}$  kinetic for kaons: Preequilibrium-cascade model PEANUT [72, 73]. In between PEANUT and DPM for kaons [74].

All three models above include evaporation and gamma deexcitation of the residual nucleus [75].

This thesis focuses on energy deposition in several radiation detectors, and hence a brief overview of the energy loss mechanisms is provided below. Amongst many mechanisms, we highlight the:

- Bethe-Bloch theory [76], Barkas  $Z^3$  [77] and Bloch  $Z^4$  effects [78].
- Mott correction to the Rutherford scattering cross section [79].
- Ranging out particles below energy cutoff, handling of porous substances and improved ionisation potential.
- Shell and other low-energy corrections derived from Ref. [80].
- Ionisation potentials and density effect parameters [81].
- Accurate treatment of curved trajectories and boundaries in magnetic and electric fields.
- Bremsstrahlung at high energy by heavy charged particles, also with electron pair production.

A special note has to be done for low-energy neutrons ( $E < 20 \text{ MeV}$ ). FLUKA uses its own neutron cross section library ( $P_5$  Legendre angular expansion, 260 neutron energy groups [81]), containing more than 250 different materials. In particular, the transport of proton recoils and protons from  $^{14}\text{N}(\text{n},\text{p})^{14}\text{C}$  reaction, relevant as they occur in the  $N_2$  present in air and in the BLM active volume.

#### 4.3.3 FLUKA usages

An integral part of the FLUKA code development is the benchmarking of the validity of its physics models and new features against experimental data over a wide energy range, which includes the comparison of predictions of individual models to measurement results (such as particle angular distributions and multiplicities). In the scope of this thesis, the FLUKA physics is assumed to be accurate,

and any discrepancy observed in the benchmarking of the complex application to the LHC is more likely due to geometrical effects or a non-ideal understanding of the beam loss mechanisms.

In the more general context of R2E at CERN, FLUKA has been extensively used not only for the experimental areas, but also to address electronics failures at intensive beam loss regions around the LHC accelerator, but also in the ARC regions. As presented in Chapter 3, the radiation damage to electronics can be divided into two categories: (i) cumulated (dose and displacement) damage will limit the lifetime of the electronics installed in the LHC tunnel (ii) whereas the alcoves are equipped with commercial (or not specifically radiation tolerant) electronics, which are mostly affected by the risk of SEEs.

The simulation data are continuously reevaluated to predict the radiation levels for several LHC operational conditions (in particular the nominal configuration), as well as for feasibility studies for future colliders (mostly for the High Luminosity LHC upgrade). The R2E aim is to provide specifications on the maximum fluence/dose values for each critical underground area, taking into account the related uncertainties (such as assumptions in operational constraints, equipment sensitivities, etc.). A safety rule of thumb is that the values obtained by the simulation benchmarking should rather overestimate measured data, rather than underestimate.

The outcome of such studies represents the starting point in the environment parametrization and radiation hardness qualification requirements that need to be fulfilled by considered electronic devices meant to have a reliable operation.

At CERN, in addition to R2E, FLUKA is extensively used for machine protection issues such as energy deposition or power calculations and studies of material damage to accelerator beamline elements [82, 83].

#### **4.3.4 Geometry construction tools**

The FLAIR tool [84, 85] is an advanced graphical user interface for particle simulation programs that eases the geometry construction for the user. Initially for FLUKA, the interface is now separated from the functionality permitting an easy integration of other simulation packages, such as FLUKA, Geant4 [86–89], PENELOPE [90], and other simulations engines.

Considering the complexity of the LHC accelerator, several tools have been developed that help the user to build the simulation files. In order to implement the geometry, FLUKA Element Database (fdb) and the linebuilder (LB) have been used [91]. The fedb is a database containing the FLUKA geometry models of different accelerator components (such as magnets, collimators, absorbers, BLMs, etc.), which are used with a modular approach to build the whole line. These elements, together with the tunnel, are implemented based on the CERN Drawing Directory [92]. The LB is a Python-based tool for assembling accelerator beam lines for FLUKA simulations (such as LHC, SPS, SPS). In particular, it allows to arrange accelerator components from fedb on the basis of TWISS file information [93]. The radiation monitors are not beamline elements, but can be added as additional components to

LineBuilder by specifying their position (and orientation). This information has been extracted from the CERN layout database (LDB) [94], and visually double checked with the GIS portal [60].

#### **4.3.5 Simulation uncertainties**

There are a number of errors and uncertainties associated with the Monte Carlo method and computational physics. Within the scope of this thesis based on FLUKA calculations, we mention:

- The main contributing factor is the accuracy of the geometry. This is in term of position of objects inside the main simulation geometry, materials and dimensions.
- There needs to be considerations for the test device itself, as the size of the sensitive volume may be too small for the low energy particle thresholds used in the computations.



## Chapter 5

# CHARM Facility Simulations and Comparison with Data

The CERN High Energy Accelerator Mixed-field (CHARM) facility [95] is a unique irradiation infrastructure as it provides a complex mixed radiation field similar to that present in the LHC accelerator and its surroundings. Its multiple applications include the characterization of electronic devices and systems and the calibration of radiation detectors, used for CERN accelerators, but also available to users from the wider aerospace community and beyond. Generally, CHARM is considered a more controlled environment that can be more easily studied compared to the large hadron collider (LHC) scenario. Therefore, it is used in the scope of this thesis as a calibration study to quantify the level of agreement between simulation and data for a radiation monitor in a complex radiation field.

The radiation environment of the CHARM facility has been studied in different contexts. Particularly relevant within the scope of this thesis are those pertaining to the deposited energy spectra in silicon [96] and the single event effects (SEE) flux calibration of detectors [97] by high-energy neutrons and in mixed fields. In addition, other dedicated analyses have been carried out for: (i) the thermalization process of secondary neutrons, measured using the gold foil activation method with bare and Cd-covered gold foils [98] (ii) the attenuation profiles of neutrons in concrete and steel, measured using an NE213 scintillator [99], (iii) activation, measured using activation detector sets consisting of aluminum, niobium, indium, and bismuth [100].

The goal of this work is to make a systematic analysis of the agreement between simulated and measured radiation levels at CHARM using a set of three radiation monitors employed for radiation to electronics (R2E) studies at CERN. For this purpose, the radiation levels are simulated using the FLUKA Monte Carlo code (version 4.1.1) and compared against measurements performed with: (i) two beam loss monitors (BLMs) [50], (ii) the RadMON system at different possible locations [56], (iii) 60 m of distributed optical fiber dosimeters (OF) [64].

### 5.1 The CHARM facility

While an exhaustive description of the CHARM layout, operation and beam parameters can be found in Ref. [95], we summarise here the main features relevant for our study. The radiation field is generated

by a 24-GeV proton beam, extracted from the proton synchrotron (PS) accelerator, hitting a metallic target (or alternatively, without any target) shaped as a 50 cm long cylinder with a diameter of 8 cm, and it is used to test electronic components and systems at predefined test positions (see Figure 5.1). Different target and shielding configurations are available in order to produce a secondary field with a broad range of radiation intensities, compositions and spectra:

- target material (in decreasing density): copper (cp), aluminium (al), sieved aluminium/aluminium with holes (alh). The lower the target material density, the lower the secondary field intensity.
- shielding configuration: four movable blocks with a size of  $20 \times 214 \times 350 \text{ cm}^3$  (width/height/length). They can be placed between the target and the test locations in different combinations (see Figure 5.1). The outer ones are made of concrete (C) and the two inner ones of stainless steel (S).

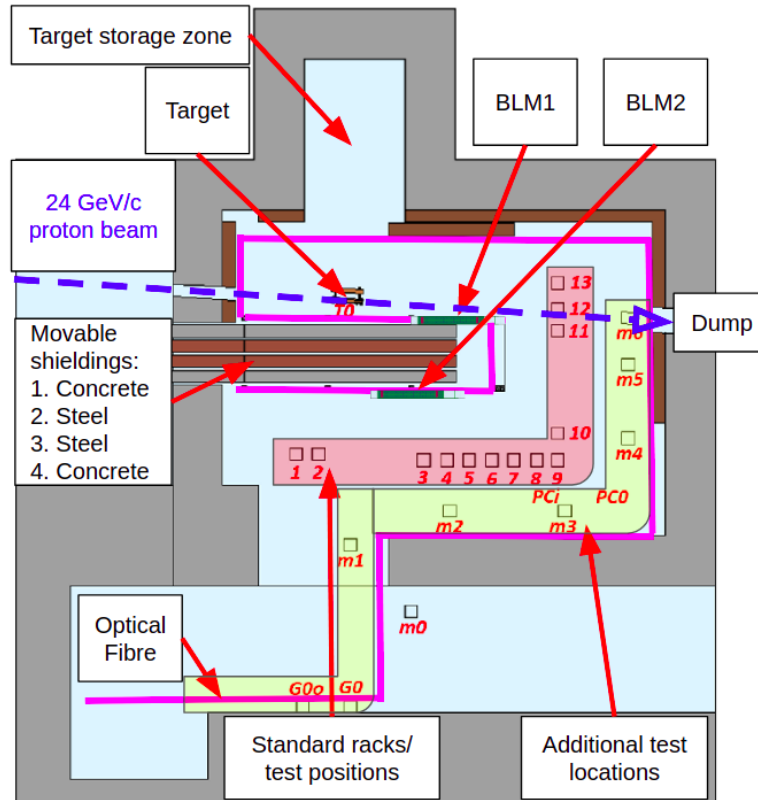


Figure 5.1: Top view of FLUKA geometry of the CHARM test area. Two BLMs are installed 1 m above beam height, one next to the target and one behind the movable shieldings. There are 13 racks (standard test locations) at beam height where RadMONs can be deployed, with additional positions distributed in the test area. An optical fibre sensor was mounted along the walls and the movable shieldings.

In order to designate a specific configuration, an acronym is used. For example, the copper target with no shielding configuration is referred to as cpOOOO, while with full shielding as cpCSSC.

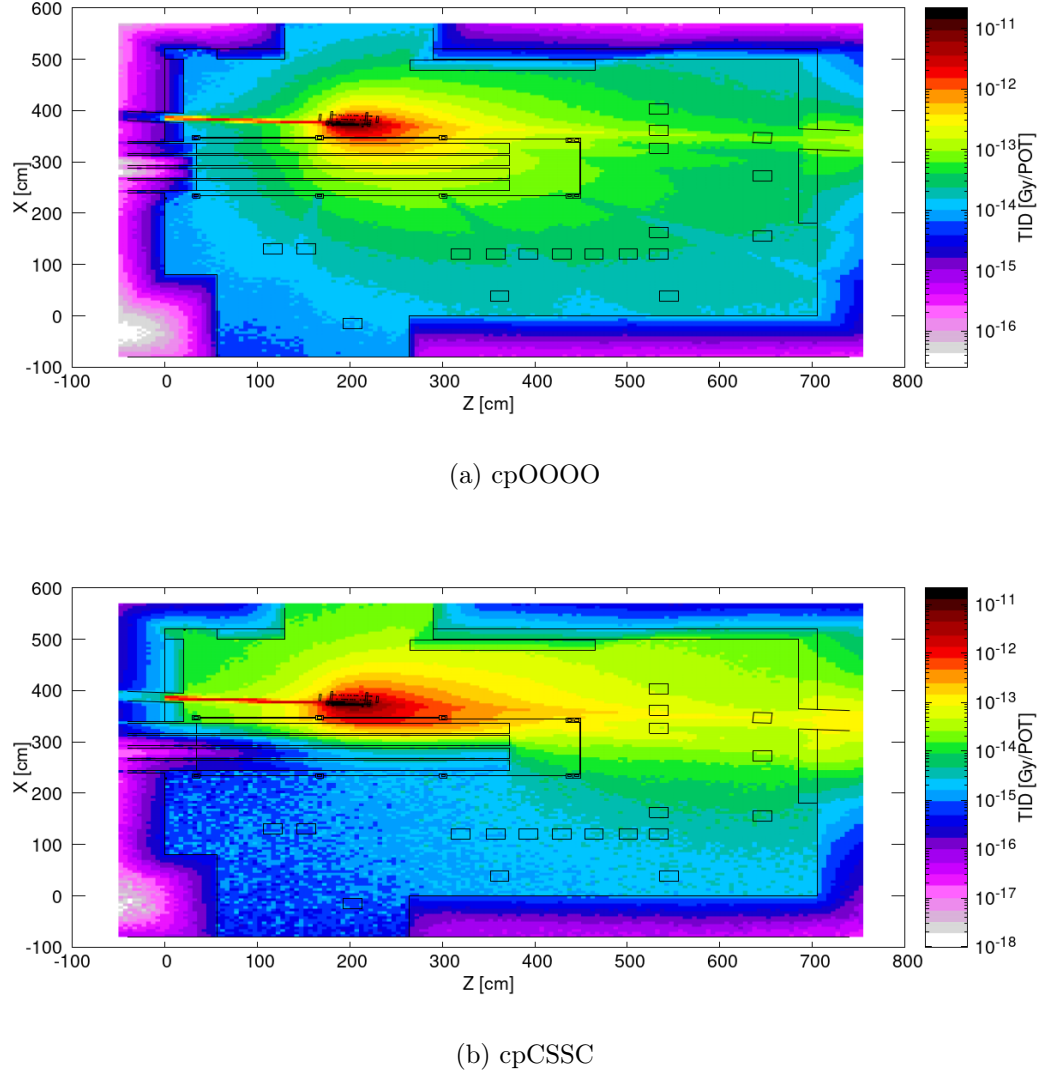


Figure 5.2: The simulated 2D TID distribution at beam height is shown for two configurations: cpOOOO (top) and cpCSSC (bottom).

## 5.2 FLUKA simulation of the CHARM facility

The radiation environment of the CHARM facility is simulated using the Monte Carlo code FLUKA (described in Section 4.3), capable of calculating R2E-relevant quantities. A full model of the experimental setup was implemented (see Figures 5.1 and 5.2, where the latter includes also a simulated 2D map of TID at beam height) using the FLAIR tool (described in Section 4.3.4).

Generally, the bodies in the geometry, including the test positions, can be considered to be accurate within 1-2 cm. This accuracy is particularly important due to the radiation gradient, e.g. the radiation field can vary up to 1% per centimetre in positions close to the beam axis [101]. This also implies that the physical size of the test equipment needs to be considered when choosing the test position with the facility.

The geometry updates/evolution was documented in dedicated accelerator and technology sector (ATS) notes [42, 101]. Compared to the simulation model previously used in Ref. [95], the main updates in the geometry consist in improving the material properties (especially the concrete density, relevant for thermalization of neutrons) and the explicit modelling of two beam loss monitors (BLMs) [50] and of the optical fibre sensor [64].

## 5.3 Similarities between CHARM and the accelerator environment at the LHC

The radiation environment of the LHC is well reproduced at CHARM, as previously confirmed in Ref. [95] for the case of the LHC shielded alcoves hosting electronics, with the main handicap of lacking the very high-energy ( $> 24$  GeV) particles. This is further confirmed by Figure 5.3, that compares the particle spectra for several particle species in the BLMs at CHARM and at the LHC, installed on the accelerator in the tunnel, allowing to reach similar conclusions. The exhaustive description of the LHC environment is provided in Section 6.1.2, with more information about the BLM deployment in the LHC geometry in Section 6.4.1).

## 5.4 Radiation monitors calibration benchmarks

This section presents the results of the comparison between FLUKA simulations and data of radiation monitors, normalized to the number of primary protons on target (POT). Typical POT figures at CHARM are of approx.  $5 \cdot 10^{11}$  protons/spill and  $1.5 \cdot 10^{16}$  protons/week.

### 5.4.1 Beam loss monitor benchmark

As anticipated, the CHARM experimental area includes two beam loss monitors (BLMs) that measure the absorbed dose (in Gy) deposited in a nitrogen-filled volume by the radiation showers through ionisation.

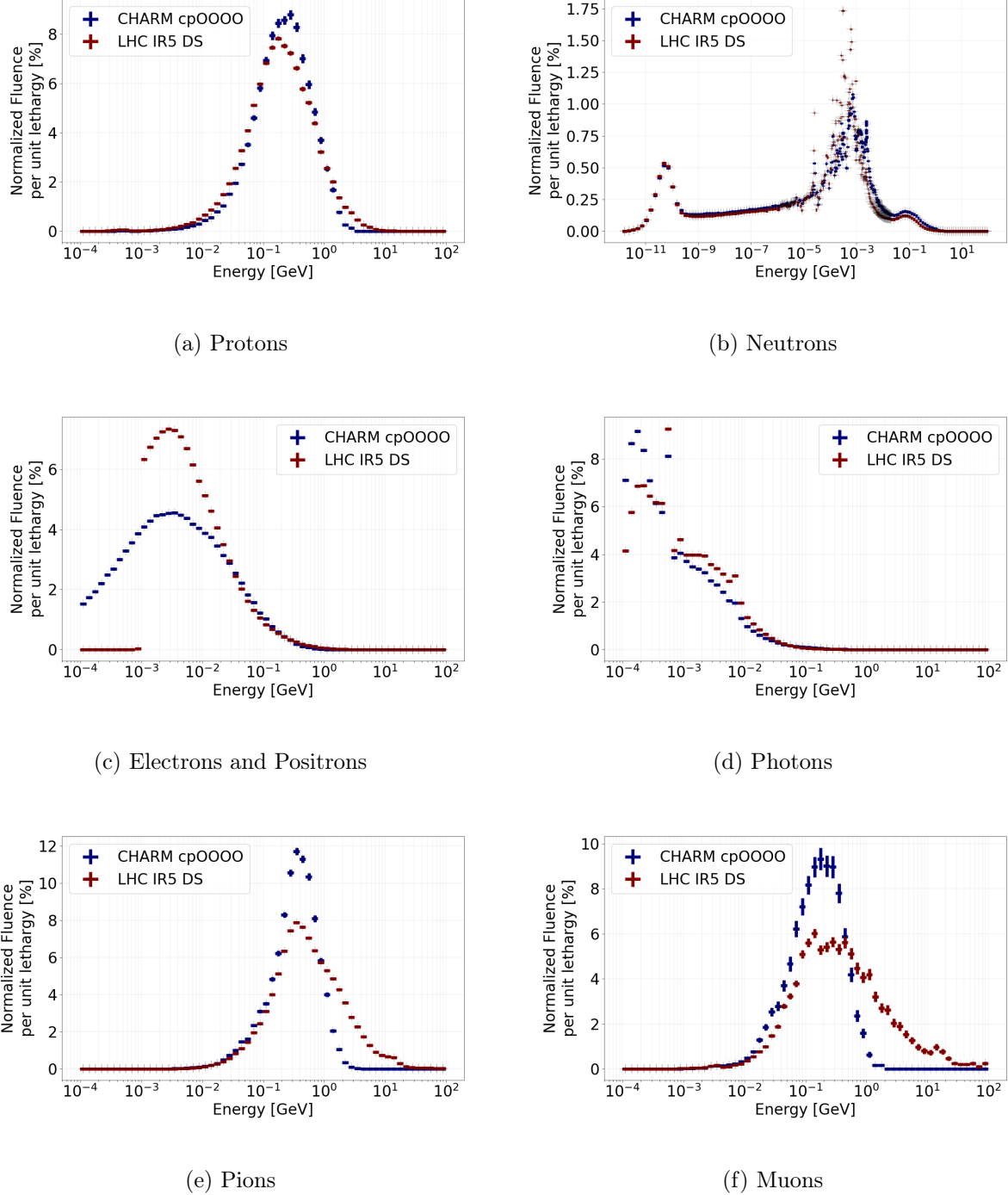


Figure 5.3: Comparison of the particle spectrum scored in the active volume of the BLMs between CHARM and LHC interaction point (IP5) dispersion suppressor (DS) for several particle species, in lethargy format. The electrons and positrons have different lower energy cutoffs: at  $10^{-4}$  GeV at CHARM and  $10^{-3}$  GeV at the LHC, to speed up computational convergence.

Table 5.1: Comparison of measured and simulated BLM TID values, as well as their ratios, for the three targets: copper (cp), aluminium (al) and aluminium with holes (alh), and the used shielding configurations (CONF.). The proton on target (POT) is an indicator of how much (in absolute terms) the respective configuration has been used: mostly cpOOOO for the high intensity and cpCSSC and alhCSSC for low intensities. The last row of each table presents the average ratio of the measured to simulated values and their standard deviation.

(a) Copper target

CONF.	POT	BLM1			BLM2			BLM1/2 ratio		
		measured [Gy/POT]	simulated [Gy/POT]	measured/ simulated	measured [Gy/POT]	simulated [Gy/POT]	measured/ simulated	measured	simulated	measured/ simulated
cpOOOO	3.14E+17	4.74E-14	5.33E-14	0.89	2.39E-14	3.22E-14	0.74	1.98	1.66	1.20
cpOOOC	4.53E+13	5.86E-14	5.34E-14	1.10	2.01E-14	3.36E-14	0.60	2.92	1.59	1.84
cpCOOO	3.21E+13	5.96E-14	5.64E-14	1.06	1.21E-14	1.10E-14	1.10	4.93	5.14	0.96
cpOOSC	1.73E+13	5.92E-14	5.49E-14	1.08	4.27E-15	5.52E-15	0.77	13.86	9.95	1.39
cpCSOO	8.46E+14	5.06E-14	5.66E-14	0.89	2.32E-15	3.13E-15	0.74	21.81	18.09	1.21
cpOSSC	1.83E+13	5.97E-14	5.58E-14	1.07	2.67E-15	2.87E-15	0.93	22.36	19.45	1.15
cpCSSO	9.00E+14	5.99E-14	5.76E-14	1.04	2.03E-15	2.44E-15	0.83	29.51	23.62	1.25
cpCSSC	2.46E+16	5.20E-14	5.80E-14	0.90	1.71E-15	2.99E-15	0.57	30.41	19.37	1.57
AVG		$1.00 \pm 0.09$			$0.79 \pm 0.17$			$1.32 \pm 0.27$		

(b) Aluminium target

CONF.	POT	BLM1			BLM2			BLM1/2 ratio		
		measured [Gy/POT]	simulated [Gy/POT]	measured/ simulated	measured [Gy/POT]	simulated [Gy/POT]	measured/ simulated	measured	simulated	measured/ simulated
alOOOO	2.18E+14	3.93E-14	3.62E-14	1.09	1.34E-14	1.35E-14	0.99	2.93	2.68	1.09
alCSOO	3.41E+14	4.20E-14	3.89E-14	1.08	1.39E-15	1.79E-15	0.78	30.22	21.72	1.39
alCSSC	5.19E+14	4.19E-14	3.85E-14	1.09	9.62E-16	1.41E-15	0.68	43.56	27.28	1.60
AVG		$1.08 \pm 0.01$			$0.82 \pm 0.16$			$1.36 \pm 0.25$		

(c) Aluminium with holes target

CONF.	POT	BLM1			BLM2			BLM1/2 ratio		
		measured [Gy/POT]	simulated [Gy/POT]	measured/ simulated	measured [Gy/POT]	simulated [Gy/POT]	measured/ simulated	measured	simulated	measured/ simulated
alhOOOO	6.25E+14	1.35E-14	2.00E-14	0.67	4.63E-15	8.05E-15	0.57	2.92	2.49	1.17
alhCOOO	1.12E+13	1.46E-14	2.09E-14	0.70	2.49E-15	3.74E-15	0.67	5.86	5.59	1.05
alhCSOO	2.83E+13	1.45E-14	2.11E-14	0.69	5.34E-16	1.06E-15	0.50	27.15	19.85	1.37
alhCSSO	3.03E+14	1.42E-14	2.09E-14	0.68	4.27E-16	7.19E-16	0.59	33.26	29.15	1.14
alhCSSC	9.95E+15	1.40E-14	2.12E-14	0.66	3.92E-16	6.59E-16	0.59	35.71	32.14	1.11
AVG		$0.68 \pm 0.01$			$0.59 \pm 0.06$			$1.17 \pm 0.12$		

A comparison between BLM TID measurements and simulations, obtained with a full modelling of

the BLMs in the FLUKA geometry, is presented in Table 5.1, showing separately the two BLMs for each configuration. Owing to the medium-sized simulation geometry of the CHARM facility and the computational resources available, enough primaries have been generated to yield simulated statistical errors of below 1%. Regarding measured signal from the BLMs, it is considered that gain variations between 1% and 5% are to be expected [17].

The results exhibit a good level of agreement, always within 40%, and often much better for individual configurations. The average ratio of the measured values over FLUKA simulated ones for all configurations is of  $0.92 \pm 0.18$  (standard deviation) for the highly irradiated BLM1,  $0.73 \pm 0.17$  (i.e. 27% simulation overestimation) for the more shielded BLM2 and  $1.28 \pm 0.23$  for the ratio of the two.

Considering these results in a conservative manner, the worse agreement of the BLM2 is taken as a reference and from it, a systematic error of 30% is subsequently considered in the LHC scenario for the BLM benchmark.

#### 5.4.2 RadMON benchmark

The CHARM facility includes a set of RadMON detectors measuring key R2E-relevant quantities, including: (i) HEHeq fluence, i.e. fluence of  $E > 20$  MeV hadrons plus an “equivalent” contribution of intermediate-energy ( $0.2 - 20$  MeV) neutrons with energy-dependent Weibull weights, (ii) thermal neutron equivalent fluence (THNeq) where neutrons are weighted proportionally to the inverse of their velocity, and (iii) total ionic dose (TID). The corresponding simulated values of the aforementioned quantities can be freely accessed using an online toolkit [102].

##### 5.4.2.1 Fluence results

The above fluences are calculated in FLUKA in  $20 \times 20 \times 20$  cm<sup>3</sup> volumes in the positions of interest without explicitly modelling the geometry of the RadMON detectors, unlike the case of the BLMs: this choice is motivated by the small size of the RadMON and by the fact that, compared to the TID, the hadron fluences are expected to be less dependent on the material and detector geometry.

Depending on the location (see Figure 5.1), the RadMONs (or in user operation, the test equipment) are exposed to a radiation field with different composition and particle energy spectra. In positions closer to the beam, the field contains a large amount of charged hadrons with particle energies extending up to the GeV range. In positions perpendicular to the target, the spectrum is “softer” [103], as the environment contains lower energetic particles, mostly neutrons, as they span to lower energies than charged hadrons. When the shielded configuration is employed, the relative amount of thermal neutrons is further enhanced. This feature of the CHARM facility allows the users to exploit a wide range of R-factors, which is a dimensionless quantity defined as the ratio of thermal neutrons to high energy hadrons. It is used to indicate the “softness” (the greater the R-factor, the “softer”) of the radiation field.

Table 5.3: Comparison of RadMON data with FLUKA results for the copper target. Note that RadMONs have not been experimentally deployed at all possible test locations; nevertheless, FLUKA allows for estimating the desired set of R2E quantities. The last row presents the average data/FLUKA ratio values and their standard deviation.

(a) cpOOOO

LOC.	High Energy Hadrons equivalent			Thermal Neutrons equivalent			R-factor		
	measured [cm <sup>-2</sup> /POT]	simulated [cm <sup>-2</sup> /POT]	measured/ simulated	measured [cm <sup>-2</sup> /POT]	simulated [cm <sup>-2</sup> /POT]	measured/ simulated	measured	simulated	measured/ simulated
R1	1.85×10 <sup>-05</sup>	3.47×10 <sup>-05</sup>	0.53	5.48×10 <sup>-05</sup>	1.20×10 <sup>-04</sup>	0.46	2.44	5.91	0.41
R4	4.28×10 <sup>-05</sup>	5.13×10 <sup>-05</sup>	0.83	3.90×10 <sup>-05</sup>	1.26×10 <sup>-04</sup>	0.31	0.91	3.29	0.28
R5	3.49×10 <sup>-05</sup>	4.40×10 <sup>-05</sup>	0.79	4.60×10 <sup>-05</sup>	1.27×10 <sup>-04</sup>	0.36	1.32	3.78	0.35
R7	4.32×10 <sup>-05</sup>	4.72×10 <sup>-05</sup>	0.92	4.43×10 <sup>-05</sup>	1.26×10 <sup>-04</sup>	0.35	1.03	3.37	0.31
R9	2.96×10 <sup>-05</sup>	4.35×10 <sup>-05</sup>	0.68	5.86×10 <sup>-05</sup>	1.24×10 <sup>-04</sup>	0.47	1.98	3.54	0.56
R10	3.28×10 <sup>-05</sup>	5.18×10 <sup>-05</sup>	0.63	5.74×10 <sup>-05</sup>	1.23×10 <sup>-04</sup>	0.47	1.75	2.84	0.62
R13	6.66×10 <sup>-05</sup>	8.32×10 <sup>-05</sup>	0.80	5.98×10 <sup>-05</sup>	1.16×10 <sup>-04</sup>	0.51	0.90	1.55	0.58
G16	3.39×10 <sup>-05</sup>	3.29×10 <sup>-05</sup>	1.03	1.32×10 <sup>-04</sup>	1.32×10 <sup>-04</sup>	1.00	3.89	5.73	0.68
AVG	<b>0.86±0.18</b>			<b>0.49±0.22</b>			<b>0.47±0.15</b>		

(b) cpCSOO

LOC.	High Energy Hadrons equivalent			Thermal Neutrons equivalent			R-factor		
	measured [cm <sup>-2</sup> /POT]	simulated [cm <sup>-2</sup> /POT]	measured/ simulated	measured [cm <sup>-2</sup> /POT]	simulated [cm <sup>-2</sup> /POT]	measured/ simulated	measured	simulated	measured/ simulated
R1	3.40E-06	7.00E-06	0.49	2.25E-05	6.93E-05	0.32	6.61	14.21	0.47
R4	9.42E-06	1.34E-05	0.71	2.46E-05	8.96E-05	0.27	2.61	8.67	0.30
R5	7.88E-06	1.24E-05	0.64	3.15E-05	9.38E-05	0.34	3.99	9.80	0.41
R7	7.73E-06	1.10E-05	0.70	3.45E-05	1.01E-04	0.34	4.47	12.00	0.37
R9	5.43E-06	9.65E-06	0.56	4.16E-05	1.03E-04	0.41	7.66	14.20	0.54
R10	5.25E-06	1.14E-05	0.46	4.01E-05	1.06E-04	0.38	7.65	12.31	0.62
G16	7.73E-06	8.80E-06	0.88	6.66E-05	9.33E-05	0.71	8.62	14.16	0.61
AVG	<b>0.63±0.15</b>			<b>0.40±0.15</b>			<b>0.47±0.12</b>		

(c) cpCSSO

LOC.	High Energy Hadrons equivalent			Thermal Neutrons equivalent			R-factor		
	measured [cm <sup>-2</sup> /POT]	simulated [cm <sup>-2</sup> /POT]	measured/ simulated	measured [cm <sup>-2</sup> /POT]	simulated [cm <sup>-2</sup> /POT]	measured/ simulated	measured	simulated	measured/ simulated
R1	1.29E-06	2.84E-06	0.45	2.36E-05	6.04E-05	0.39	18	31.26	0.58
R4	4.06E-06	6.19E-06	0.66	2.24E-05	8.28E-05	0.27	6	18.29	0.33
R7	4.54E-06	6.42E-06	0.71	3.16E-05	9.58E-05	0.33	7	21.27	0.33
R10	3.54E-06	9.13E-06	0.39	3.45E-05	1.02E-04	0.34	10	15.41	0.65
G16	3.77E-06	4.32E-06	0.87	5.31E-05	8.90E-05	0.60	14	29.47	0.48
AVG	<b>0.62±0.20</b>			<b>0.38±0.13</b>			<b>0.47±0.14</b>		

(d) cpCSSC

LOC.	High Energy Hadrons equivalent			Thermal Neutrons equivalent			R-factor		
	measured [cm <sup>-2</sup> /POT]	simulated [cm <sup>-2</sup> /POT]	measured/ simulated	measured [cm <sup>-2</sup> /POT]	simulated [cm <sup>-2</sup> /POT]	measured/ simulated	measured	simulated	measured/ simulated
R1	9.04E-07	1.98E-06	0.46	2.44E-05	6.59E-05	0.37	26.99	49.31	0.55
R4	3.27E-06	4.81E-06	0.68	2.76E-05	9.09E-05	0.30	8.42	26.83	0.31
R5	3.03E-06	5.11E-06	0.59	3.21E-05	9.28E-05	0.35	10.57	26.08	0.41
R7	4.48E-06	5.91E-06	0.76	3.31E-05	9.63E-05	0.34	7.4	23.72	0.31
R9	3.64E-06	6.44E-06	0.57	4.03E-05	9.97E-05	0.40	11.06	22.25	0.50
R10	3.93E-06	9.03E-06	0.44	3.69E-05	1.02E-04	0.36	9.41	15.59	0.60
G16	3.11E-06	3.39E-06	0.92	5.27E-05	9.13E-05	0.58	16.97	39.36	0.43
AVG	<b>0.63±0.17</b>			<b>0.39±0.09</b>			<b>0.44±0.11</b>		

Table 5.5: Comparison of RadMON data with FLUKA results for the aluminium target. Note that RadMONs have not been experimentally deployed at all possible test locations; nevertheless, FLUKA allows for estimating the desired set of R2E quantities. The last row presents the average data/FLUKA ratio values and their standard deviation.

(a) alOOOO									
LOC.	High Energy Hadrons equivalent			Thermal Neutrons equivalent			R-factor		
	measured [cm <sup>-2</sup> /POT]	simulated [cm <sup>-2</sup> /POT]	measured/ simulated	measured [cm <sup>-2</sup> /POT]	simulated [cm <sup>-2</sup> /POT]	measured/ simulated	measured	simulated	measured/ simulated
R1	7.19E-06	1.03E-05	<b>0.70</b>	1.15E-05	2.75E-05	<b>0.42</b>	1.6	3.93	<b>0.41</b>
R4	2.00E-05	1.93E-05	<b>1.04</b>	1.08E-05	3.21E-05	<b>0.34</b>	0.54	2.07	<b>0.26</b>
R5	1.73E-05	1.82E-05	<b>0.95</b>	1.43E-05	3.28E-05	<b>0.44</b>	0.83	2.22	<b>0.37</b>
R7	2.22E-05	2.10E-05	<b>1.06</b>	1.39E-05	3.40E-05	<b>0.41</b>	0.63	1.94	<b>0.33</b>
R9	1.74E-05	2.15E-05	<b>0.81</b>	2.00E-05	3.44E-05	<b>0.58</b>	1.15	1.89	<b>0.61</b>
R10	1.86E-05	2.75E-05	<b>0.68</b>	2.08E-05	3.45E-05	<b>0.60</b>	1.12	1.44	<b>0.78</b>
G16	1.55E-05	1.24E-05	<b>1.26</b>	4.73E-05	3.37E-05	<b>1.40</b>	3.06	3.57	<b>0.86</b>
AVG	<b>0.96±0.21</b>			<b>0.60±0.37</b>			<b>0.52±0.23</b>		

(b) alCSOO									
LOC.	High Energy Hadrons equivalent			Thermal Neutrons equivalent			R-factor		
	measured [cm <sup>-2</sup> /POT]	simulated [cm <sup>-2</sup> /POT]	measured/ simulated	measured [cm <sup>-2</sup> /POT]	simulated [cm <sup>-2</sup> /POT]	measured/ simulated	measured	simulated	measured/ simulated
R1	1.41E-06	2.83E-06	<b>0.50</b>	7.59E-06	2.12E-05	<b>0.36</b>	5.38	10.89	<b>0.49</b>
R4	5.21E-06	6.97E-06	<b>0.75</b>	9.33E-06	2.95E-05	<b>0.32</b>	1.79	5.59	<b>0.32</b>
R5	5.05E-06	7.11E-06	<b>0.71</b>	1.19E-05	3.09E-05	<b>0.39</b>	2.35	5.69	<b>0.41</b>
R7	5.78E-06	7.14E-06	<b>0.81</b>	1.32E-05	3.32E-05	<b>0.40</b>	2.29	6.07	<b>0.38</b>
R9	4.68E-06	6.81E-06	<b>0.69</b>	1.69E-05	3.48E-05	<b>0.49</b>	3.61	6.71	<b>0.54</b>
R10	4.97E-06	8.80E-06	<b>0.56</b>	1.63E-05	3.52E-05	<b>0.46</b>	3.29	5.21	<b>0.63</b>
G16	4.71E-06	4.58E-06	<b>1.03</b>	2.62E-05	3.13E-05	<b>0.84</b>	5.55	9.36	<b>0.59</b>
AVG	<b>0.72±0.17</b>			<b>0.46±0.17</b>			<b>0.48±0.12</b>		

(c) alCSSC									
LOC.	High Energy Hadrons equivalent			Thermal Neutrons equivalent			R-factor		
	measured [cm <sup>-2</sup> /POT]	simulated [cm <sup>-2</sup> /POT]	measured/ simulated	measured [cm <sup>-2</sup> /POT]	simulated [cm <sup>-2</sup> /POT]	measured/ simulated	measured	simulated	measured/ simulated
R1	6.05E-07	1.08E-06	<b>0.56</b>	8.53E-06	2.01E-05	<b>0.42</b>	14.11	27.38	<b>0.52</b>
R4	2.39E-06	3.31E-06	<b>0.72</b>	1.09E-05	3.05E-05	<b>0.36</b>	4.54	12.95	<b>0.35</b>
R5	2.35E-06	3.68E-06	<b>0.64</b>	1.29E-05	3.14E-05	<b>0.41</b>	5.49	12.07	<b>0.45</b>
R7	3.92E-06	4.74E-06	<b>0.83</b>	1.34E-05	3.31E-05	<b>0.41</b>	3.41	9.72	<b>0.35</b>
R9	3.50E-06	5.39E-06	<b>0.65</b>	1.61E-05	3.40E-05	<b>0.47</b>	4.61	8.59	<b>0.54</b>
R10	4.24E-06	7.70E-06	<b>0.55</b>	3.84E-05	3.53E-05	<b>1.09</b>	9.07	6.06	<b>1.50</b>
G16	2.42E-06	2.38E-06	<b>1.02</b>	2.62E-05	3.11E-05	<b>0.84</b>	10.8	18.91	<b>0.57</b>
AVG	<b>0.71±0.17</b>			<b>0.57±0.28</b>			<b>0.61±0.40</b>		

The results of the benchmarking between RadMON measurements and simulations are presented in Table 5.3 for the copper target, Table 5.5 for the aluminium target and Table 5.7 for the aluminium with holes target. One consistent feature is that for HEHeq the agreement is satisfactory, with an average (over all configurations) measured/simulated ratio of  $0.78 \pm 0.16$  (i.e. overestimation by 20%), whereas for thermal-energy neutrons this decreases  $0.49 \pm 0.22$  and similarly for the R-factor to  $0.47 \pm 0.15$  (i.e. overestimation by a factor of 2).

Table 5.7: Comparison of RadMON data vs FLUKA results for the aluminium with holes target. Note that RadMONs have not been experimentally deployed at all possible test locations; nevertheless, FLUKA allows for estimating the desired set of R2E quantities. The last row presents the average data/FLUKA ratio values and their standard deviation.

(a) alhOOOO

LOC.	High Energy Hadrons equivalent			Thermal Neutrons equivalent			R-factor		
	measured [cm <sup>-2</sup> /POT]	simulated [cm <sup>-2</sup> /POT]	measured/ simulated	measured [cm <sup>-2</sup> /POT]	simulated [cm <sup>-2</sup> /POT]	measured/ simulated	measured	simulated	measured/ simulated
R1	2.52E-06	5.79E-06	0.44	5.56E-06	1.67E-05	0.33	2.2	4.28	0.51
R4	7.19E-06	1.09E-05	0.66	4.08E-06	1.88E-05	0.22	0.57	2.15	0.27
R7	8.44E-06	1.21E-05	0.70	5.16E-06	2.08E-05	0.25	0.61	2.07	0.29
R10	6.65E-06	1.63E-05	0.41	7.12E-06	2.11E-05	0.34	1.07	1.49	0.72
G16	5.79E-06	7.08E-06	0.82	1.87E-05	2.00E-05	0.94	3.24	3.70	0.87
AVG	$0.60 \pm 0.18$			$0.41 \pm 0.30$			$0.53 \pm 0.26$		

(b) alhCSOO

LOC.	High Energy Hadrons equivalent			Thermal Neutrons equivalent			R-factor		
	measured [cm <sup>-2</sup> /POT]	simulated [cm <sup>-2</sup> /POT]	measured/ simulated	measured [cm <sup>-2</sup> /POT]	simulated [cm <sup>-2</sup> /POT]	measured/ simulated	measured	simulated	measured/ simulated
R1	5.22E-07	1.64E-06	0.32	3.76E-06	1.31E-05	0.29	7.2	11.67	0.62
R4	2.13E-06	4.16E-06	0.51	3.60E-06	1.76E-05	0.20	1.7	5.61	0.30
R7	2.56E-06	4.42E-06	0.58	5.09E-06	2.01E-05	0.25	2	5.99	0.33
R10	1.70E-06	5.61E-06	0.30	5.68E-06	2.16E-05	0.26	3.3	4.98	0.66
G16	1.93E-06	2.77E-06	0.70	1.44E-05	1.87E-05	0.77	7.5	9.25	0.81
AVG	$0.48 \pm 0.17$			$0.36 \pm 0.23$			$0.55 \pm 0.22$		

(c) alhCSSC

LOC.	High Energy Hadrons equivalent			Thermal Neutrons equivalent			R-factor		
	measured [cm <sup>-2</sup> /POT]	simulated [cm <sup>-2</sup> /POT]	measured/ simulated	measured [cm <sup>-2</sup> /POT]	simulated [cm <sup>-2</sup> /POT]	measured/ simulated	measured	simulated	measured/ simulated
R1	2.75E-07	6.87E-07	0.40	3.19E-06	1.29E-05	0.25	14.11	28.66	0.49
R4	9.59E-07	2.07E-06	0.46	4.23E-06	1.94E-05	0.22	4.42	13.33	0.33
R5	1.13E-06	2.36E-06	0.48	4.95E-06	1.97E-05	0.25	4.38	11.85	0.37
R7	1.72E-06	3.06E-06	0.56	5.22E-06	2.16E-05	0.24	3.03	9.78	0.31
R9	1.50E-06	3.54E-06	0.42	6.32E-06	2.18E-05	0.29	4.22	8.30	0.51
R10	1.88E-06	4.91E-06	0.38	6.31E-06	2.28E-05	0.28	3.36	6.07	0.55
G16	1.10E-06	1.52E-06	0.73	1.03E-05	1.92E-05	0.54	9.36	18.39	0.51
AVG	$0.49 \pm 0.12$			$0.29 \pm 0.11$			$0.44 \pm 0.10$		

This could potentially lead to a conservative estimation of the possible single event effects (SEE) induced in the electronics, for detectors calibrated at CHARM. For example, a detector is tested in CHARM and one uses the overestimated FLUKA HEHeq fluence to calculate (via Equation 3.1) the cross-section for the induced SEE in the detectors, leading to a smaller value compared to the experimental one. Then, when operating the detector in the accelerator environment, it will experimentally yield more SEEs compared to the FLUKA predictions.

These results exhibit a satisfactory level of agreement within a factor of 2, common in R2E related

studies. Considering these results, a systematic error of 50% is subsequently considered in the LHC scenario for the RadMON fluence benchmark.

#### 5.4.2.2 TID results with two-step simulation approach

Since the RadMON detectors are not explicitly modelled, the TID (as energy deposition per unit mass) was evaluated in air in the 20x20x20 cm<sup>3</sup> volume. However, such a procedure has several limitations. In a radiation field consisting only of photons, this approximation can be satisfactory as for 1.25-MeV photons (roughly the location of the photon intensity peak for the CHARM radiation field), the mass attenuation coefficients are almost identical in air and in SiO<sub>2</sub> [104]. However, at the high energy mixed-field of CHARM, this assumption fails as the presence of other particles involves different interaction mechanisms, which ultimately yield an under/overestimation of the absorbed dose. The most notable example is the <sup>14</sup>N(n,p)<sup>14</sup>C reaction of thermal neutrons leading to an overestimation of the deposited dose in air [105]: the resulting 590 keV proton will deposit its energy through ionization processes [106].

One solution would be to set a high neutron energy cutoff at 1 MeV to suppress most of the <sup>14</sup>N(n,p)<sup>14</sup>C reaction, as previously performed in Ref. [64]. However, an alternative second step simulation has been studied in Ref. [107], where the particle fluences obtained from initial simulation are used as the new source/beam that will hit an explicit model of the detectors, in this case the RadMON RADFET (see section 4.2.2 for a description of the RadMON detectors). The beam is modelled as a wide uniform beam as large as the irradiated detector, assuming a mono-directional radiation source. Considering that most of the radiation comes from the CHARM target, this is a reasonable approximation. The second step uses the suggested simulation settings of Ref. [107], namely: (i) a RADFET oxide with 400 nm thickness, (ii) PRECISIO default settings in FLUKA, (iii) particle transport thresholds set at 1 keV, and(iv) the input spectra are cutoff at 100 keV (for all particles, except neutrons).

Both the results of the direct simulation and of the second step, together with the measured value and their ratios are presented for each available rack location in Tables 5.9 (copper target), 5.11 (aluminium target), and 5.13 (aluminium with holes target). Their averaged agreement levels are given for convenience in Table 5.15, with a global average agreement level of  $0.82 \pm 0.23$  for the TID deposition in AIR (i.e. 18% overestimation) and  $1.01 \pm 0.36$  for the second step approach.

The study carried out in Ref. [107] considered only the R1 location for the cpOOOO configuration only, as it was meant to be an exploratory study to find the most suitable simulation parameters. Taking advantage of this, these results extend the a wider range of configurations and locations in order to study the usefulness of the second step approach. The 20% improvement indicated in Ref. [107] in the simulated dose is supported by our results, in particular for the shielded configurations (see Table 5.17), where the radiation field consists of more neutrons that contribute to the <sup>14</sup>N(n,p)<sup>14</sup>C reaction.

Such a simulation procedure could be employed at the LHC as well for specific locations where the particle spectra consists predominantly of neutrons and where statistics are sufficiently good.

Table 5.9: Comparison of RadMON (RADFET) TID data with FLUKA results for the copper target, considering both the standard CHARM simulation and the second step approach.

(a) cpOOOO

LOC.	TID					
	Measured [Gy/POT]	Simulated [Gy/POT]	Measured/ Simulated	Simulated 2nd step [Gy/POT]	Measured/ Simulated 2nd step	Simulated 2nd step/ 1st step
G0	2.50E-15	2.97E-15	<b>0.84</b>	3.08E-15	<b>0.81</b>	<b>1.04</b>
R1	1.20E-14	1.40E-14	<b>0.86</b>	1.21E-14	<b>0.99</b>	<b>0.86</b>
R4	2.17E-14	2.58E-14	<b>0.84</b>	2.85E-14	<b>0.76</b>	<b>1.11</b>
R5	1.70E-14	2.10E-14	<b>0.81</b>	2.00E-14	<b>0.85</b>	<b>0.95</b>
R7	1.95E-14	2.51E-14	<b>0.78</b>	3.14E-14	<b>0.62</b>	<b>1.25</b>
R9	1.70E-14	2.34E-14	<b>0.73</b>	2.32E-14	<b>0.73</b>	<b>1.00</b>
R10	2.41E-14	2.61E-14	<b>0.92</b>	2.49E-14	<b>0.97</b>	<b>0.95</b>
R13	3.00E-14	3.86E-14	<b>0.78</b>	3.88E-14	<b>0.77</b>	<b>1.00</b>
M14	1.49E-13	7.86E-14	<b>1.90</b>	8.86E-14	<b>1.68</b>	<b>1.13</b>
G16	1.41E-14	1.70E-14	<b>0.83</b>	1.53E-14	<b>0.92</b>	<b>0.90</b>
AVG	<b>0.93±0.34</b>			<b>0.91±0.29</b>		<b>1.02±0.12</b>

(b) cpCSOO

LOC.	TID					
	Measured [Gy/POT]	Simulated [Gy/POT]	Measured/ Simulated	Simulated 2nd step [Gy/POT]	Measured/ Simulated 2nd step	Simulated 2nd step/ 1st step
R1	1.29E-15	1.58E-15	<b>0.82</b>	9.77E-16	<b>1.32</b>	<b>0.62</b>
R4	2.84E-15	2.86E-15	<b>0.99</b>	1.86E-15	<b>1.52</b>	<b>0.65</b>
R5	3.31E-15	2.69E-15	<b>1.23</b>	2.01E-15	<b>1.64</b>	<b>0.75</b>
R7	3.46E-15	3.08E-15	<b>1.12</b>	2.25E-15	<b>1.54</b>	<b>0.73</b>
R9	3.56E-15	3.55E-15	<b>1.00</b>	2.44E-15	<b>1.46</b>	<b>0.69</b>
R10	4.97E-15	4.27E-15	<b>1.17</b>	3.67E-15	<b>1.36</b>	<b>0.86</b>
G16	2.84E-15	2.57E-15	<b>1.10</b>	1.40E-15	<b>2.03</b>	<b>0.54</b>
AVG	<b>1.06±0.14</b>			<b>1.55±0.24</b>		<b>0.69±0.10</b>

(c) cpCSSO

LOC.	TID					
	Measured [Gy/POT]	Simulated [Gy/POT]	Measured/ Simulated	Simulated 2nd step [Gy/POT]	Measured/ Simulated 2nd step	Simulated 2nd step/ 1st step
R1	7.28E-16	1.05E-15	<b>0.69</b>	6.79E-16	<b>1.07</b>	<b>0.65</b>
R4	1.48E-15	1.87E-15	<b>0.79</b>	1.17E-15	<b>1.27</b>	<b>0.63</b>
R7	2.16E-15	2.57E-15	<b>0.84</b>	1.87E-15	<b>1.16</b>	<b>0.73</b>
R10	2.44E-15	4.34E-15	<b>0.56</b>	3.39E-15	<b>0.72</b>	<b>0.78</b>
G16	1.77E-15	2.26E-15	<b>0.78</b>	1.25E-15	<b>1.41</b>	<b>0.55</b>
AVG	<b>0.73±0.11</b>			<b>1.13±0.26</b>		<b>0.67±0.09</b>

(d) cpCSSC

LOC.	TID					
	Measured [Gy/POT]	Simulated [Gy/POT]	Measured/ Simulated	Simulated 2nd step [Gy/POT]	Measured/ Simulated 2nd step	Simulated 2nd step/ 1st step
R1	7.38E-16	9.67E-16	<b>0.76</b>	5.49E-16	<b>1.34</b>	<b>0.57</b>
R4	1.60E-15	1.80E-15	<b>0.89</b>	1.10E-15	<b>1.45</b>	<b>0.61</b>
R5	1.88E-15	1.90E-15	<b>0.99</b>	1.30E-15	<b>1.44</b>	<b>0.69</b>
R7	2.21E-15	2.65E-15	<b>0.84</b>	2.00E-15	<b>1.10</b>	<b>0.76</b>
R9	2.41E-15	3.04E-15	<b>0.79</b>	2.09E-15	<b>1.15</b>	<b>0.69</b>
R10	3.56E-15	4.47E-15	<b>0.80</b>	3.51E-15	<b>1.01</b>	<b>0.78</b>
G16	1.76E-15	2.00E-15	<b>0.88</b>	1.26E-15	<b>1.40</b>	<b>0.63</b>
AVG	<b>0.85±0.08</b>			<b>1.27±0.18</b>		<b>0.68±0.08</b>

Table 5.11: Comparison of RadMON (RADFET) TID data with FLUKA results for the aluminium target, considering both the standard CHARM simulation and the second step approach.

(a) alOOOO

LOC.	TID					
	Measured [Gy/POT]	Simulated [Gy/POT]	Measured/ Simulated	Simulated 2nd step [Gy/POT]	Measured/ Simulated 2nd step	Simulated 2nd step/ 1st step
R1	4.43E-15	5.10E-15	<b>0.87</b>	4.34E-15	<b>1.02</b>	<b>0.85</b>
R4	1.01E-14	1.16E-14	<b>0.87</b>	1.32E-14	<b>0.76</b>	<b>1.14</b>
R5	9.63E-15	1.12E-14	<b>0.86</b>	1.18E-14	<b>0.82</b>	<b>1.05</b>
R7	1.12E-14	1.39E-14	<b>0.80</b>	1.41E-14	<b>0.80</b>	<b>1.01</b>
R9	1.13E-14	1.43E-14	<b>0.79</b>	1.40E-14	<b>0.81</b>	<b>0.97</b>
R10	1.25E-14	1.76E-14	<b>0.71</b>	1.77E-14	<b>0.71</b>	<b>1.01</b>
G16	6.83E-15	9.08E-15	<b>0.75</b>	8.44E-15	<b>0.81</b>	<b>0.93</b>
AVG	<b>0.81±0.06</b>			<b>0.82±0.10</b>		<b>0.99±0.09</b>

(b) alCSOO

LOC.	TID					
	Measured [Gy/POT]	Simulated [Gy/POT]	Measured/ Simulated	Simulated 2nd step [Gy/POT]	Measured/ Simulated 2nd step	Simulated 2nd step/ 1st step
R1	4.48E-16	5.75E-16	<b>0.78</b>	3.98E-16	<b>1.13</b>	<b>0.69</b>
R4	1.60E-15	1.68E-15	<b>0.96</b>	1.58E-15	<b>1.01</b>	<b>0.94</b>
R5	1.93E-15	1.95E-15	<b>0.99</b>	1.53E-15	<b>1.26</b>	<b>0.78</b>
R7	2.37E-15	2.44E-15	<b>0.97</b>	2.08E-15	<b>1.14</b>	<b>0.85</b>
R9	2.62E-15	2.81E-15	<b>0.93</b>	2.53E-15	<b>1.04</b>	<b>0.90</b>
R10	4.35E-15	4.41E-15	<b>0.99</b>	3.53E-15	<b>1.23</b>	<b>0.80</b>
G16	1.57E-15	1.94E-15	<b>0.81</b>	1.35E-15	<b>1.16</b>	<b>0.70</b>
AVG	<b>0.92±0.09</b>			<b>1.14±0.09</b>		<b>0.81±0.10</b>

(c) alCSSC

LOC.	TID					
	Measured [Gy/POT]	Simulated [Gy/POT]	Measured/ Simulated	Simulated 2nd step [Gy/POT]	Measured/ Simulated 2nd step	Simulated 2nd step/ 1st step
R1	3.66E-16	4.18E-16	<b>0.88</b>	2.33E-16	<b>1.57</b>	<b>0.56</b>
R4	1.31E-15	1.27E-15	<b>1.03</b>	1.14E-15	<b>1.15</b>	<b>0.90</b>
R5	1.72E-15	1.53E-15	<b>1.13</b>	1.18E-15	<b>1.46</b>	<b>0.77</b>
R7	2.23E-15	2.16E-15	<b>1.03</b>	1.71E-15	<b>1.30</b>	<b>0.79</b>
R9	2.52E-15	2.74E-15	<b>0.92</b>	2.21E-15	<b>1.14</b>	<b>0.81</b>
R10	4.19E-15	4.22E-15	<b>0.99</b>	3.67E-15	<b>1.14</b>	<b>0.87</b>
G16	1.39E-15	1.75E-15	<b>0.79</b>	1.79E-15	<b>0.78</b>	<b>1.02</b>
AVG	<b>0.97±0.11</b>			<b>1.22±0.26</b>		<b>0.82±0.14</b>

Table 5.13: Comparison of RadMON (RADFET) TID data with FLUKA results for the aluminium with holes target, considering both the standard CHARM simulation and the second step approach.

(a) alhOOOO

LOC.	TID					
	Measured [Gy/POT]	Simulated [Gy/POT]	Measured/ Simulated	Simulated 2nd step [Gy/POT]	Measured/ Simulated 2nd step	Simulated 2nd step/ 1st step
R1	1.51E-15	3.12E-15	<b>0.48</b>	3.02E-15	<b>0.50</b>	<b>0.97</b>
R4	3.46E-15	6.73E-15	<b>0.51</b>	6.54E-15	<b>0.53</b>	<b>0.97</b>
R7	3.71E-15	7.85E-15	<b>0.47</b>	7.67E-15	<b>0.48</b>	<b>0.98</b>
R10	4.79E-15	9.84E-15	<b>0.49</b>	9.69E-15	<b>0.49</b>	<b>0.98</b>
G16	2.34E-15	5.26E-15	<b>0.45</b>	5.19E-15	<b>0.45</b>	<b>0.99</b>
AVG			<b>0.48±0.02</b>		<b>0.49±0.03</b>	<b>0.98±0.01</b>

(b) alhCSOO

LOC.	TID					
	Measured [Gy/POT]	Simulated [Gy/POT]	Measured/ Simulated	Simulated 2nd step [Gy/POT]	Measured/ Simulated 2nd step	Simulated 2nd step/ 1st step
R1	1.63E-16	3.49E-16	<b>0.47</b>	2.39E-16	6.83E-01	<b>0.68</b>
R7	9.48E-16	1.43E-15	<b>0.66</b>	1.16E-15	8.15E-01	<b>0.81</b>
R10	1.01E-15	2.67E-15	<b>0.38</b>	0	4.23E-01	<b>0.90</b>
G16	5.25E-16	1.09E-15	<b>0.48</b>	9.83E-16	5.34E-01	<b>0.90</b>
AVG			<b>0.50±0.12</b>		0.61±0.17	<b>0.82±0.10</b>

(c) alhCSSC

LOC.	TID					
	Measured [Gy/POT]	Simulated [Gy/POT]	Measured/ Simulated	Simulated 2nd step [Gy/POT]	Measured/ Simulated 2nd step	Simulated 2nd step/ 1st step
R1	1.72E-16	2.81E-16	<b>0.61</b>	5.41E-16	<b>0.32</b>	<b>1.92</b>
R4	5.21E-16	8.35E-16	<b>0.62</b>	6.18E-16	<b>0.84</b>	<b>0.74</b>
R5	6.86E-16	1.02E-15	<b>0.67</b>	8.22E-16	<b>0.83</b>	<b>0.81</b>
R7	8.48E-16	1.25E-15	<b>0.68</b>	1.08E-15	<b>0.79</b>	<b>0.86</b>
R9	9.58E-16	1.59E-15	<b>0.60</b>	1.39E-15	<b>0.69</b>	<b>0.87</b>
R10	1.63E-15	2.70E-15	<b>0.60</b>	2.48E-15	<b>0.66</b>	<b>0.92</b>
G16	5.57E-16	9.83E-16	<b>0.57</b>	6.94E-16	<b>0.80</b>	<b>0.71</b>
AVG			<b>0.62±0.04</b>		<b>0.70±0.18</b>	<b>0.98±0.42</b>

Table 5.15: Benchmark results for the RadMON TIDs for the AIR cube model (step 1) and for the explicit RadMON model (step 2), for each target. The last row present the averaged values.

(a) Copper target

	RadMON TID					
	Ratio Measured / step 1		Ratio measured / step 2		Ratio step 2 / step 1	
	AVG	STDEV	AVG	STDEV	AVG	STDEV
cpOOOO	0.93	0.34	0.91	0.29	1.02	0.12
cpCSOO	1.06	0.14	1.55	0.24	0.68	0.10
cpCSSO	0.73	0.11	1.13	0.26	0.65	0.09
cpCSSC	0.85	0.08	1.27	0.18	0.67	0.08
AVG (cp)	<b>0.91</b>	<b>0.25</b>	<b>1.19</b>		<b>0.80</b>	<b>0.19</b>

(b) Aluminium target

	RadMON TID					
	Ratio Measured / step 1		Ratio measured / step 2		Ratio step 2 / step 1	
	AVG	STDEV	AVG	STDEV	AVG	STDEV
alOOOO	0.81	0.06	0.82	0.10	0.99	0.09
alCSOO	0.92	0.09	1.14	0.09	0.81	0.10
alCSSC	0.97	0.11	1.22	0.26	0.79	0.14
AVG (al)	<b>0.90</b>	<b>0.11</b>	<b>1.06</b>		<b>0.87</b>	<b>0.14</b>

(c) Aluminium with holes target

	RadMON TID					
	Ratio Measured / step 1		Ratio measured / step 2		Ratio step 2 / step 1	
	AVG	STDEV	AVG	STDEV	AVG	STDEV
alhOOOO	0.48	0.02	0.49	0.03	0.98	0.01
alhCSOO	0.50	0.12	0.61	0.17	0.81	0.10
alhCSSC	0.62	0.04	0.70	0.18	0.88	0.42
AVG (alh)	<b>0.55</b>	<b>0.10</b>	<b>0.62</b>		<b>0.94</b>	<b>0.28</b>

Table 5.17: Average ratio of the explicit RadMON model (step 2) over the AIR cube (step 1) benchmark results

	AVG	STDEV
OOOO	0.99	0.02
CSOO	0.77	0.07
CSSC	0.78	0.11

### 5.4.3 Optical fibre benchmark

The optical fibre dosimeter presents the advantage of measuring spatially distributed TID profiles, compared to the point-like measurements of BLMs or RadMONs. The results of TID measurements with an optical fibre dosimeter have been previously presented in Ref. [64], together with a first

comparison with FLUKA predictions, and a similar benchmark with the updated simulation is included in this work.

The optical fibre (OF) dosimeter is too small (only  $125\ \mu\text{m}$  in diameter) to include an exact replica in the FLUKA geometry in a CPU-efficient manner, hence it is modelled as a 1 cm thick cylinder made of  $\text{SiO}_2$ . This represents a significant update with respect to the FLUKA simulation used in [64], where a scoring of dose in air was used.

The path of the OF sensor (schematically shown in Figure 5.1) follows the walls of the facility, with regions close to the target where peaks are observed in Figure 5.5 at 60 m and 75 m. The OF segments between (40-45), (65, 70) and (80, 100) m are mounted behind the shieldings, hence the pronounced decrease in the estimated levels for the fully shielded configuration.

The shape of the 1D profile is very well reproduced (see Figure 5.5), and the ratio of measured and simulated dose is generally well within the 50% margin, with local fluctuations in both directions. The average (weighted on TID) of the measured over simulation ratio is  $0.93 \pm 0.24$  for the cpOOOO shielding and  $0.99 \pm 0.32$  for the cpCSSC shielding. Considering these results, a systematic error of 30% is subsequently considered in the LHC scenario for the optical fibre sensor TID benchmark.

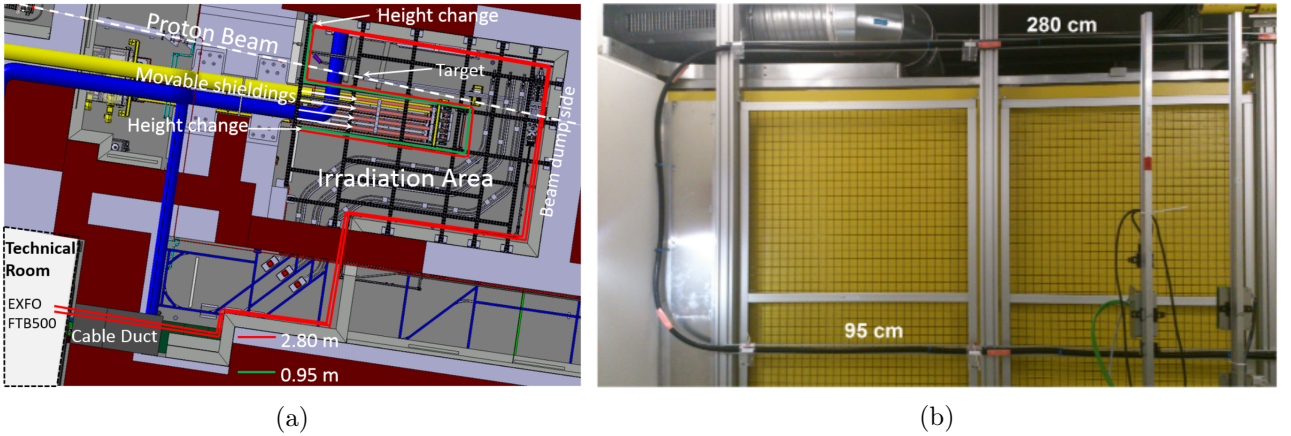


Figure 5.4: CHARM optical fibre path as (a) modelled in FLUKA, and (b) deployed at the facility. [108]

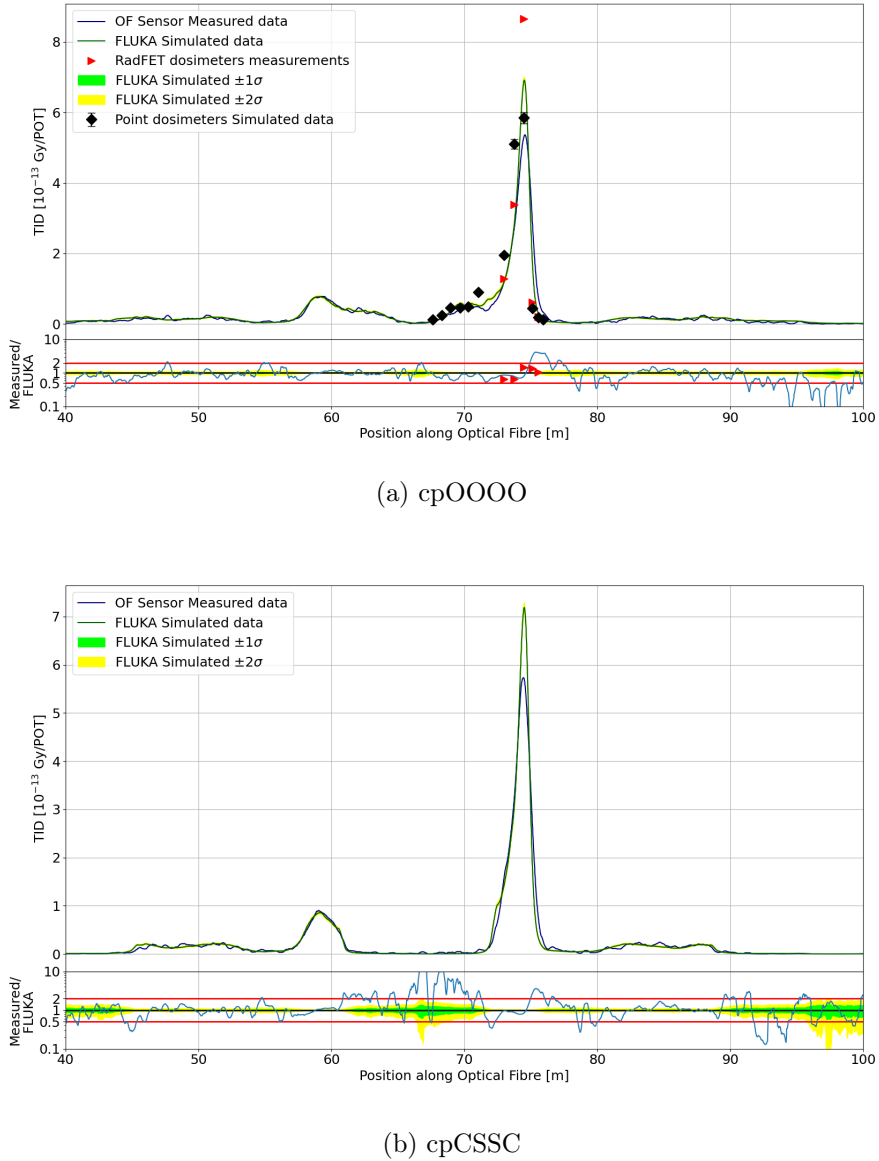


Figure 5.5: Comparison of optical fibre data with FLUKA for two shielding configurations: cpOOOO (top) and cpCSSC (bot). The green and yellow band are the  $\pm 1\sigma$  and  $\pm 2\sigma$  simulated statistical uncertainty intervals, respectively, centered on the FLUKA simulation result. For the cpOOOO configuration, pointwise measurements were available from deployed RADFET dosimeters, for which the TID values have been simulated in a  $20 \times 20 \times 20$  cm<sup>3</sup> cube made out of AIR. The lower pad shows the ratio between the measurements and simulation, and the red lines display the factor 2 discrepancy range.



# Chapter 6

## LHC Environment Simulations and Comparison with Data

The ultimate scope of this thesis is to perform a systematic benchmark between the simulated and the measured data for the radiation monitors useful for radiation to electronics (R2E) studies at the large hadron collider (LHC). For this purpose, the radiation levels are simulated using the FLUKA Monte Carlo code (version 4.1.1, CERN distributed) and compared against measurements performed with: (i) the beam loss monitoring (BLMs) system [50], (ii) the radiation monitor (RadMON) system [56], and (iii) 180 m of distributed optical fiber sensor (OF) [64].

Experimentally, the measured data is stored continuously over the entire Run 2 period of data taking and quantifies radiation levels for different operational parameters of the LHC machine. However, it is neither feasible from a computational point of view to simulate all possible LHC configurations (i.e. all combinations of beam optics, collimation parameters, etc., as further described in Section 6.2), nor very relevant since some of them correspond to low radiation levels or correspond just to singular test runs. Therefore, several selection criteria are considered to identify time periods from the entire Run 2 that allow for a direct comparison between measured and simulated data.

To validate the combined use of FLUKA simulations and radiation monitor measurements, an application benchmark study has been performed for the long straight section (LSS) and dispersion suppressor (DS) at the high luminosity interaction points (IP1 - ATLAS and IP5 - CMS). Moreover, the simulation has been extended into the ARC of IP1 to test several hypotheses. The objective of this study was to compare the total ionizing dose (TID) and the high energy hadron (HEHeq) fluences measured by the several radiation monitors within the scope of R2E (see Chapter 3) with the values predicted by the FLUKA simulations for the Run 2 LHC operation.

### 6.1 Radiation source - luminosity driven interaction points

The accelerator on the right side of the ATLAS (IP1, see Figure 6.1) and CMS (IP5) that are used in this thesis have been constructed with the procedure prescribed in Section 4.3.4, as a common effort within the SYS-STI-BMI section.

As previously described in Section 2.6 and indicated by Figures 6.2 and 6.3, the main source of radiation in the interaction points (IPs) are the debris from the beam collisions. In practical terms for the FLUKA simulations, this implies that the source term are proton-proton collisions located at  $z = 0$  m that will then propagate in the tunnel. Therefore, the further away from the interaction point, the lower the radiation levels and the statistics of the FLUKA simulations decreases, and thus, the simulation error increases (see Figure 6.3). As a rule of thumb for Monte Carlo simulations, statistical simulation errors of less than 20% should be used for reliable results.

In order to compare the FLUKA results with the measured data, the nominal simulation output has to be normalized per unit  $\text{fb}^{-1}$ , which is achieved by multiplying the simulation output with the inelastic proton-proton cross section of  $\sigma = 80 \text{ mb}$  at 6.5 TeV beam energy (see Equation 2.1). In addition, the total ionizing dose (TID) yielded in FLUKA is in units of  $\text{GeV/g}$ , which is converted to Gy via a conversion factor of  $1.60217 \cdot 10^{-7} \text{ Gy}/(\text{GeV/g})$ .

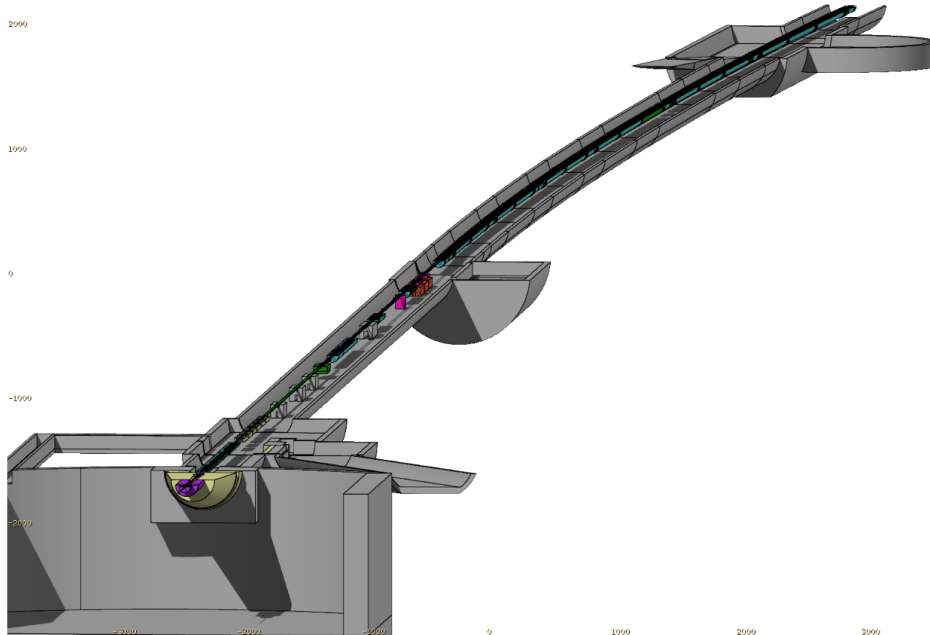


Figure 6.1: FLUKA geometry of the right side of IP1.

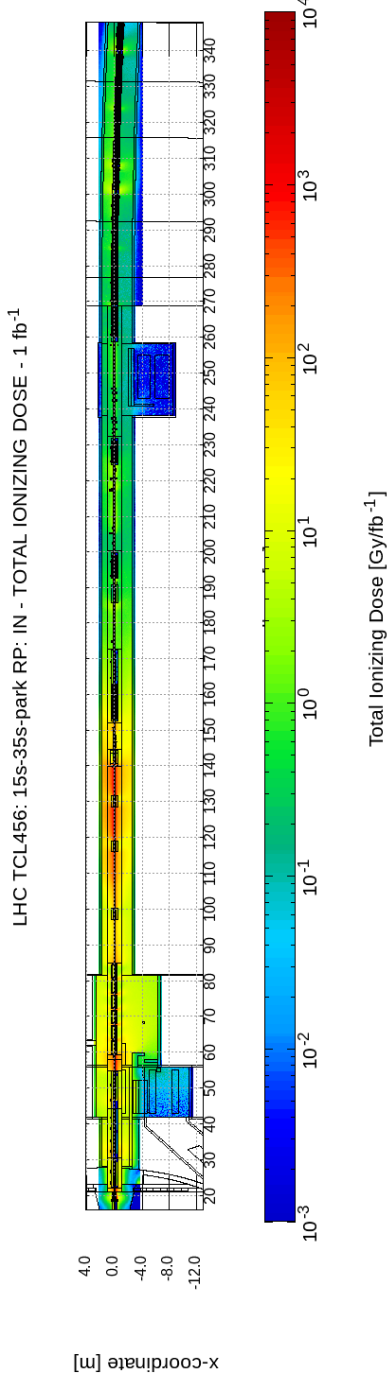


Figure 6.2: Simulated TID deposition in AIR in the right side of LHC for the configuration mostly used in 2018. Similar plots are available for the other FLUKA simulated values: HEHeq, THN and R-factor.

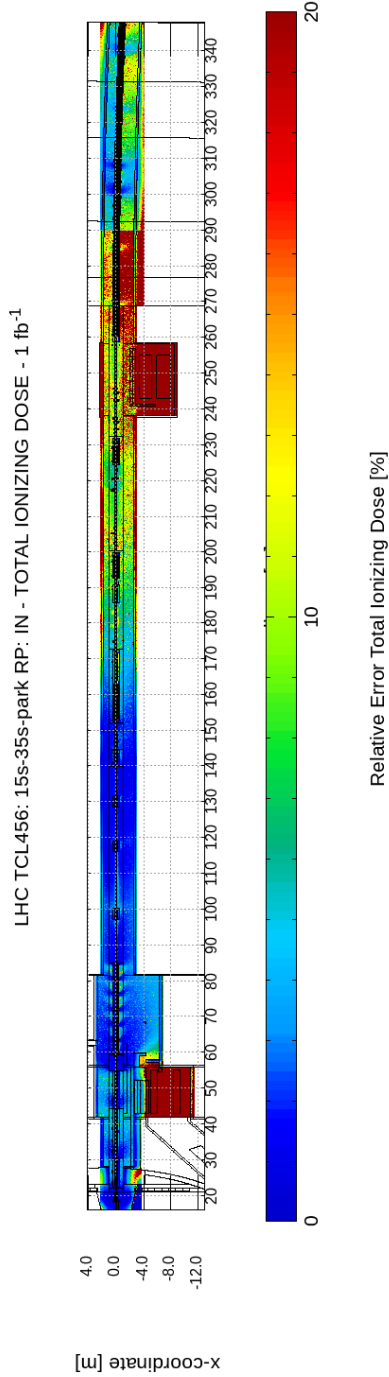


Figure 6.3: Simulated TID deposition in AIR and its associated simulation errors in the right side of LHC for the configuration mostly used in 2018. From 290 m, the second step simulation results are used, hence the lower errors from this point.

### 6.1.1 Second step simulations

To handle the computational issue of having sufficient statistics even at hundreds of meters away from the source term at  $z = 0$ , the simulation for the dispersion suppressor (DS) region (after 269 m) is done via 2 steps:

- a simulation is run with high particle thresholds of 1 TeV to speed up the computation, as it is considered that only these high energetic debris are capable to reach the DS region after 269 m<sup>1</sup>. Their properties (position, velocity, particle type, etc.) are saved ("dumped") into a file whenever they interact with a beamline element such an aperture restriction or the beam pipe,
- and used as input for a second step simulation that begins at 269 m. A consequence of this procedure is that the region between 269 and 290 m is undersimulated (see Figure 6.4, due to the lack of forward scattering from the debris before 269 m.).

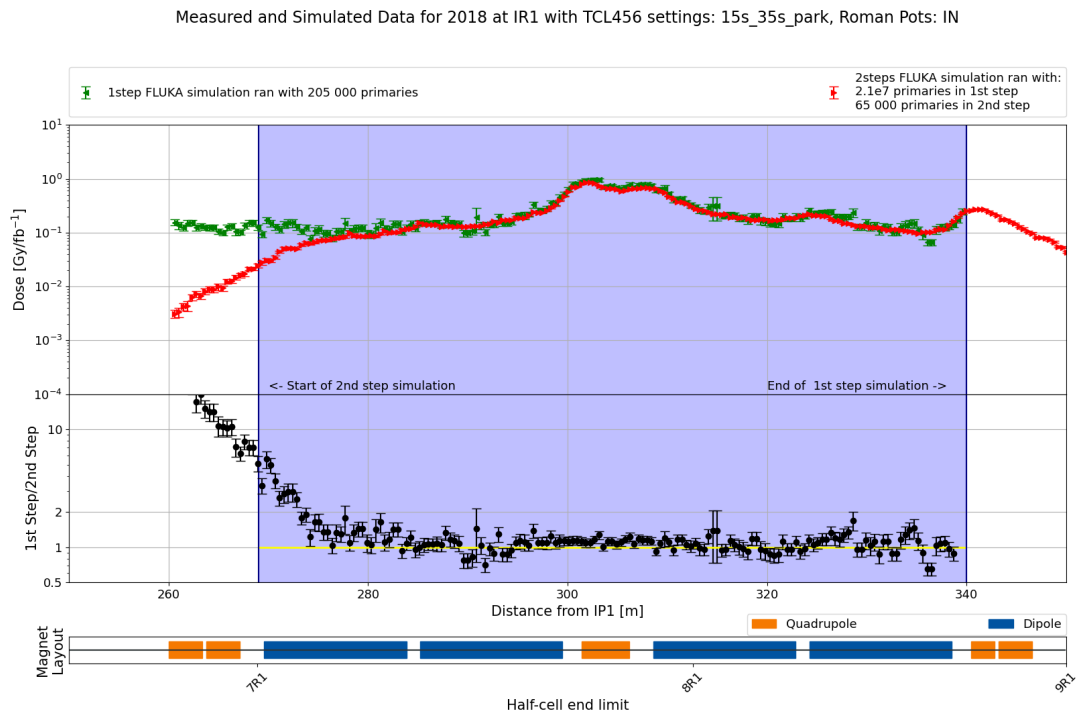


Figure 6.4: Comparison between the 1<sup>st</sup> step and the 2<sup>nd</sup> step simulations. The second step simulated values before 269 m are due to backscattering. The values provided here are scored in 20x20x50 cm<sup>3</sup> (X x Y x Z) in AIR next to the inner side of the tunnel wall.

<sup>1</sup>The value of 1 TeV at 269 m has been found by trial-error to yield suitable results, but if one desires to cut the particles ahead or downstream of the 269 m cut used here, the cutoff thresholds should be changed as well

### 6.1.2 Particle distributions

Electronic components and other equipment that are installed in the tunnel and adjacent areas are exposed to a mixed radiation field which varies considerably both in intensity and composition depending on the exact location with respect to the loss points. This long term exposure induces both cumulative and stochastic effects as previously described, leading to temporary or even permanent failures. The long-term effects are related to total ionizing dose (mainly electromagnetic components) and displacement damage (generally associated to 1-MeV neutron equivalent fluence in silicon SiO<sub>2</sub>), while the frequency of single event effects (SEE) depends, in first approximation, on the high energy hadron equivalent (HEHeq) fluence.

The radiation composition cannot be discriminated using the current radiation monitors employed at the LHC, with the exception of the RadMON V6 that can measure thermal energy neutrons. In order to have access to this information, the FLUKA simulation has been used to score the most relevant particles species in several locations along the LHC: in the long straight section (LSS) (see Figures 6.6), in the dispersion suppressor (DS) (see Figures 6.7) and in the shielded alcoves (Figures 6.9). The spectra are scored in 20x20x20 cm<sup>3</sup> in AIR, at floor level, for the regions in the tunnel, and in larger volumes (due to poor statistics) in the shielded alcoves, in locations where RadMONs are also placed.

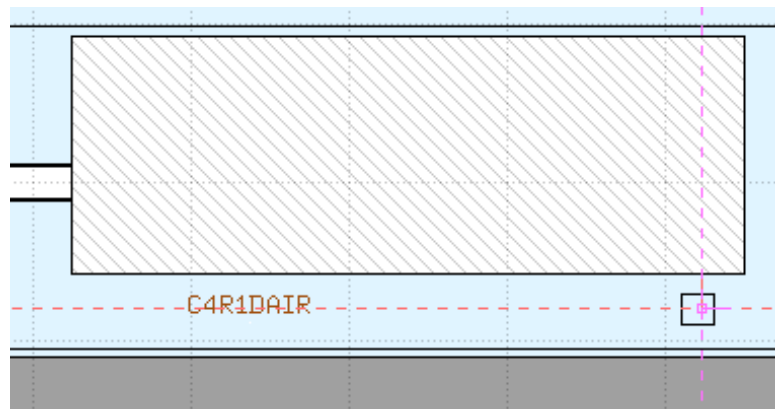


Figure 6.5: Side view of the LHC tunnel, showcasing a typical RadMON location in the tunnel, at floor level (the gray area is in the lower part). The large shaded box is the target collimator long 4 (TCL4), which generates a radiation shower when its aperture is closed, hence the placement of the RadMON in its vicinity.

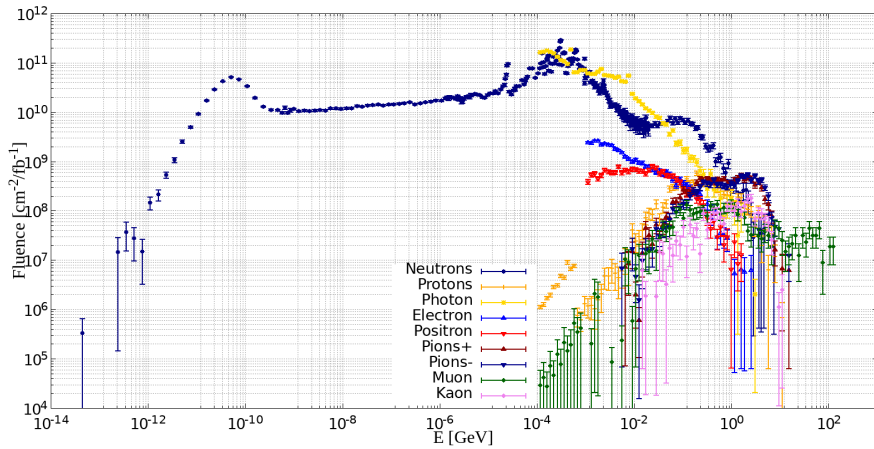
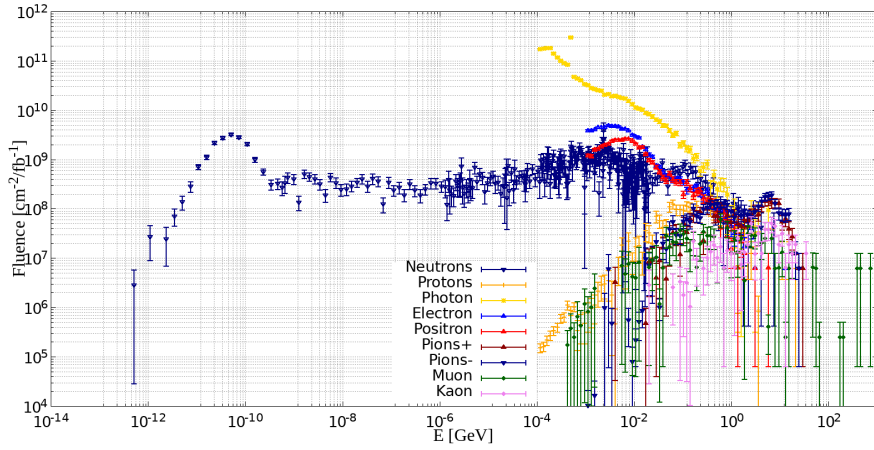
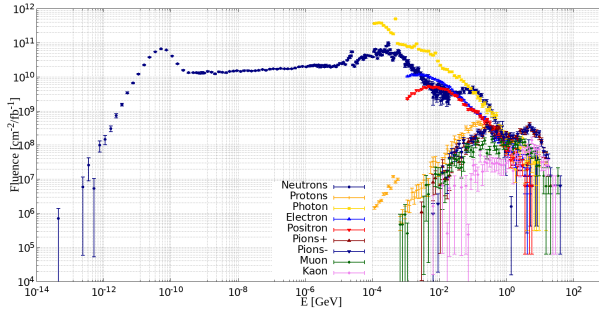

 (a) Inner triplet region ( $z = 50$  m).

 (b) Tunnel location, unshielded ( $z = 100$  m).

 (c) TAN collimator region, absorbing neutral particles ( $z = 144$  m).

Figure 6.6: Simulated particle spectra at floor level below the beam at several locations along the LHC tunnel for the 2018 LHC configuration.

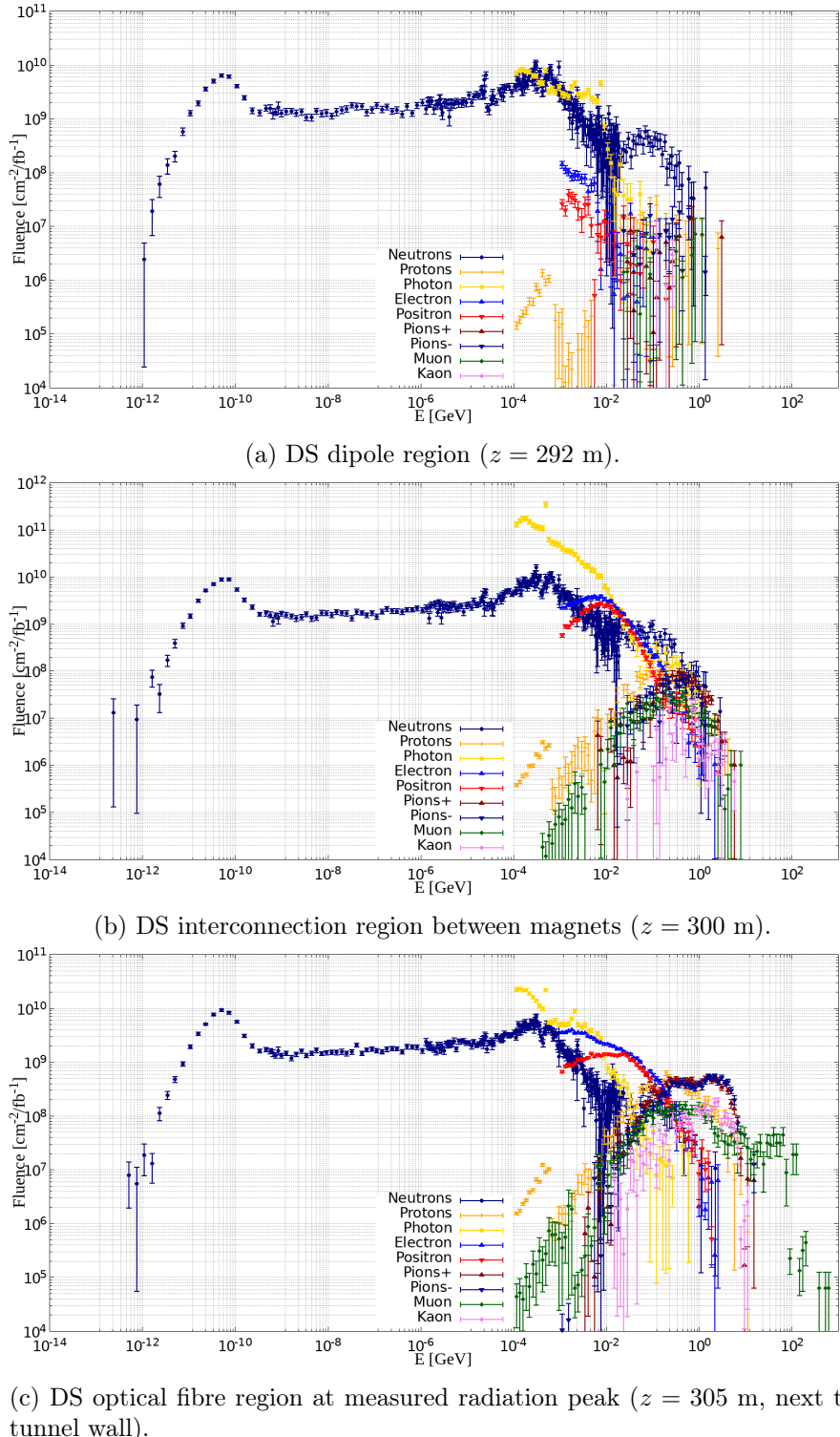
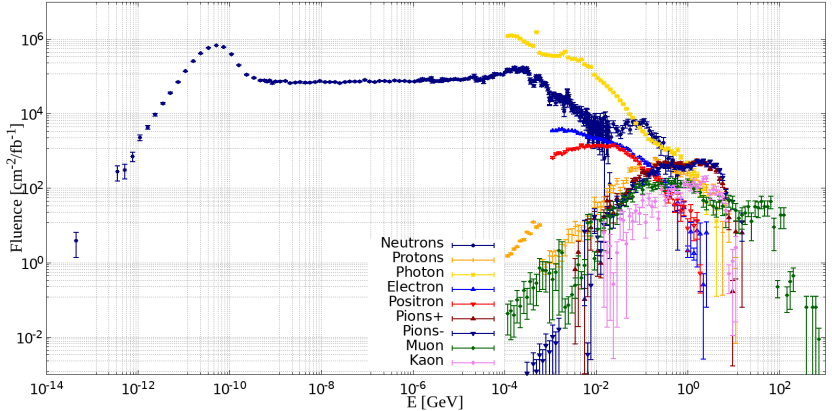
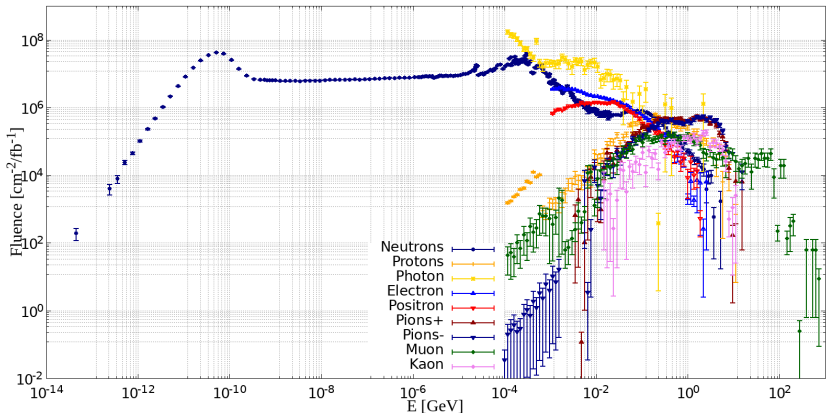


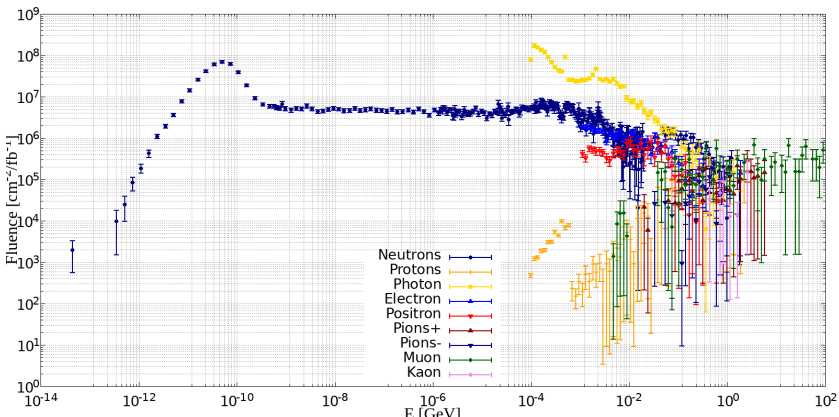
Figure 6.7: Simulated particle spectra at floor level below the beam at several locations along the LHC tunnel for the 2018 LHC configuration.



(a) UJ16 shielded alcove.



(a) UJ17 shielded alcove.



(b) RR17 shielded alcove.

Figure 6.9: Simulated particle spectra in the shielded alcoves next to the LHC tunnel for the 2018 LHC configuration.

## 6.2 Selected time periods of LHC operation

There are several parameters that describe the operation of the LHC in the proximity of the interaction points (IP), which impact the radiation levels in the subsequent regions of the tunnel. They have been described in section 2.3, and we recall those considered in this thesis here:

- crossing angle: the angle between the colliding beams.
- $\beta^*$ : the transversal size of the beam at the IP.
- target collimator long (TCL) settings: aperture size (and usage) of the collimators protecting the beam elements, e.g. the cold magnets in half-cell 8 and 9.
- roman pots (RP) settings: devices used to measure the total cross section of two particle beams in a collider, which can either be used (IN) or not (OUT)<sup>2</sup>

The starting point of the present analysis is to select periods of the LHC operation with stable operational parameters, such that their radiation level data can be compared to a corresponding FLUKA simulation that represents as accurately as possible the LHC configuration under examination. Indeed, the simulations employed in this study are able to (statically) replicate only one such configuration at a time, i.e. neither the alternating use of the TCLs or the RP, nor the (anti-)levelling cannot be reproduced. This leads to the need to identify time periods with constant LHC settings within single fills, given in Table 6.1, quantifying how much integrated luminosity (i.e. how many collision data, representing the source of radiation) have been delivered for each condition.

The first selection criterion is for the radiation monitor data to correspond to the STABLE BEAMS beam mode, as this one corresponds to the delivery of luminosity. Subsequently, within this single fill, some parameters (such as the collimator settings or the roman pots usage) alternate between two predefined values, while others are changed quasi-continuously, as the LHC performance has been improved. Starting from 2017, crossing angle anti-levelling has been successfully employed to increase the instantaneous luminosity towards the end of the fill. Moreover, the baseline  $\beta^*$  setting was reduced in the technical stop 2 (TS2) of 2017 from 40 cm to 30 cm, while in 2018 anti-levelling within the fills was used to increase the instantaneous luminosity.

---

<sup>2</sup>The Roman Pots can also have various apperture size, but to what concerns this thesis, their impact can be considered as binary (IN/OUT)

Table 6.1: Delivered luminosity for constant LHC operational settings. The crossing angle cells containing the asterisk \* indicate that quasi-continuous anti-levelling took place within the fill, and the value provided here is the average considered for the simulation. Similar anti-levelling occurred for the the  $\beta^*$ , but as it happened incrementally, it could be further subdivided. The bold values in the "Extracted luminosity per setting" column correspond to the configurations that have been simulated.

IR	year	Crossing angle [ $\mu$ rad]	$\beta^*$ [cm]	TCL5 [ $\sigma$ (state)]	TCL6 [ $\sigma$ (state)]	Roman Pots	Extracted luminosity per setting (approx.)
IR1	2015		80	15 (closed)	open	OUT	0.17
				35 (open)	20 (closed)	IN	0.00
	2016	-185	40	15 (closed)	open	OUT	<b>33.03</b>
				35 (open)	20 (closed)	IN	0.04
	2017	150*	40	15 (closed)	open	OUT	1.00
				35 (open)	20 (closed)	IN	6.10
			30	15 (closed)	open	OUT	0.01
				35 (open)	20 (closed)	IN	<b>7.88</b>
	2018	130*	30	16.4 (closed)	open	OUT	4.10
				38.2 (open)	open	IN	<b>21.12</b>
			27	15.7 (closed)	open	OUT	0.08
				36.6 (open)	open	IN	0.55
			25	15.0 (closed)	open	OUT	0.05
				35.0 (open)	open	IN	0.28
IR5	2015		80	15 (closed)	open	OUT	0.09
				35 (open)	20 (closed)	IN	0.00
	2016		40	15 (closed)	open	OUT	13.95
				35 (open)	20 (closed)	IN	7.12
	2017		40	15 (closed)	open	OUT	4.28
				35 (open)	20 (closed)	IN	19.19
			30	15 (closed)	open	OUT	0.05
				35 (open)	20 (closed)	IN	9.99
	2018		30	16.4 (closed)	open	OUT	1.08
				38.2 (open)	open	IN	<b>28.37</b>
			27	15.7 (closed)	open	OUT	0.00
				36.6 (open)	open	IN	0.42
			25	15.0 (closed)	open	OUT	0.00
				35.0 (open)	open	IN	0.45

### 6.3 Measured data

As already discussed, the tunnel next to the ATLAS (IP1) and CMS (IP5) experiments are considered to have collision debris from the interaction point as the main source of radiation. Scaling the measured values of the BLMs by luminosity as in Figure 6.10 confirms this assumption. Moreover, the comparison of measured TID per unit integrated luminosity for different periods of operation with the same configuration of LHC parameters exhibits a very stable profile. This result allows us to merge different fills corresponding to periods with identical operational conditions, yielding the data set statistics of Table 6.1.

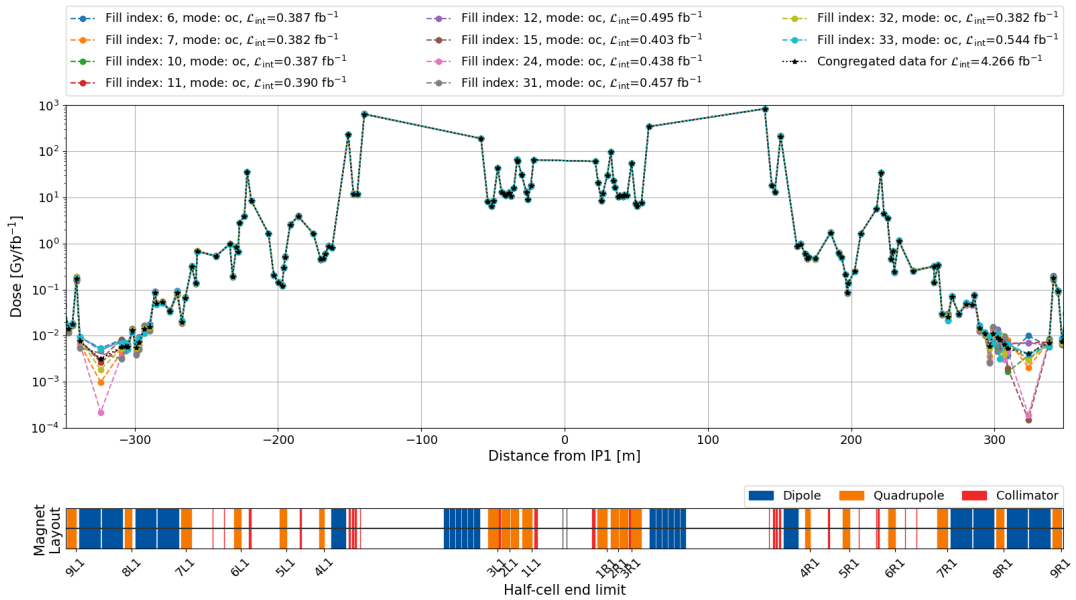


Figure 6.10: A selection of the time-integrated BLM TID profile vs the instance from the collision point in IP1 sharing the same operational settings (2017 configuration, "oc" indicates the TCL configuration with TCL5 open and TCL6 closed), showcasing that luminosity is a suitable scaling factor.

Moreover, the symmetry around the interaction point (IP) allows to reduce the study only to one side of the interaction point, thereby halving the computational time subsequently needed for the simulation. This is the main reason why the FLUKA geometry has been implemented only for the right side of the IP in Figure 6.1.

One immediate question is how much do the aforementioned LHC machine parameters affect the radiation levels on a local level, if not globally. Different local radiation levels due to the change

in collimator settings are shown in Figure 6.11, where the collimator apertures of TCL5 and 6 have been changed. Both TCL5 and TCL6 have a BLM immediately after them that registers a significant difference in the deposited TID between the two different settings. Moreover, the TCL6's apperture change is relevant not for its impact in the region immediately afterwards, but in the region between 270 to 350 m (half-cells 8 and 9), protecting the superconducting bending magnets and the quadrupoles. The impact of the aperture change from 380 m onwards is negligible.

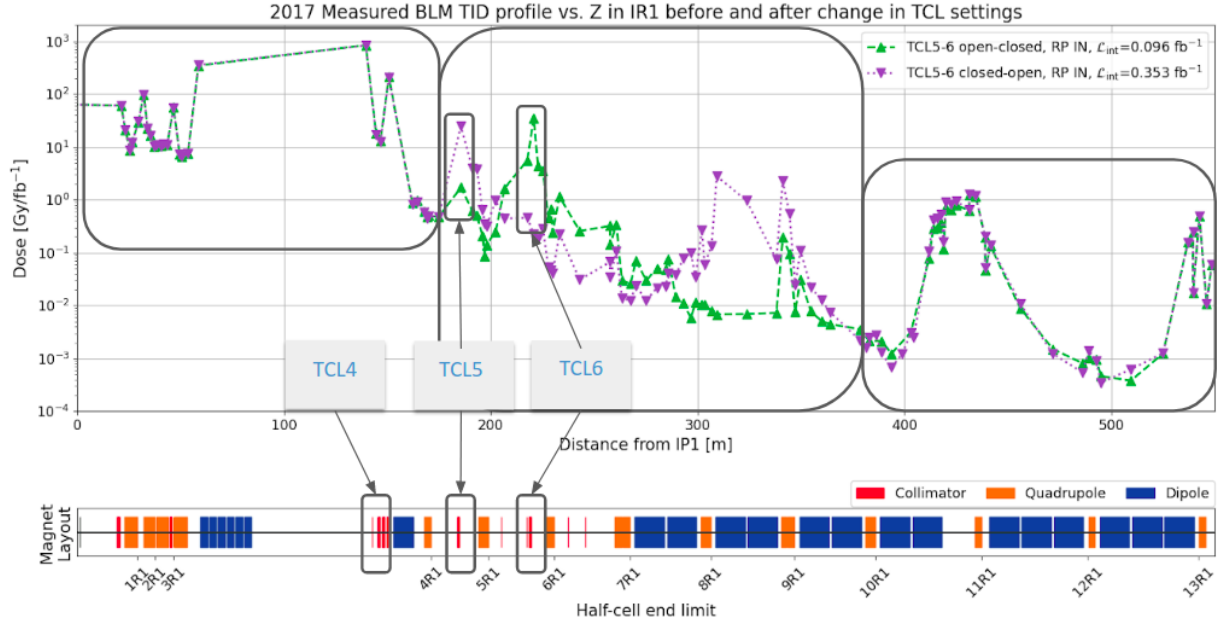


Figure 6.11: Measured BLM TID profile vs distance from the collision point in IP1 for fill number 6724 in 2017 before and after the changes in the collimator and roman pot settings. The positions of the three collimators (TCL4, 5, 6) are highlighted, although only the settings of the latter two have been modified during the run.

In addition, the radiation levels measured by the BLM outside the RR shielded alcove (i.e. on the tunnelside) have a very strong correlation with the TCL settings. Inside the RR, the RadMON measurements exhibit radiation levels that change by roughly a factor of 10 depending on the TCL settings, in the absence of the roman pots. However, when TCL6 is used with open apperture and the roman puts are used (as in most of the 2018 operation), then the change is much more modest, as a factor of 2 only. Especially relevant in terms of operational impact are the radiation levels in the RRs, as they host a large number of power converters that suffer mainly from single event effect (SEE) failures.

The impact of the roman pots cannot be studied independently in the measured data, as they have either been used (or not) depending if TCL6 was open (or not). However, the simulated levels the for the different usage of the TOTEM roman pots are shown in Figure 6.12.

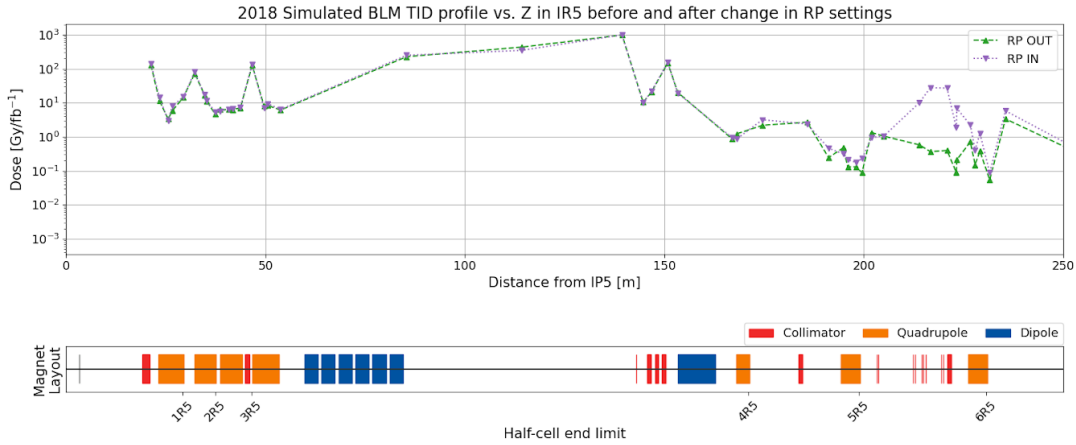


Figure 6.12: FLUKA simulated BLM TID profile vs distance from the collision point in IP5 before and after the changes in the roman pot settings for the 2018 configuration.

## 6.4 Total ionizing dose results

The total ionizing dose (TID) (see Section 3.3.1.1 for a full description) is the energy deposited per unit mass through either electromagnetic or hadronic showers via ionisation in the material, as simulated by FLUKA.

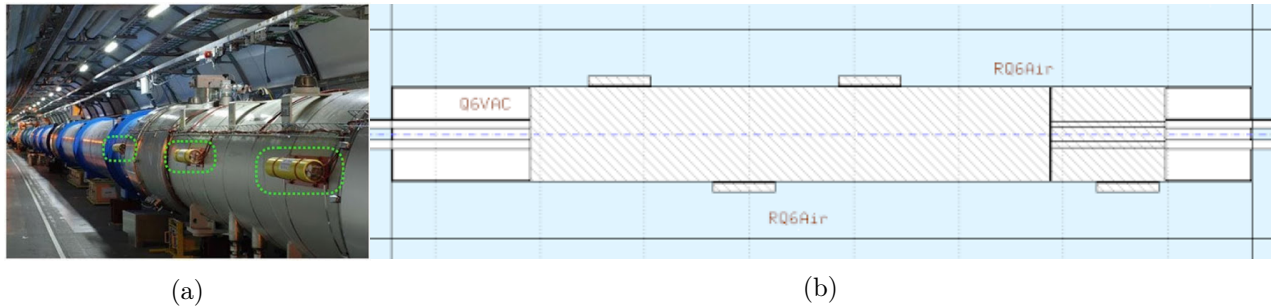


Figure 6.13: Beam loss monitor (BLM), (a) as deployed in the LHC (yellow detectors), and (b) as simulated in the FLUKA geometry around a quadrupole.

### 6.4.1 Beam loss monitor benchmark

Within the large LHC FLUKA geometry, the beam loss monitors (BLMs) are explicitly modelled and the TID is deposited in their active volume (Nitrogen gas) and compared to the measured values.

Previous sporadic studies of this kind for Run 2 [109, 110] have used a similar simulation procedure, but the experimental data consisted of at most one LHC fill (corresponding to at most  $0.65 \text{ fb}^{-1}$ ). Similar studies have been performed for the the BLM benchmark for Run 1 of the LHC, when it was operated at 4 TeV [111, 112].

The experimental errorbars considered in this analysis are derived from the CHARM study (see Section 5.4.1), namely a 30% systematic error.

#### 6.4.1.1 Single step simulation: LSS + DS (half-cells 8+9)

The single step FLUKA simulation usually employed in such studies originally covered only the long straight section (LSS) up to 269 m, but it has been extended for two more half-cells (8 and 9) into the dispersion suppressor (DS) up to 348 m to bridge the subsequent second step (as described in the next paragraph 6.1.1). The LHC configurations that have been chosen from Table 6.1 for simulation studies are shown in Figures 6.14 (2016), 6.15 (2017) and 6.16 (2018) for IP1 and in 6.17 (2018) for IP5. Throughout the thesis, the green and yellow band represent the  $\pm 1\sigma$  and  $\pm 2\sigma$  simulated statistical uncertainty intervals, respectively, centered on the FLUKA simulation result. The middle pad shows the ratio between the measurements and simulation, and the red lines display the factor 20% Monte Carlo threshold considered as good statistics for a reliable result. The lower pad displays the corresponding machine beamline layout. The TID weighted average ratio for each configuration is given in Tables 6.2, together with the standard deviation (STD).

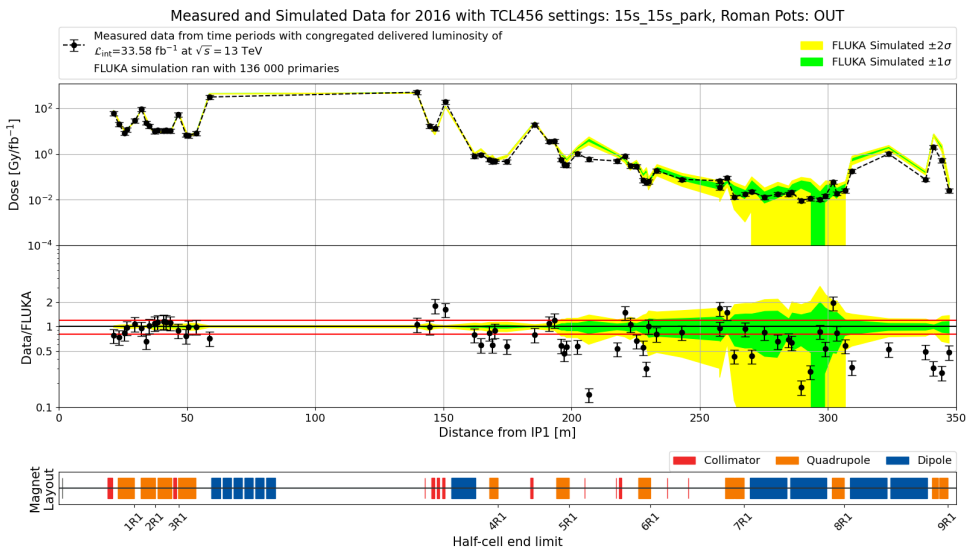


Figure 6.14: Comparison between BLM data and FLUKA predictions for IP1 LSS+DS in 2016 for TCL456: 15s-15s-park RP: OUT.

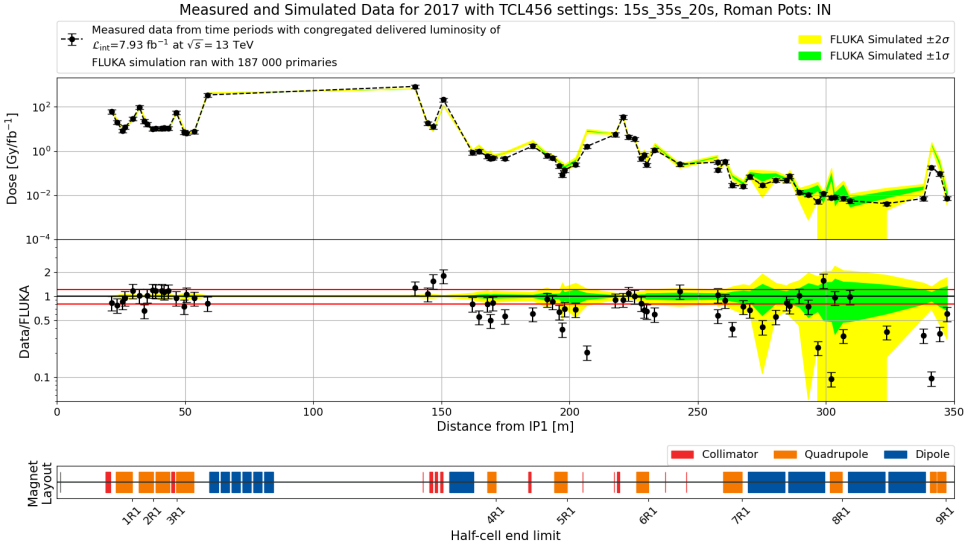


Figure 6.15: Comparison between BLM data and FLUKA predictions for IP1 LSS+DS in 2017 for TCL456: 15s-35s-20s RP: IN.

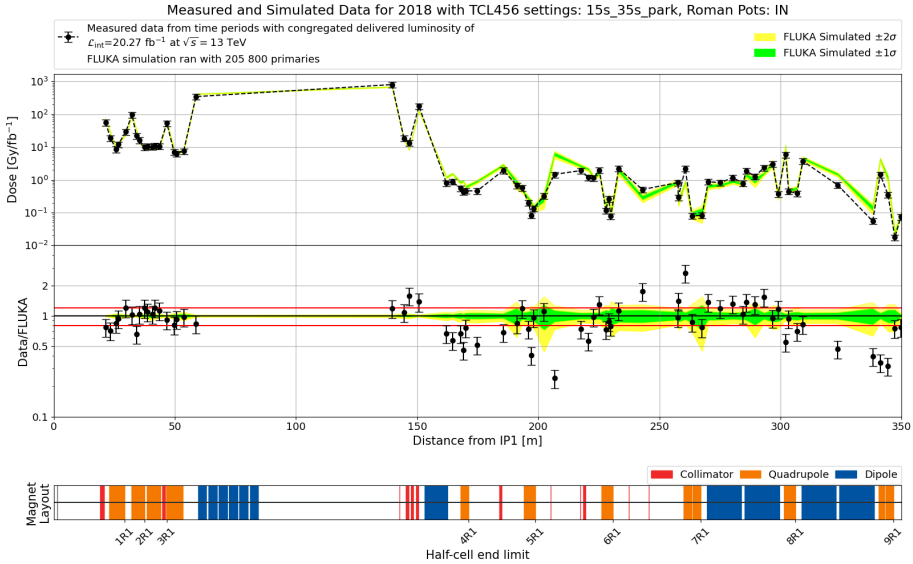


Figure 6.16: Comparison between BLM data and FLUKA predictions for IP1 LSS+DS in 2018 for TCL456: 15s-35s-park RP: IN.

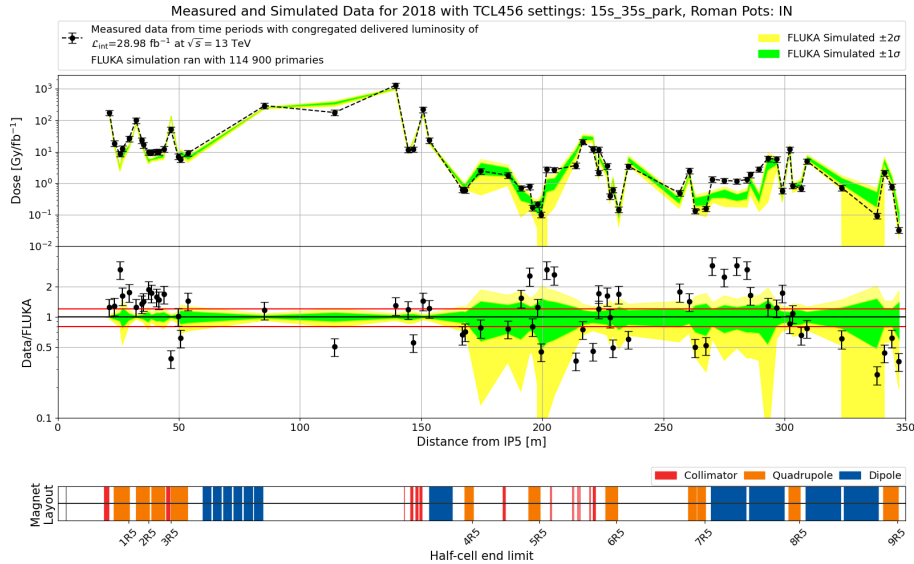


Figure 6.17: Comparison between BLM data and FLUKA predictions for IP5 LSS+DS IN 2018 for TCL456: 15s-35s-park RP: IN.

There are a couple of global trends regardless of the chosen configuration, out of which the most important is the global good agreement within a factor of 2 between data and FLUKA simulations. For the highly irradiated BLMs near the inner triplet IT up to 70 m, there is a very good agreement (i.e. within the errorbars). The largest TID is recorded at the BLM next to the TAN collimator [113], as it absorbs the flux of forward high energy neutral particles (predominantly neutrons) that are produced at the collision points of IP1 and IP5, thereby preventing these particles from quenching the twin aperture superconducting beam separation dipoles (D2) and the outer triplet quadrupoles (Q4, Q5, Q6) and localizing the induced activation to the absorber. Subsequently, this generates plenty of secondary showers and thermalizes neutrons, leading to a high TID area, as it can be seen also from Figure 6.2. In consequence, a local overestimation (e.g. at TCL4) is usually followed by an underestimation (and vice-versa) as it can be seen around 150 m. The further away from the interaction point, the smaller number of particle debris can arrive without being absorbed upstream and the lower the TID; this also leads to poorer simulation statistics, especially for configurations with TCL6 closed (as in 2016 and 2017), which results in lower levels in half-cells 8 and 9.

There are a few strategies to identify the disagreement sources for the most prominent outliers. One such strategy is identifying systematic discrepancies across the several configurations/years. For example, the BLM identified as BLMEI.06R1.B1E10\_XRP.A6R1 located at 206.69 m (visible in all figures as an outlier with very low data/FLUKA ratio) is shifted by 1 m compared to its actual location, placing it into a local peak of a radiation shower in the simulation. In general, such obvious outliers are considered to arise due to inaccurate geometry modelling.

### 6.4.1.2 Two-step simulation approach: DS + ARC

Owing to the aforementioned poor statistics, the two-step simulation procedure (see Section 6.1.1) has been employed from 290 m onwards, which yields results that are virtually identical to those as from the single step in the overlap region, as indicated by Figure 6.4. The two-step simulation approach has been used just for the 2018 configurations of IP1 (Figure 6.18) and IP5 (Figure 6.19). There is a reasonable agreement for higher TID BLMs, such as those in half-cell 11, but the are discrepancies still to be investigated in half-cell 13. The very large simulation errors after 550 m, especially those larger than 20% even after running 260 000 primaries in the second step, indicate that even the two-step simulation procedure is not able to achieve statistical convergence beyond half-cell 13.

Based on the very good scaling with luminosity, it is clear that the collision debris are the main source of radiation in the long straight section (LSS). Moreover, the beam losses in the dispersion suppressor (DS) are also considered to be composed of off-momentum protons with a  $\delta p/p_0$  of 2-20% up to half-cell 9, 1-2% up to half-cell 11 and below 1% in half-cell 13 (up to 550 m from the IP) [114]. In the LHC ARC, the beam-residual gas interaction becomes the main source of radiation (for a detailed analysis of the measured BLM signals in the ARC, please consult Ref. [49]).

This thesis answers as well an old question about LHC operation: at which point is the collision debris no longer dominant? From this study (qualitatively in Figures 6.18 and quantitatively from

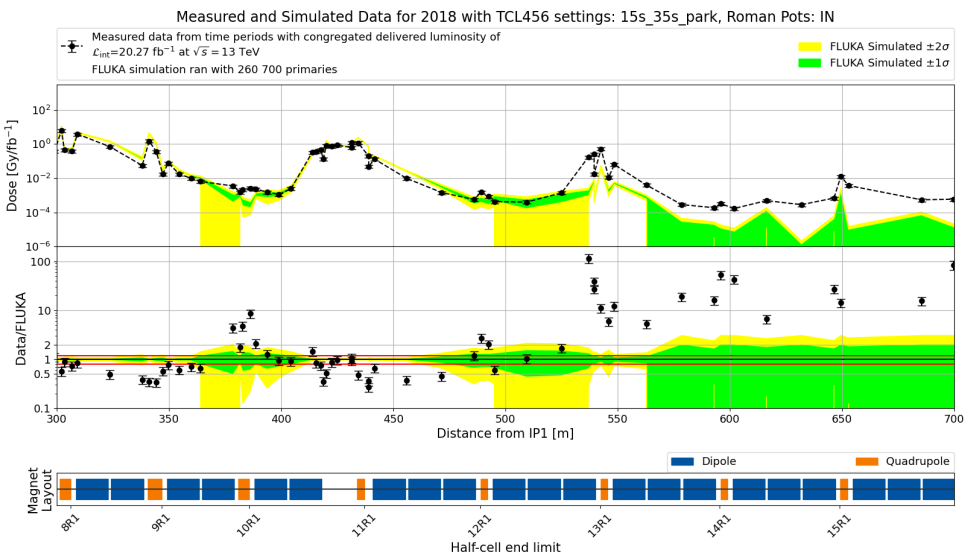


Figure 6.18: Comparison between BLM data and FLUKA predictions for IP1 DS+ARC in 2018 TCL456: 15s-35s-park RP: IN.

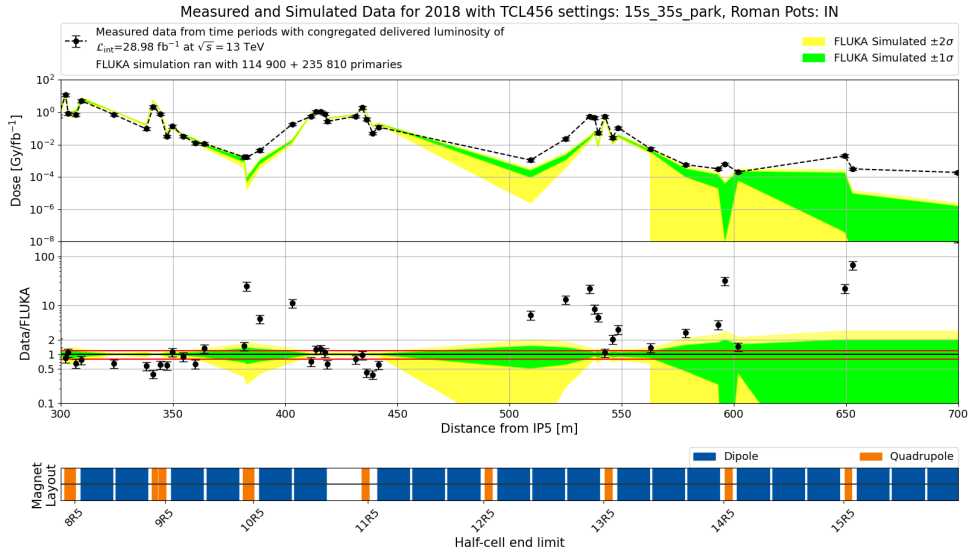


Figure 6.19: Comparison between BLM data and FLUKA predictions for IP5 DS+ARC in 2018 TCL456: 15s-35s-park RP: IN.

the agreement levels of Table 6.2), we infer that the collision debris are no longer the main source of radiation only after 550 m (end of half-cell 13), in the ARC region. Nevertheless, small local radiation peaks could be distinguished even further in BLM data [53], in half-cells 15 and 17, which are considered to be also luminosity-driven.

#### 6.4.1.3 Joint simulations of LSS and DS

The results from the previous two sections can be joint as described in Section 6.1.1: the second step simulation values are used from 290 m onwards. Similar procedure is applied in the next sections to compare data and simulated values of other radiation monitors.

To summarise, the BLM agreement is generally very good, with the global ratio of measured to FLUKA simulated values (see Table 6.2) always within 25% for the areas where the collision debris represent the main source of radiation. Regionally, there are some systematic trends that can be observed. The BLMs in the DS region are oversimulated by a factor of 2 for the configurations with TCL6 operated with closed aperture (2016 and 2017), which could be due to the significantly lower radiation levels leading to poorer simulation statistics as well. The agreement improves when TCL6 is opened (2018), even overshooting within 50% for IP5.

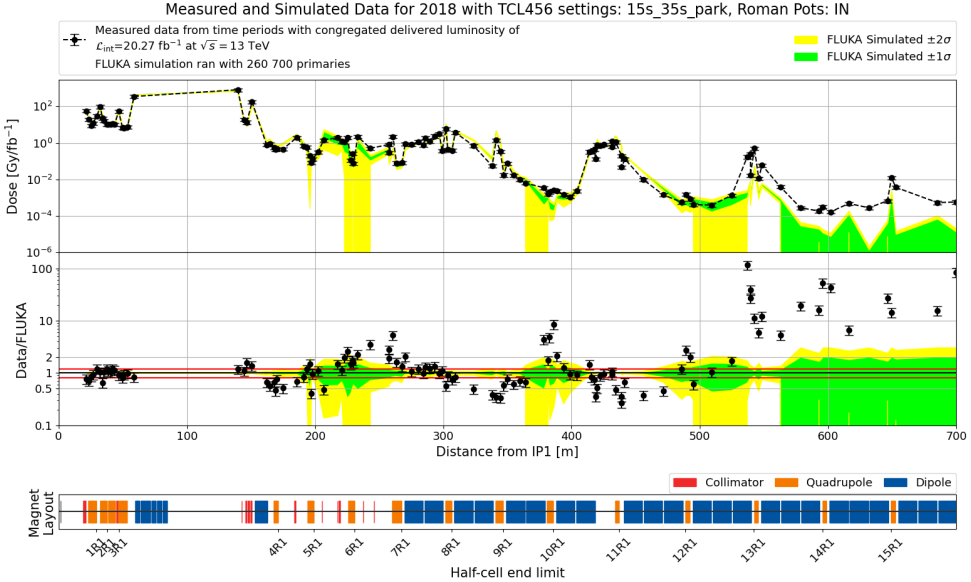


Figure 6.20: Comparison between BLM data and FLUKA predictions for IP1 LSS+DS+ARC 2018  
TCL456: 15s-35s-park RP: IN.

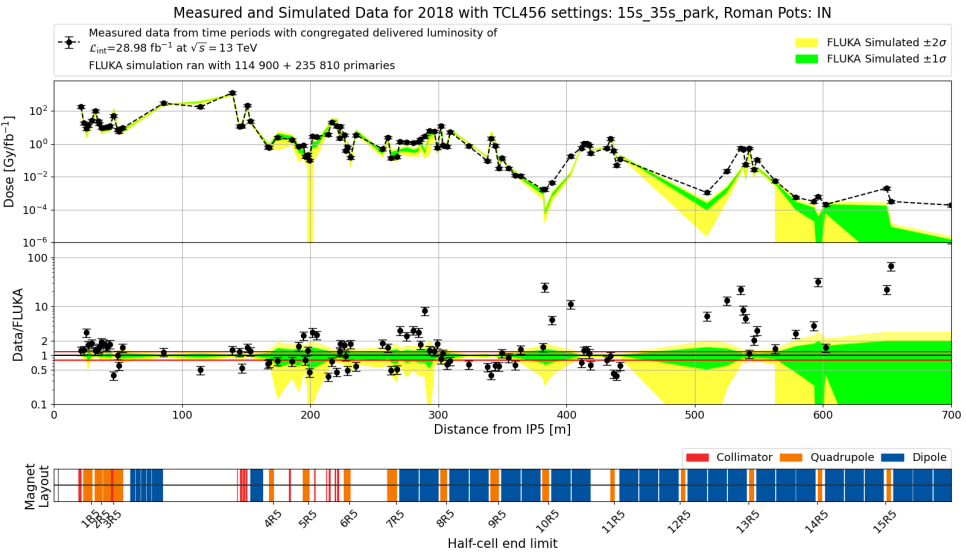


Figure 6.21: Comparison between BLM data and FLUKA predictions for IP5 LSS+DS+ARC 2018  
TCL456: 15s-35s-park RP: IN.

Table 6.2: TID averaged ratio of measured data to FLUKA values for the beam loss monitors (BLM).

(a) IP1 2016.

Region	Distance from IP	Measured data to FLUKA ratio		
		AVG	STD	STD [%]
LSS (Inner Triplet)	0 to 60 m	0.829	0.038	4.613
LSS (after TAN)	140 to 269 m	1.204	0.071	5.889
DS (single step)	269 to 348 m	0.398	0.098	24.707
Global	0 to 348 m	1.022	0.046	4.453

(b) IP1 2017.

Region	Distance from IP	Measured data to FLUKA ratio		
		AVG	STD	STD [%]
LSS (Inner Triplet)	0 to 60 m	0.894	0.040	4.420
LSS (after TAN)	140 to 269 m	1.339	0.056	4.156
DS (single step)	269 to 348 m	0.443	0.095	21.365
Global	0 to 348 m	1.163	0.040	3.469

(c) IP1 2018.

Region	Distance from IP	Measured data to FLUKA ratio		
		AVG	STD	STD [%]
LSS (Inner Triplet)	0 to 60 m	0.896	0.039	4.406
LSS (after TAN)	140 to 269 m	1.231	0.173	14.045
DS (single step)	269 to 348 m	0.909	0.089	9.811
Global	0 to 348 m	1.089	0.092	8.445

(d) IP5 2018.

Region	Distance from IP	Measured data to FLUKA ratio		
		AVG	STD	STD [%]
LSS (Inner Triplet)	0 to 60 m	1.140	0.117	10.248
LSS (after TAN)	140 to 269 m	1.251	0.103	8.225
DS (single step)	269 to 348 m	1.434	0.444	30.965
Global	0 to 348 m	1.213	0.108	8.917

(e) IP1 2018 second step.

Region	Distance from IP	Measured data to FLUKA ratio		
		AVG	STD	STD [%]
DS step 2	290 to 450 m	0.789	0.256	32.476
ARC	450 to 700 m	37.606	28.996	77.104

(f) IP5 2018 second step.

Region	Distance from IP	Measured data to FLUKA ratio		
		AVG	STD	STD [%]
DS step 2	290 to 450 m	1.254	1.496	119.275
ARC	450 to 700 m	9.947	14.594	146.708

### 6.4.2 Optical fibre benchmark

When deployed in the machine tunnels, the optical fibre (OF) sensors operate in a complex mixed-field radiation environment. For this reason, they have been qualified in conditions as close as possible to the ones encountered during operation [64, 65]. The previous CHARM section 5.4.3 described an updated FLUKA approach to estimate the radiation levels and the agreement with measured data, quantifying the expected agreement level to a 30% error margin.

Compared to the online monitoring done in the proton synchrotron booster (PSB) [61], the optical fibre deployed in 2018 in the DS region right of IP1 provides only passive measurements collected during the three technical stops, as it can be seen in Figure 6.24. The TID per unit  $\text{fb}^{-1}$  in the three time periods is consistent with each other and henceforth only the cumulative (annual) value shall be used. Since multiple LHC operational settings have been used throughout 2018 and the optical fibre sensor data does not allow to identify time periods as for the BLMs, the simulated values have to be weighted according to how much integrated luminosity (taken from Table 2.1) each mode corresponded to.

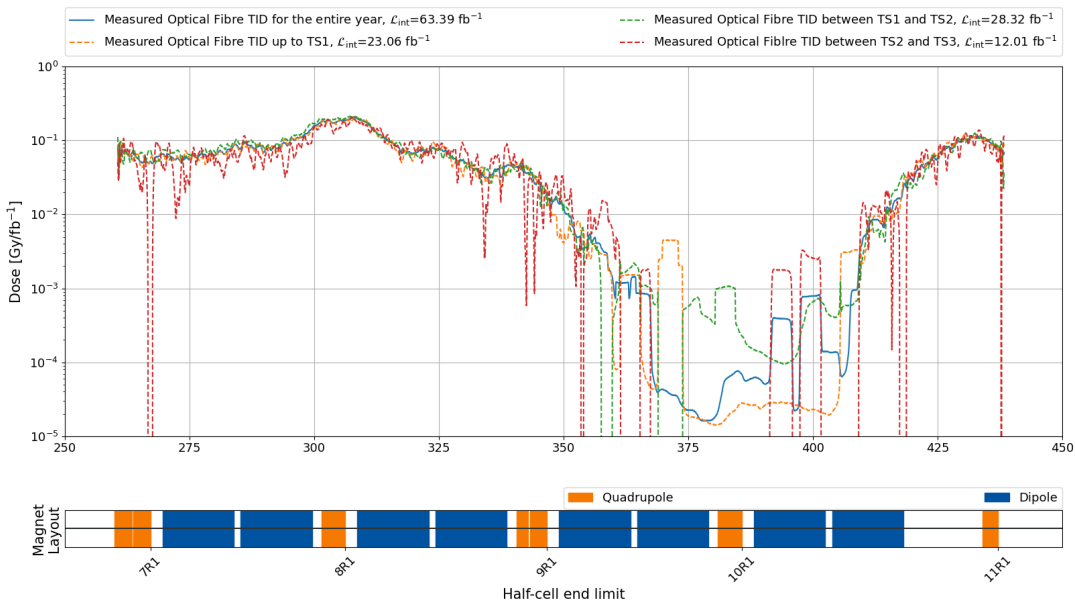


Figure 6.22: Optical fibre passive measurements in 2018 at IP1 DS, measured at the three technical stops. The values recorded in the region from 370 to 420 m often fell below the detection limit of the OF sensor.

The initial simulated TID values are extracted at the optical fibre position in air, using the standard scoring for such simulations with voxel of  $20 \times 20 \times 50 \text{ cm}^3$  ( $X \times Y \times Z$ ). However, this method presents

several drawbacks as already highlighted by section 5.4.3, and as apparent from Figure 6.23, the most prominent being the general overestimation of the data. This launched further investigations in the modelling of both the optical fibre sensor, and of the beamline elements.

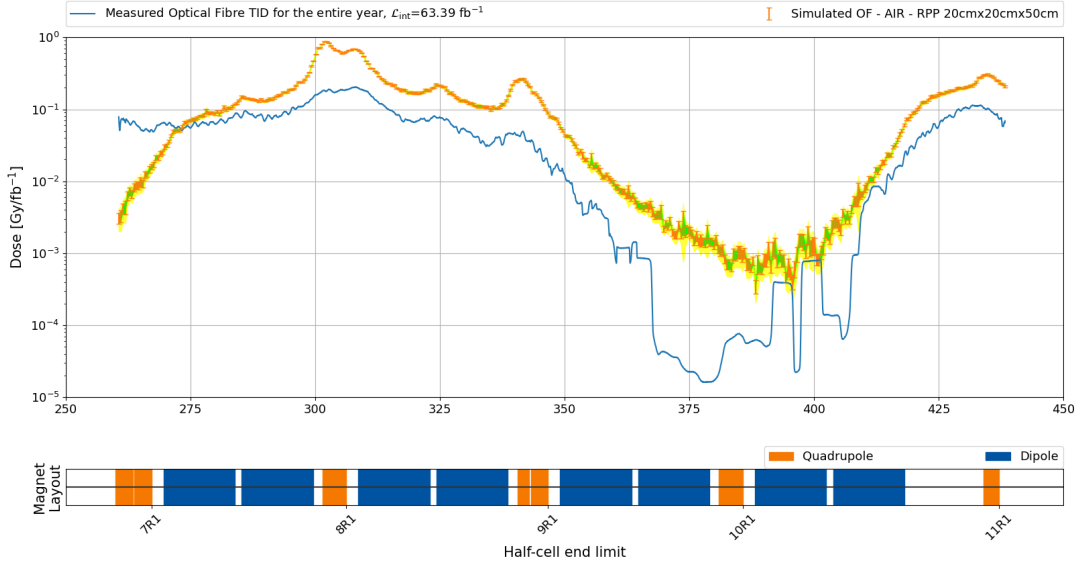


Figure 6.23: Initial optical fibre data vs. FLUKA comparison for the 2018 passive measurements in IP1 DS. The simulation results have been obtained using the two-step approach for increased statistics, yielding as an artefact the undersimulation up to 290 m.

Following the updated OF implementation of CHARM (see Section 5.4.3), the final FLUKA model of the OF at the LHC consisted of a cylinder made of SiO<sub>2</sub> with a size of 1 x 1 x 50 cm<sup>3</sup> (X x Y x Z). The longitudinal direction is chosen to match the 1 m measured data accuracy [61], whereas the transversal size is the main responsible of simulation artefacts, such as self-shielding or build-up effects (see Section 6.7.4 for a more detailed discussion about this topic).

The final results of Figure 6.24 exhibit a good agreement, with a (TID weighted) ratio average of  $0.77 \pm 0.32$  (standard deviation). It is a slightly lesser agreement level compared to the one of CHARM ( $0.93 \pm 0.24$  and  $0.99 \pm 0.32$ ), as it overestimates the measured data by 23%. Nevertheless, this is fully explained by the increased size of the simulation geometry and the more complex radiation source.

There seems to be an overestimation near the magnet interconnects, pointing to possible mismodeling. The interconnections are responsible of ensuring the continuity of several functions (vacuum enclosures, beam pipe image currents, cryogenic circuits, electrical power supply, and thermal insulation) between the cryostat magnets of the LHC. Indeed, after checking the implemented model, there is some material

budget missing coming from the absence of the endcaps for the DS quadrupoles and a thinner layer of the interconnect's tube. On-going efforts include correcting these models, which result in a lower simulated radiation level due to the shielding coming from the additional material.

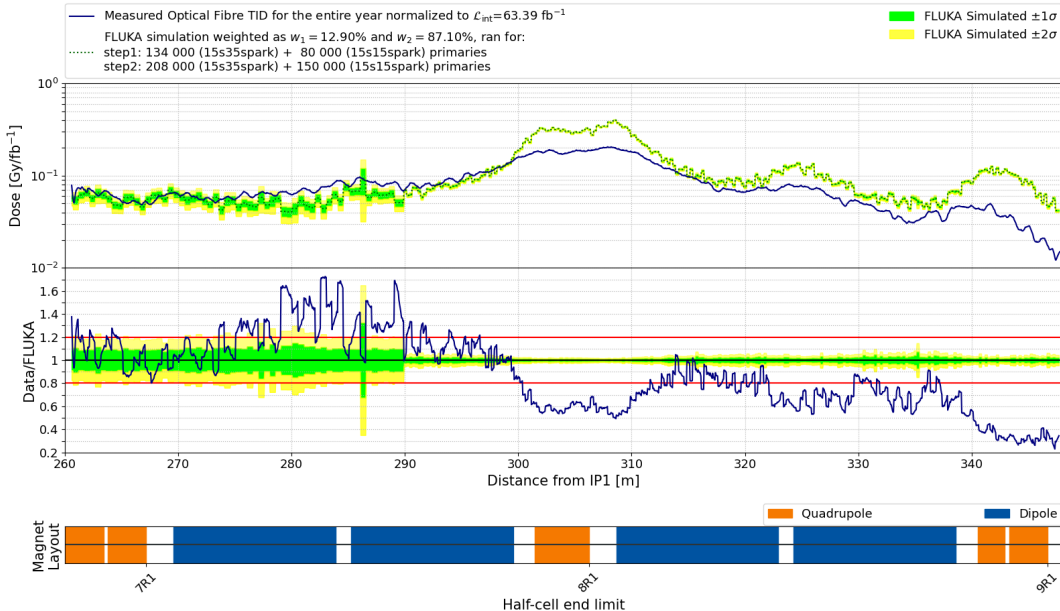


Figure 6.24: Comparison of optical fibre measured data and FLUKA simulated values for the 2018 passive measurements in IP1 DS. Two simulated configurations (with TCL5 closed at  $15\sigma$  and open at  $35\sigma$ ) have been used for this comparison.

### 6.4.3 RadMON RADFETs benchmark

There are two RADFETs on the deployed RadMONs (as described in section 4.2.2), measuring independently the TID. On the FLUKA side, the TID is deposited in AIR in a voxel of  $20 \times 20 \times 50 \text{ cm}^3$  ( $X \times Y \times Z$ ), with its already discussed drawbacks. Nevertheless, the radiation levels shown in Figures 6.25 (2016), 6.26 (2017) and 6.27 (2018) for IP1 exhibit average ratios of measured to FLUKA simulated values that are either systematically oversimulated, but always within a factor of 2 for the first RADFET, located on the RadMON motherboard, or undersimulated for the second RADFET, which is deported in a different location for some RadMONs (especially in 2018, to monitor the quench protection system).

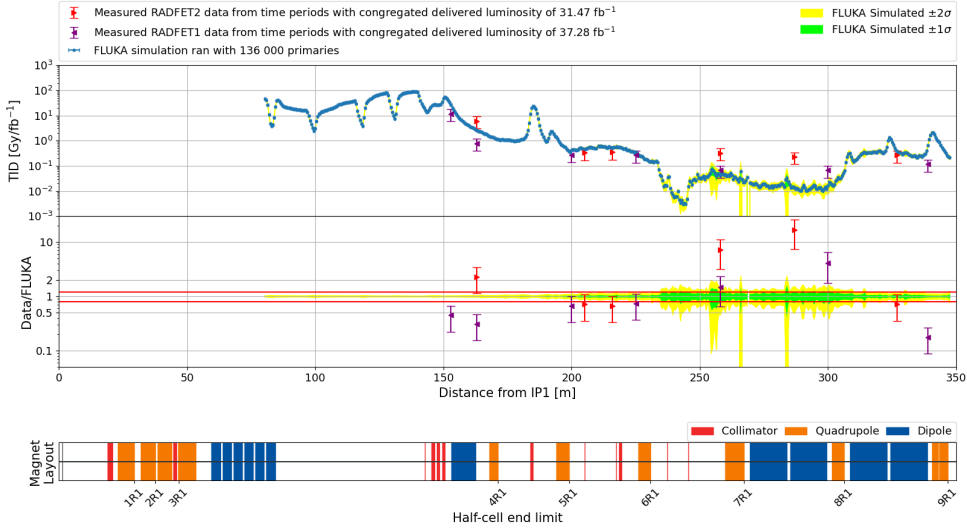


Figure 6.25: Comparison between RadMON TID data and FLUKA predictions for IP1 in 2016 for TCL456: 15s-15s-20s RP: OUT.

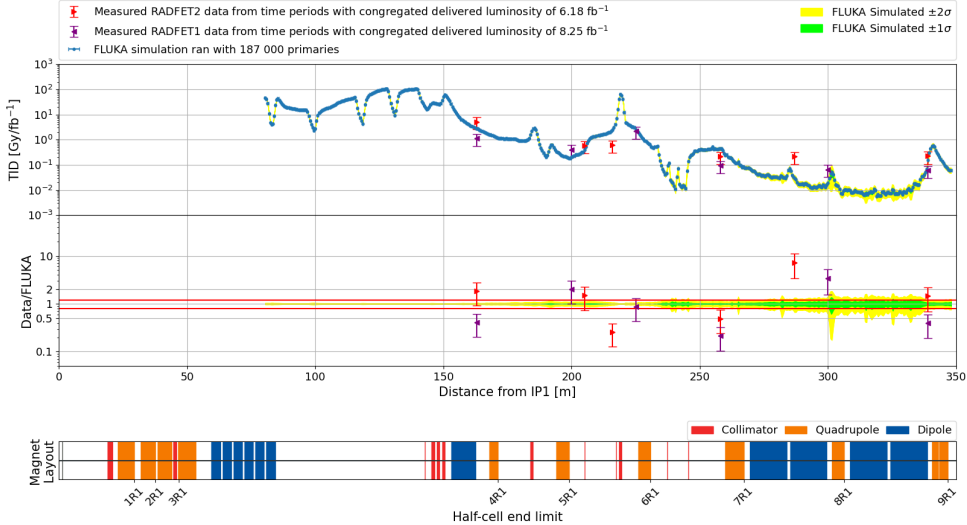


Figure 6.26: Comparison between RadMON TID data and FLUKA predictions for IP1 in 2017 for TCL456: 15s-35s-20s RP: IN.

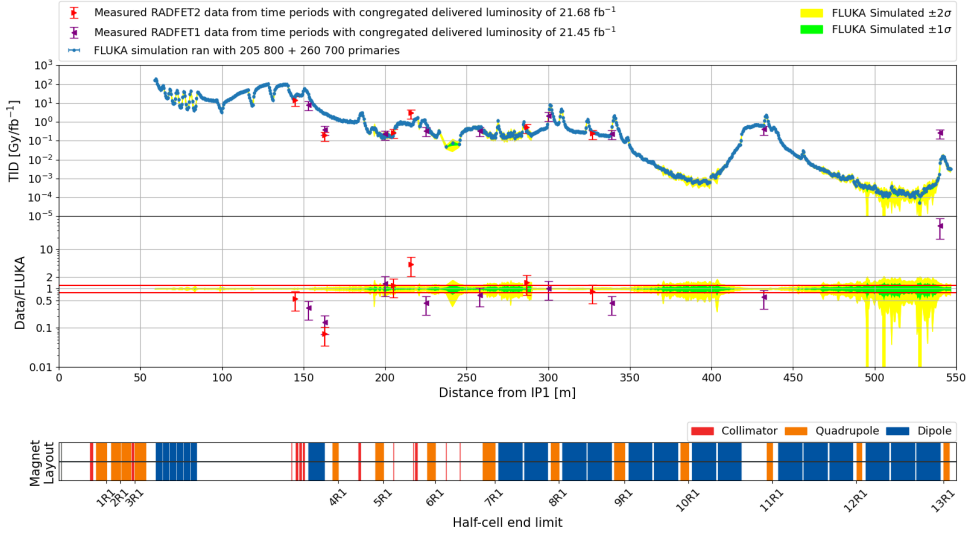


Figure 6.27: Comparison between RadMON TID data and FLUKA predictions for IP1 in 2018 TCL456: 15s-35s-park RP: IN. The last data point at 540 m is discarded from the average ratio calculation.

Table 6.4: Average (AVG±STD) RadMON ratios of measured TID data to FLUKA simulated values.

YEAR	RADFET	Measured data to FLUKA ratio		
		AVG	STD	STD [%]
2016	1	0.47	0.52	110.58
	2	2.75	2.62	95.42
2017	1	0.87	0.51	58.05
	2	1.77	1.05	59.28
2018	1	0.48	0.14	28.74
	2	1.19	0.60	50.63

## 6.5 SEU induced effects in RadMONs results

The only radiation detector installed at the LHC capable of measuring single event upsets (SEU) and, through its calibration, the high energy hadrons equivalent (HEHeq) and thermal energy neutron (THN) fluences is the RadMON (see section 4.2.2). However, only the RadMON V6 is capable of discriminating thermal neutrons and they were deployed only in some regions and only in 2018, hence the thermal neutron analysis is not presented within this thesis.

The analysis presented in this thesis focuses both on the RadMONs installed below the beam line (at

floor level), as well as those placed in the shielded alcoves adjacent to the LHC tunnel (UJ16, UJ17, RR17). The latter RadMONs are not in direct line of sight of the beam line, thereby being situated in a lower radiation field.

FLUKA is capable of evaluating the fluences of high-energy hadrons and thermal neutrons, which are scored using a track length estimator (USRTRACK), capable of discriminating the differential energy of the particles of interest (see Figures 6.6, 6.7 and 6.9). Special scoring regions are implemented in the FLUKA geometry of the LHC for the RadMON locations in the tunnel and the shielded alcoves, as well as in additional regions of generic interest. If the HEHeq and THNeq are known, the SEU response of a RadMON placed in that location can be estimated by applying Eq. 3.1.

Table 6.5: Comparison of data vs FLUKA for RadMON SEE response in IP1.

(a) Table for 2016

RadMON name	Measured Fluence [cm <sup>-2</sup> /fb <sup>-1</sup> ]	Measured Error (Systematic + Statistic) [%]	Simulated Fluence [cm <sup>-2</sup> /fb <sup>-1</sup> ]	Simulation Error [%]	Measured/ Simulated Ratio	Total Error [%]
SIMA.UJ16.1RM01S	4.53E+06	60	4.46E+06	33	<b>1.02</b>	68
SIMA.UJ16.1RM02S	8.96E+07	50	1.48E+08	5	<b>0.61</b>	50
SIMA.UJ17.1RM03S	6.80E+09	50	8.91E+09	1	<b>0.76</b>	50
SIMA.RR17.1RM11S	1.47E+07	55	2.99E+07	22	<b>0.49</b>	59
SIMA.RR17.1RM12S	4.84E+06	65	2.73E+06	53	<b>1.77</b>	84
SIMA.RR17.1RM13S	2.92E+06	102	2.39E+06	59	<b>1.22</b>	118

(b) Table for 2017

RadMON name	Measured Fluence [cm <sup>-2</sup> /fb <sup>-1</sup> ]	Measured Error (Systematic + Statistic) [%]	Simulated Fluence [cm <sup>-2</sup> /fb <sup>-1</sup> ]	Simulation Error [%]	Measured/ Simulated Ratio	Total Error [%]
SIMA.UJ16.1RM01S	4.53E+06	78	4.16E+06	28	<b>1.09</b>	83
SIMA.UJ16.1RM02S	1.07E+08	55	1.40E+08	4	<b>0.76</b>	55
SIMA.UJ17.1RM03S	6.42E+09	50	8.86E+09	1	<b>0.73</b>	50
SIMA.RR17.1RM11S	9.84E+07	51	1.57E+08	8	<b>0.63</b>	51
SIMA.RR17.1RM12S	7.93E+06	60	1.70E+07	19	<b>0.47</b>	63
SIMA.RR17.1RM13S	6.21E+06	65	1.71E+07	18	<b>0.36</b>	67

(c) Table for 2018

RadMON name	Measured Fluence [cm <sup>-2</sup> /fb <sup>-1</sup> ]	Measured Error (Systematic + Statistic) [%]	Simulated Fluence [cm <sup>-2</sup> /fb <sup>-1</sup> ]	Simulation Error [%]	Measured/ Simulated Ratio	Total Error [%]
SIMA.UL16.1RM01S	1.09E+05	54	1.73E+05	40	<b>0.63</b>	67
SIMA.UJ16.1RM02S	3.63E+06	51	9.38E+06	7	<b>0.39</b>	52
SIMA.RR17.1RM11S	3.21E+07	50	4.00E+07	15	<b>0.80</b>	52
SIMA.RR17.1RM12S	2.11E+06	51	5.18E+06	50	<b>0.41</b>	71
SIMA.RR17.1RM13S	4.01E+06	50	6.29E+06	36	<b>0.64</b>	62

Similar studies have been carried out to estimate the number of SEUs in the LHC, for example References [83] (Tables 1, 2, 3) and [115] (notably Table VII).

Compared to the BLMs, there are only a handful of RadMONs in the regions under investigation in this thesis. Nevertheless, they represent crucial data points that can be benchmarked. In addition to the systematic uncertainty of 50% that is considered as a result of the CHARM benchmark (see Section 5.4.2), the RadMON performs a counting experiment of SEU (i.e. Poisson statistics) with its associated (relative) statistical error of  $1/\sqrt{N}$ . The number of SEUs is converted to HEHeq fluence via Equation 3.14. Together, they are considered as measured uncertainty, whereas the simulation error is given by the Monte Carlo statistics.

### 6.5.1 Shielded alcoves RadMONs benchmark

The benchmark (measured and simulated) data for the RadMONs located in the shielded alcoves are shown in Tables 6.5. The ratios of measured data to FLUKA for each year are:  $0.76 \pm 0.47$  (2016),  $0.72 \pm 0.25$  (2017) and  $0.73 \pm 0.17$  (2018).

### 6.5.2 Tunnel RadMONs benchmark

The results are given in Figures 6.28 (2016), 6.29 (2017) and 6.30 (2018) for IP1 and in 6.31 (2018) for IP5. Considering the complex accelerator environment and the heterogeneity of the radiation field, the observed agreement is considered to be generally good: the FLUKA predictions reproduce well the measured data trend and the agreement is within a factor of 2 for most RadMONs. The local outliers can generate further work in order to understand the origin of discrepancies, for which the possible sources are discussed in Section 6.7.

Table 6.7: Average (AVG $\pm$ STD) of the ratios of measured RadMON SEUs data to FLUKA simulated values.

IP	Year	Measured data to FLUKA ratios		
		AVG	STD	STD [%]
1	2016	1.03	0.46	44.95
	2017	0.91	0.15	16.59
	2018	0.69	0.38	55.36
5	2018	0.55	0.15	27.26

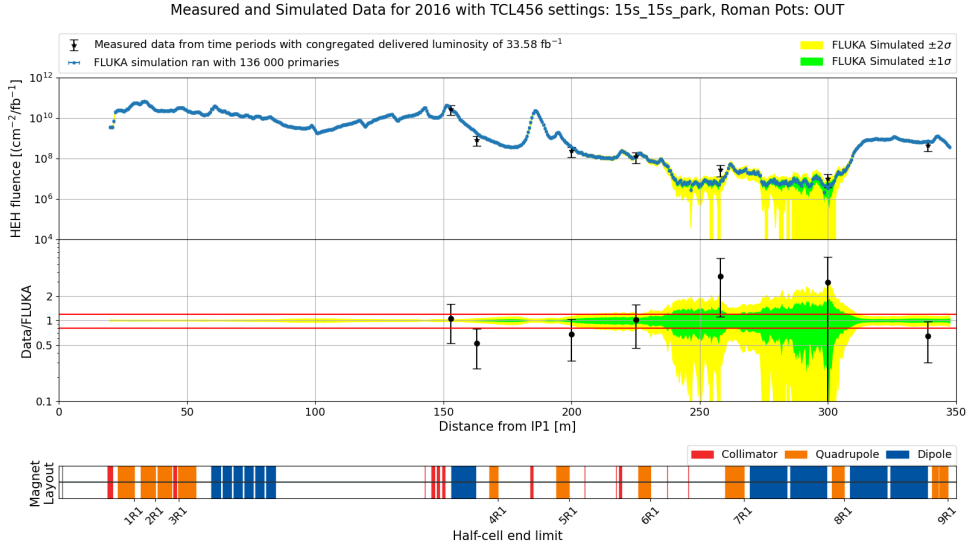


Figure 6.28: Comparison of RadMON SEU measured data and FLUKA simulated HEHeq fluence for IP1 in 2016 TCL456: 15s-15s-park RP: OUT.

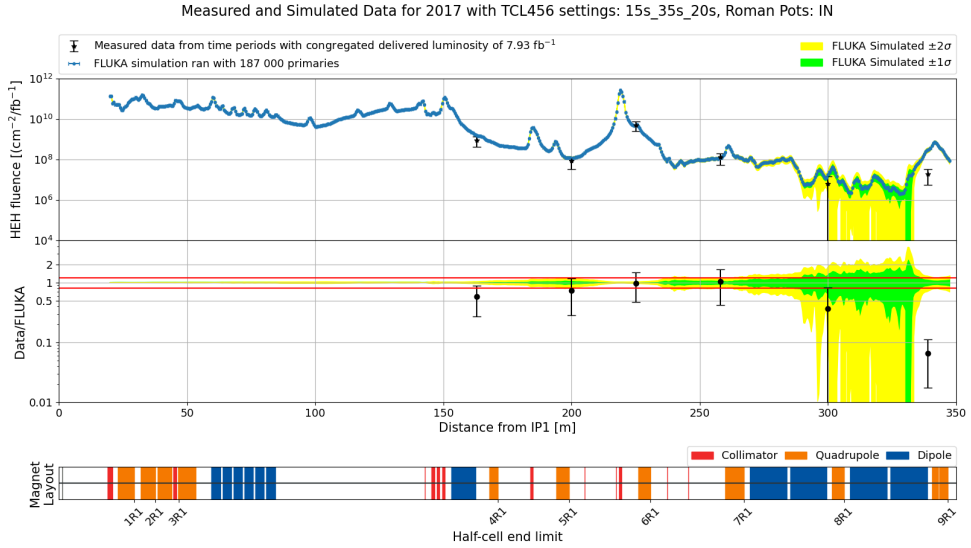


Figure 6.29: Comparison of RadMON SEU measured data and FLUKA simulated HEHeq fluence for IP1 in 2017 TCL456: 15s-35s-20S RP: IN.

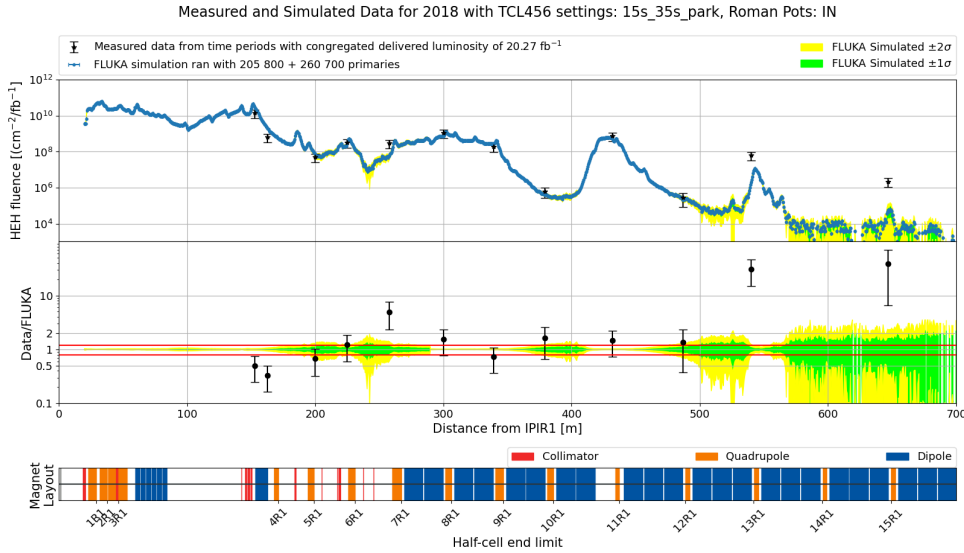


Figure 6.30: Comparison of RadMON SEU measured data and FLUKA simulated HEHeq fluence for IP1 in 2018 TCL456: 15s-35s-park RP: IN. The last two points located in the ARC are discarded from the agreement level computation, as the collision debris are not expected to be the main source of radiation.

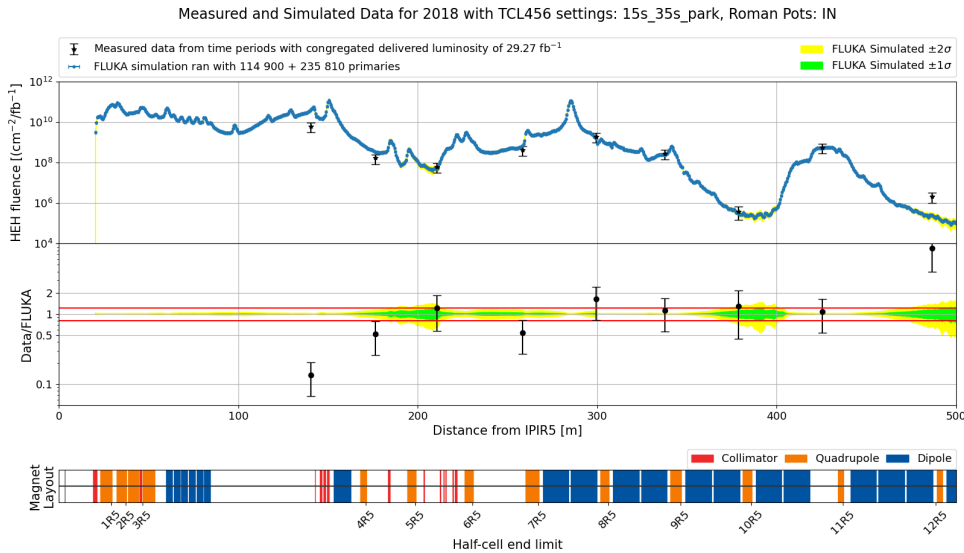


Figure 6.31: Comparison of RadMON SEU measured data and FLUKA simulated HEHeq fluence for IP5 in 2018 TCL456: 15s-35s-park RP: IN.

## 6.6 Agreement levels for FLUKA radiation level specifications

The average ratios of measured data to FLUKA simulated values are almost always (with isolated outliers) within one standard deviation from unity, regardless of the monitor, scored quantity or LHC configuration. However, for R2E applications, one is interested in the worst case scenario error, considering that the most common sources of uncertainty (see next section) have been removed. This is the reason why the disagreement level (DL) for each monitor and location is computed as:

$$DL = \begin{cases} AVG + STD & \text{if } AVG \geq 1 \\ AVG - STD & \text{if } AVG < 1 \end{cases} \quad (6.1)$$

Then, the agreement level (AL) for one monitor type is taken as the maximum over all configurations (i.e. LHC years of operation):

$$AL = \max(|1 - DL|) \quad (6.2)$$

yielding the values in Table 6.8. The worst agreement is for the RadMON TID in the LHC tunnel, for which the agreement is 105%, which implies that values twice as high could be expected. This translates into a factor of 2 as the worst agreement level.

Table 6.8: Agreement levels for the LHC radiation monitors.

Monitor	Region	Distance from IP	Agreement levels [%]				
			Worst case scenario	2016 IP1	2017 IP1	2018 IP1	2018 IP5
BLM	LSS (Inner Triplet)	0 to 60 m	26	21	15	14	26
	LSS (after TAN)	140 to 269 m	40	27	39	40	35
	DS (single step)	269 to 348 m	88	70	65	18	88
	DS (second step)	290 to 450 m	47	-	-	47	32
RadMON	tunnel (TID)	-	105	105	63	67	-
	tunnel (HEHeq)	-	69	43	24	69	60
	shielded alcoves	-	56	29	47	56	-
OF	DS (single + second step)	260 to 350 m	45	-	-	45	-

## 6.7 Uncertainties and limitations

Considering the complexity of the IP1 beam line, the measured results are in good agreement with the predicted values from FLUKA. However, they should be treated with care due to the associated uncertainties, some that are already known.

### 6.7.1 Integrated luminosity scaling

The comparison is particularly sensitive to normalization: the actual number of lost protons in IR1, which are used to scale the simulation results. Any changes in this number will directly impact the results of all the radiation monitors locations. In this thesis, the luminosity values delivered by LHC was used, and not the one useful for physics experiments that is usually reported by the experiments. The difference is not larger than 5-7% [23, 24], caused by several factors, for example the dead time of detectors.

### 6.7.2 Thermal neutron sensitivity

Another point of uncertainty is the contribution from thermal neutrons. Depending on the actual water content (resulting in different concentrations of hydrogen), which is used for the concrete in the tunnel and shielding walls, the thermal neutron fluence may significantly change. Also, equipment installed in the proximity of the RadMONs may alter the thermal neutron field, especially in the Shielded Alcoves. Experience from the better understood CHARM simulations shows that there is a tendency for the simulations to overestimate the thermal neutron fluence. This affects only the HEHeq measurements for the RadMON V5, as an assumption for the R-factor has to be made; this is no longer the case for the RadMON v6.

### 6.7.3 Geometry mismodelling

Locally, some radiation monitors are placed in the close proximity of strong gradients of radiation, implying that even a slightly shifted position could significantly change the overall agreement (e.g. 1 m gives almost a factor of 10 for BLMEI.06R1.B1E10\_XRP.A6R1). Some BLMs and RadMONs would potentially see more radiation, while others would see less. Nevertheless, it is generally considered that for the LHC geometry, the beam lines elements are modelled correctly within a 10 cm accuracy and only the radiation monitors may have up to a 1 m shift, as was one identified case.

### 6.7.4 Approximations due to statistical convergence

The simulated models cannot be 100% replicas of the experimental devices due to unavoidable inhomogeneities in the material and dimension uncertainties. Moreover, some detectors are explicitly modelled with an oversized active area, due to the small size that would be unfeasible for sufficient simulations statistics. This may cause several effects, but most important for our study are two: self-shielding and build-up. The differential energy deposition with distance  $dE/dx$  (also known as stopping power) varies depending on the particle type and on the material.

In particular, the optical fibre model was studied for such potential effects, as it is the one with the least realistic model. A secondary simulation (similar to the one used for the CHARM RadMON TID deposition) was used to quantify the dose-depth curves for different particles in SiO<sub>2</sub>. Figure 6.32 exhibits for the electromagnetic components (photons, electrons and positrons) the build-up effect in

the first millimeters and the self-shielding effect after 0.1 centimeters. The hadronic particle species (neutrons, protons, pions) are relatively more constant.

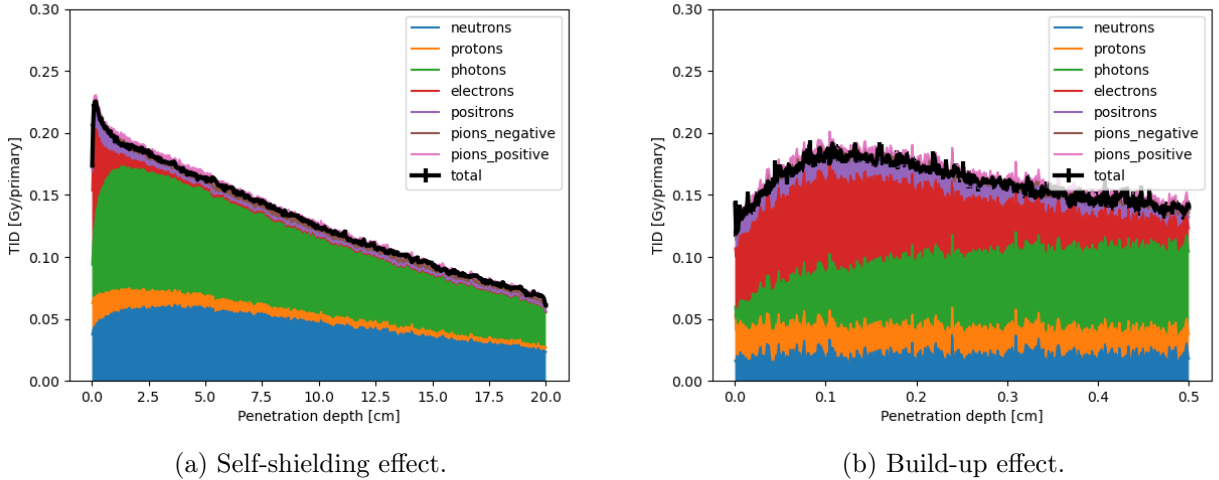


Figure 6.32: Longitudinal dose deposition for several particle species as a function of depth in a cylinder made of  $\text{SiO}_2$ , exhibiting (a) self-shielding and (b) build-up effects. The radiation field composition is as simulated by FLUKA for the tunnel region in the DS of IP1 at the optical fibre location (see Figure 6.7c).

### 6.7.5 Energy deposition dependency on simulated material

In addition to the measurement of radiation levels with deployed monitors, the MCWG group within the R2E project is in charge of providing the equipment owners with radiation levels in specific positions of their equipment or in other desired locations. However, it is not practical to implement each inquired configuration and (possibly new) equipment. For this reason, the specified radiation levels are given as mostly scored in air, with its already known drawbacks. An ongoing study is to quantify the difference in dose deposition different materials, as already indicated by Figure 6.33 for the optical fibre between Air and  $\text{SiO}_2$ .

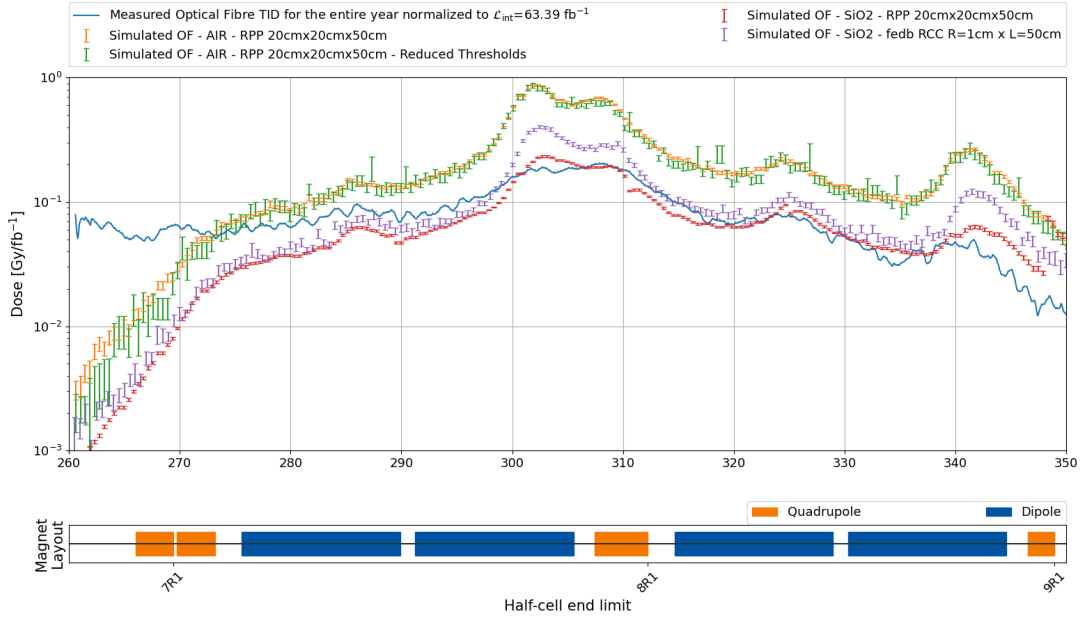


Figure 6.33: FLUKA calculation of the TID in the OF based on different models, namely: 20x20x50 cm<sup>3</sup> segments made of AIR (orange line), 20x20x50 cm<sup>3</sup> segments made of AIR with reduced electromagnetic thresholds (green line), 20x20x50 cm<sup>3</sup> segments made of SiO<sub>2</sub> (red line), and 50 cm long with 1 cm radius cylinder segments made of SiO<sub>2</sub> (purple line). Note in particular the factor 5 difference between the models made out of AIR and SiO<sub>2</sub> ones. The undersimulated values before 280 m are a known consequence due to the second step simulation procedure.

## 6.8 Discussion and future work

These benchmarking results are of paramount importance to cross check the two independent tools used for assessing the radiation levels in the large hadron collider (LHC) accelerator environment: (i) measured data from radiation monitors, and (ii) FLUKA simulations. Used for the design of future accelerators and for the lifetime usage of several beam elements, the FLUKA Monte Carlo code predicts several quantities for which no measurements are available, e.g. the total TID received by sensitive equipment or cables, and one must make sure that these equipments will resist the radiation levels they will actually receive. Therefore, this thesis aimed to quantify the level of agreement that FLUKA can achieve in the very difficult scenario of the accelerator, which consists of a complex radiation field, a geometry that spans hundreds of meters and for the a radiation source far away from the region of interest.

The general level of agreement that results from this study is a factor of 2 or better, for selected radiation monitors, quantities and/or locations. In practical terms, this implies that it is reasonable

to apply a safety margin of this order, whenever radiation levels are specified for LHC installations, equipment locations or feasibility studies for future accelerator.

Nevertheless, the factor of 2 safety margin is often not the limiting factor in such specifications. Some specifications are done via extracting the dose in AIR, but in other materials the deposited dose is lower (e.g. almost 5 times for the case of SiO<sub>2</sub>, as was the case for the optical fibre study). All these additional estimates indicate that the FLUKA simulations of the LHC accelerator are one of the most reliable tools at hand to evaluate the radiation levels suffered by electronics, and equipment at large.

Future work consists in correcting all possible discrepancies by identifying the source of inconsistency, either from the measurement side (radiation monitor not functioning properly, error in the data analysis chain, etc.) or on the simulation side (position inaccuracy, equipment mismodeling, etc.). This procedure increase the level of agreement for the benchmark over time, thereby increasing the accuracy of both measurements and simulations.

Moreover, this thesis has focused on the high luminosity experiments (IP1 - ATLAS and IP5 - CMS), but similar work is being carried out for the other insertion regions (IR7 - Dump, IR6 - Collimation and IP8 - LHCb), with priority given to the areas with the highest total radiation levels. Nevertheless, the lower radiation level insertion regions are also exposed to R2E effects and are used to monitor and improve the quality of the beam. For example, IR4 contains several equipment units crucial for LHC operation, e.g. the accelerating radio-frequency cavities.

# Chapter 7

## Conclusions

The study carried out in this thesis consisted of benchmarking the radiation levels simulated by the FLUKA Monte Carlo code using a comprehensive set of measurements of the total ionizing dose (TID) and fluences of high energy hadron (HEH) and thermal neutrons (THN), which are of particular interest for radiation effects to electronics (R2E), using radiation monitors deployed in the CERN high energy accelerator mixed-field (CHARM) facility for testing and the large hadron collider (LHC) tunnel.

Test measurements have been carried out at the CHARM facility, which is capable to generate a variety of mixed field radiation depending on the use of target material and shieldings. It is used to quantify the systematic uncertainties for the comparison between measured data and simulations for three types of detectors that have been investigated. Beam loss monitors (BLMs) are ionizing gas ( $N_2$ ) chambers explicitly modelled in FLUKA, which measure TID rates with good time resolution. Two such detectors have been deployed at CHARM. The average ratio of the measured values and FLUKA simulated ones is of  $0.92 \pm 0.18$  (standard deviation) for the highly irradiated BLM1 and  $0.73 \pm 0.17$  (i.e. 27% simulation overestimation) for the more shielded BLM2. The FLUKA model of the optical fibre sensor made out of  $SiO_2$  reproduced very well the measured 1D profile. The ratio of measured to simulated dose generally agreed within 30% variation ( $0.93 \pm 0.24$  for no shielding and  $0.99 \pm 0.32$  for a fully shielding use case) with local fluctuations exceeding the margin in both directions. The RadMON monitors acted both as TID and fluence detectors. Two RADFETs achieved an average agreement between measurements and simulated TID values of  $0.82 \pm 0.23$  for the TID deposition in AIR and of  $1.01 \pm 0.36$  for a second step approach with a fully modelled RADFET. The fluence detectors achieved a satisfactory agreement of measured to simulated values for HEH fluence of  $0.78 \pm 0.16$  (i.e. overestimation by 20%), whereas for thermal-energy neutrons the ratio decreases to  $0.49 \pm 0.22$  (i.e. overestimation by a factor of 2). For the R-factor, which quantifies the ratio of thermal-energy neutrons to high energy hadrons, the measured to simulated ratio is  $0.47 \pm 0.15$ , due to the lower thermal-energy neutron ratio. These results lead to a conservative estimation via simulations of possible single event effects (SEE) induced in the electronics.

Having determined the systematic uncertainties in the more controlled and better understood environment at CHARM, the same benchmark studies have also been performed for the LHC accelerator with a very large simulation size (a tunnel section with radius of roughly 2.5 m spanning up to 700 m and contains additional shielded alcoves) and a complex radiation source consisting of collision debris from the interaction point of particles lost from interactions between the beam and the machine ele-

ments. The LHC has been operated under various conditions that impact both the local and the global radiation levels. For this reason, the first task was to select the measured data corresponding only to luminosity producing collisions data sets and for well defined operational parameters that can be simulated. The settings used for most of the delivered luminosity were selected for the simulations with FLUKA.

As the main result of the thesis, the radiation levels in the LHC tunnel near the collision points could be simulated with a good agreement with the measured data within a factor of 2 and often much better, depending on the radiation monitors and location. The BLM simulated values show an average agreement within 40% up to 269 m from the interaction point (IP), i.e. in the long straight section (LSS), regardless of the configuration. The agreement is better closer to the collision point and fades away with the distance to 40%(80%) for the dispersion suppressor (DS) region in the second (single) step. After 550 m, the collision debris no longer represents the main source of radiation. The simulated optical fibre sensor, providing only a passive measurement, shows a good agreement with a (TID weighted) average ratio of measured to simulated values of  $0.77 \pm 0.32$ , which translates into a 45% agreement level. The RADFET TID measurements on the RadMON module are within a factor of 2 (with one outlier) with the FLUKA simulated values. When it comes to the HEH fluence benchmark, the RadMON measurements are also generally also overestimated by the simulation, albeit to a lower extent with data to FLUKA ratios ranging from 0.56 to 1.03.

In conclusion, benchmark exercises such as those presented in this work are crucial for cross-checks of the validation of the tools used for radiation levels predictions. They allow for the determination of the systematic uncertainties and deviations to be expected for the LHC machine for the Run 3 and High-Luminosity LHC operation.

# Appendix A

## Particle accelerators and colliders

This chapter gives an introduction to particle accelerators in the context of this thesis. Basic principles of particle accelerators, as well as beam collider experiments, are discussed. The recurrent concepts of luminosity, center of mass energy, cross section and event rates are briefly described, followed by the basics of accelerator physics.

### A.1 Motivation

The state-of-the-art tool for fundamental research in particle physics are high energy accelerators. Their importance and applications can be appreciated when one described one figure of merit, the beam energy. If one intends to compare accelerators to large “microscopes”, then the spatial resolution that is resolved increases with beam energy, according to the de Broglie equation. The relation between the wavelength  $\lambda$  of a wave packet and its momentum  $\vec{p}$  is given via Planck’s constant  $h$  as:

$$\lambda = \frac{h}{|\vec{p}|} \quad (\text{A.1})$$

Therefore, larger momenta correspond to shorter wavelengths and access to smaller structures. Similarly, one can have access to the early universe by exploiting the large energy (and the large uncertainty thereof) via the time-energy uncertainty relation [116]:

$$\Delta E \cdot \Delta t \geq \frac{\hbar}{2} \quad (\text{A.2})$$

In addition, it is possible to use accelerators to produce new particles, according to Einstein’s famous equation:

$$E = mc^2 \quad (\text{A.3})$$

i.e. this requires the more energy the heavier the particles are. Because beams are circulated for several hours accelerators are based on beams of stable particles and antiparticles, such as  $e^-$ ,  $e^+$  (at LEP),  $p$  (at LHC) or  $\bar{p}$ .

Particle accelerators are used to accelerate particles to very high energies. The two main accelerator categories that are currently employed worldwide are: linear, where the beam of particles travels along a straight line, e.g. SLAC [117]; and circular, where the beam circulates around the loop, e.g. LHC. The most powerful accelerators are circular, as this allows the beam to be accelerated continuously as it can pass through the acceleration region (radio frequency cavities) multiple times.

Particle accelerators can be categorized differently in fixed target experiments (where the beam hits a stationary target), or collider experiments (that collide two counter-circulating beams with each other). In the case of a fixed target experiment, the center of mass energy grows with the incoming beam energy as  $\sqrt{s} \approx \sqrt{E_{inc}}$ , whereas in beam-beam collisions, we find a linear increase  $\sqrt{s} \approx E_{CM} = 2E_{inc}$ .

## A.2 Acceleration methods and the radio frequency cavity

According to Lorentz force definition (Equation A.4), only charged particles can interact with the electromagnetic field directly. To increase the particles energy an electric field  $\mathbf{E}$  is required, and to focus and steer them a magnetic one  $\mathbf{B}$  is used.

$$\vec{F} = q\vec{E} + q\vec{v} \times \vec{B} \quad (\text{A.4})$$

Although the electric field could also be used for steering, it is more efficient to use magnetic fields, since it scales with the momentum in an ultrarelativistic regime encountered at the LHC. One could also use an electrostatic field to accelerate charged particles. Since the maximal available potential difference (Tandem Van de Graaff accelerators [118]) is limited to 25 MV, one could only accelerate particles up to 25 MeV. However, the fact that the electrostatic field is conservative:

$$\oint \vec{E} \cdot d\vec{l} = 0 \quad (\text{A.5})$$

implies that the energy transfer only depends on the potential difference and not on the path. Therefore, circulating the beam in an electrostatic field does not lead to an increasing acceleration.

The problem is solved by using several times a small but variable potential difference. This can be done using linear or circular machines. In the latter, one can use several times the same acceleration (radio frequency) cavity. In the case of a circular accelerator, the particles will receive a certain amount of energy at every turn through the cavity, assuming they are in phase with the accelerating potential. Because of the inertia principle, one further needs an increasingly powerful magnetic field providing the centripetal force to keep particles on a circular path.

In a cyclotron, particles are injected in the center and accelerated with a variable potential while a magnetic field  $\mathbf{B}$  keeps them on spiral trajectories. Finally, particles are extracted and used in experiment. For a particle moving in the cyclotron, the centripetal and Lorentz forces are balanced:

$$m \frac{v^2}{\rho} = qvB \implies \rho = \frac{p}{qB} \equiv \text{const.} \quad (\text{A.6})$$

In the case of the synchrotron, the trajectory radius is kept constant. This is achieved by dipole magnets, while high frequency cavities are used to accelerate the particles. Setting the particle charge  $q = Ze$  (with  $e$  the unit electron charge) and using the SI units  $cp[\text{eV}] = czB\rho = 3 \cdot 10^8 \frac{m}{s} zB[T]\rho[m]$ , leads to a momentum definition of:

$$p \left[ \frac{\text{GeV}}{c} \right] = 0.3ZB[T]\rho[m] \quad (\text{A.7})$$

The maximal energy is of order 20 MeV for cyclotrons and up to 600 MeV for synchrotrons. Consider now the LHC at CERN: With a circumference of 27 km, yielding a radius of 4.3 km, an average magnetic field of 5.4 T<sup>1</sup> would be needed to keep protons with momentum 7 TeV/c on circular trajectories. However, since the LHC contains also long straight sections and the magnetic field cannot be fully continuous, in practice only 60-70% of the LHC ring is used by dipoles, leading to the requirement of 8.3 T bending magnets.

### A.3 Relevant quantities in accelerator physics

Amongst several quantities describing a collider's performance, two critical ones are the maximum energy of particles and the luminosity. The latter describes the efficiency of collisions, i.e. collision frequency normalised with the interaction cross-section. Often an integrated luminosity is used, which is an integral of the luminosity with respect to time. Typically, the objective is to maximise integrated luminosity obtained at high energy, but there might be exceptions depending on the physics programme of the accelerator.

To define the meaning of luminosity, let us consider head-on collisions of two identical Gaussian shaped beams with dimensions in terms of standard deviation  $\sigma_x$  and  $\sigma_y$ , yielding a transverse size of  $4\pi\sigma_x\sigma_y$ . They circulate in the collider with a revolution frequency  $f$ , and  $I_1$  and  $I_2$  are the intensities of two colliding bunches. Then the luminosity ( $L$ ) can be defined as follows [119]:

$$L = f \frac{I_1 I_2}{4\pi\sigma_x\sigma_y} \quad (\text{A.8})$$

---

<sup>1</sup>Magnetic fields of this magnitude require very large currents and therefore superconductors which only work at low temperatures (about 2 K). The superconducting cables are therefore cooled with liquid helium.

To further elaborate on the beam size ( $\sigma_x$  and  $\sigma_y$ ), the beta function ( $\beta$ ) describes optics (i.e. magnet configuration) of an accelerator. The beta function value at the collision point is denoted as  $\beta^*$ . The beam transverse size ( $\sigma$ ) is connected with the beta function via the beam emittance ( $\epsilon$ ), that describes the spread of particles in position-and-momentum phase space, through the equation (in the simplest case):

$$\sigma_{x,y} = \sqrt{\epsilon_{x,y} \beta_{x,y}} \quad (\text{A.9})$$

According to this equation, the luminosity can be increased by reducing the cross section of the beam (for example, via decreasing the value of a beta function at the collision point ( $\beta_{x,y}^*$ )). Alternatively, it is possible to increase the number of particles in the beam or the revolution frequency.

With a cross section  $\sigma$  of inelastic collisions, one is able to compute how many inelastic collisions occur as the number of events per second  $R$ :

$$R = \sigma L \quad (\text{A.10})$$

In general, the luminosity of an accelerator gradually increases over time, while accelerator physicists learn how to operate the machine and to squeeze the beam size at the intersection point. The integral of the delivered luminosity over time is called integrated luminosity and is a measure of the collected data size.

## A.4 General features at circular colliders

For a circular collider to work properly, some technical problems have to be overcome. First, the particle density in a beam is significantly lower than in a solid/liquid target. In practice, one crosses the beams several times and maximizes the beam intensities. Moreover, it is not possible to set transverse (with respect to beam direction) spread of the particles to zero. The problem of focusing the beam is addressed by using quadrupole magnets, which have focusing properties, but only in one plane, leading to defocusing in the other transverse. The magnetic field of an ideal quadrupole is depicted in Figure A.1. To keep the trajectory inside the vacuum beam pipe and close to the design trajectory, one performs focusing in both planes, so that the particle bunch from the beam oscillates around the design trajectory.

Another issue is that synchotron radiation is produced around the accelerator ring, which is counterproductive as the accelerated particles lose energy. For an angle  $\alpha$  between the velocity and the magnetic field, the power emitted decreases with the fourth power of particle mass:

$$P = \frac{(Ze)^2(E^2 - m^2c^4)^2}{6\pi\epsilon_0 c^5 \rho^2 \sin^2 \alpha} \cdot \frac{1}{m^4} \quad (\text{A.11})$$

where  $(Ze)$  is the charge of the particle/atom,  $E$  and  $m$  are its energy and mass,  $\rho$  is the radius of curvature of the track in the field;  $\epsilon_0$  is the vacuum permittivity and  $c$  is the speed of light.

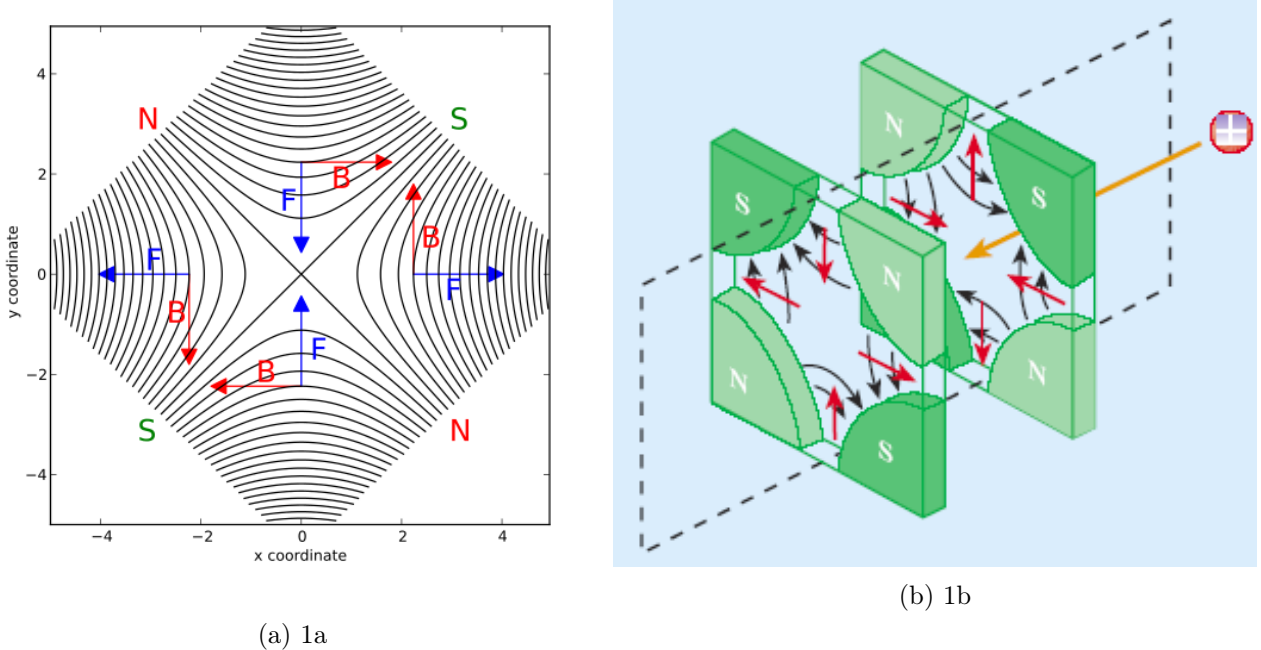


Figure A.1: a) Magnetic field of an idealized quadrupole with forces [120]. b) Two quadrupoles working together to keep the protons squuzed such that the transverse beam size is under control. The former quadrupole acts on the beam width while the latter one acts on the beam height. [121]

Therefore, by using the heavier hadrons instead of leptons, this effect can be decreased overcoming the limits an electron-positron circular collider. Generally, proton-proton colliders are instead limited by the maximum magnetic field; this is why, for example, the LHC achieved a center-of-mass energy 70 times larger than its predecesor, the LEP, although the proton mass is approximatively 2000 times greater than the electron mass.

Furthermore, in order to avoid beam-gas interactions (unintended fixed target collisions, the main source of radiation far away from the interaction points), a high vacuum is needed in the beam-pipe (about  $10^{-9}$  Pa, better than outer space).

In the particle-particle collision scenraio, two beam lines are needed, whereas in the particle-antiparticle scenario one beam line is sufficient, as the two beams can circulate in opposite directions.

Finally, the detector readout systems (data acquisition) represent another crucial part of the setup. At a rate of about  $4 \cdot 10^6$  collisions per second a fast read-out electronic system is necessary to decide which collision information to store and which to discard.



## Appendix B

# LHC interaction regions and sources of radiation

The case of the experimental interaction regions (IR) where collisions occur at the interaction points (IP) is rather straightforward in terms of the main source of radiation (collision debris) and the normalization factors (luminosity). However, the other IRs at the LHC present more complex source terms that are further described in this chapter.

### B.1 IR4: Radio frequency system

Two radio frequency (RF) systems (as well as some of the LHC beam instrumentation) are hosted in IR4, one independent system for each LHC beam, with the purpose of accelerating the beam. Each RF system is composed of eight cavities, each delivering up to 2 MV at top energy, equivalent to an accelerating field of 5 MV/m. With each passage through the RF cavities, each particle gains an energy of 485 keV. For injection energy each RF system has to provide approximately 8 MV, while at top energy up to 16 MV are required. The 450 GeV injection energy of the particles rises to 6.5 TeV in approximately 20 min, bunches having passed through the RF cavities more than 10 million times. During acceleration to the top energy, the field in the LHC magnets increases as the energy of the particles does. Once the top energy is reached, the main role of the LHC RF cavities is to keep the approximately 2 556 proton bunches tight, controlling the bunch length.

### B.2 IR3 and IR7: Collimation systems

During beam operation, individual particles may suffer deviations from the designed path (such as changes in their transverse oscillation amplitudes or variation in their kinetic energies) that would lead to interactions in the beam pipes, beamline elements or even in the detectors. Such an incident is called a beam loss and the scope of the collimation systems is intercept locally such particles to avoid losing them in unwanted locations along the LHC ring and to maximize the cross section of the colliding beams.

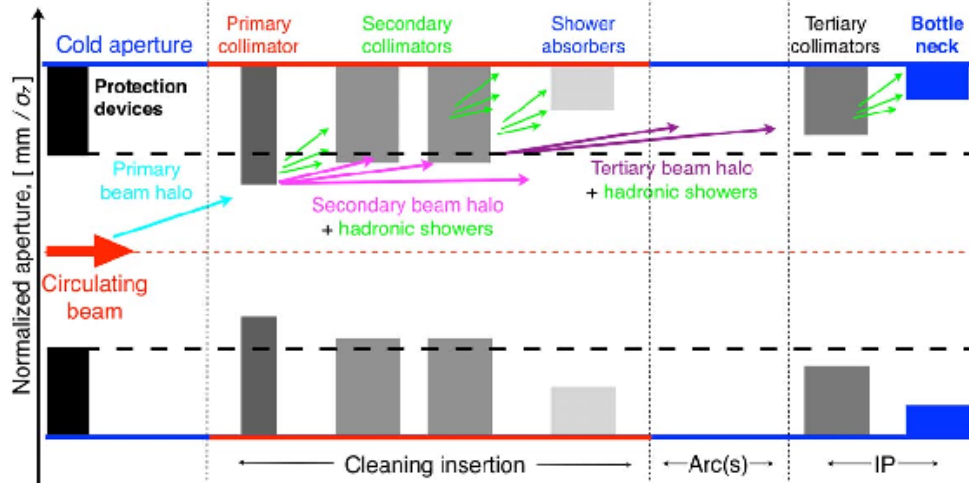


Figure B.1: Key elements of the LHC multi-stage collimation system [122]. The target collimator primary (TCPs) and target collimator secondary (TCSs) are closer to the beam and intercept large beam losses. Therefore, they are made of a carbon fibre composite (CFC) to ensure high robustness. The target collimator absorbers (TCLAs) absorb the particles scattered out of the TCSs and the showers from upstream collimators. They are made of a tungsten alloy in order to stop as much as possible of the incoming energy.

Among other sources, the electromagnetic interaction of the beam particles among themselves, with their environment and with the other beam are responsible for change in beam quality. The bunches of beam particles have a finite length, and this leads to particles receiving slightly lower or higher energies compared to those located in the center of the bunch. As another consequence of this, the magnetic fields in the dipoles will deviate the particles differently, resulting in a transverse offset.

One solution is to suppress particles with transverse oscillation amplitudes or energy deviations (longitudinal oscillation amplitudes) significantly larger than those of the reference particle at the centre of the bunch, which are referred to as beam halo particles. Beam losses should be avoided during operation, in order to guarantee the LHC machine protection, but they cannot be completely suppressed.

A powerful collimation system is required in order to clean the halo particles, especially considering the high intensity beam circulating in the LHC and the associated loss rates of protons, that can be very high. The general purpose of a collimation system is to dispose of beam losses that would otherwise occur at sensitive locations or on accelerator equipment which is not designed to face these losses. Designing a collimation system involves setting up an arrangement of collimators which ensures that losses in superconducting magnets remain below the quench limits for all types of loss rates. The key elements and arrangement of the LHC multi-stage collimation system are shown in Figure B.1.

The betatron amplitudes of stray particles outside the core of the beam are constrained by placing blocks of material (the collimator jaws) close to the circulating beams, thereby absorbing the tails

of the beam. Collimation of off-momentum tails is achieved in a similar way as for betatron tails, by placing collimators at locations of high dispersion, where the particle's transverse offset caused by energy shifts is higher. They are preferably placed in warm regions, as far as possible from the more sensitistive superconducting (cold) magnets.

A similar benchmark exercise to the one proposed in this thesis has been done for the collimation system of IR7 in [123].

### **B.3 IR6: Beam dump systems**

More than 360 MJ are stored within each beam at peak intensity and energy (7 TeV). Fast losses of even fraction of the beam in an uncontrolled manner can already lead to magnet quenches or (in worst case) structural damages of beamline elements. Therefore, a stable and controlled operation is necessary to protect the LHC. In case of such an unstable and potentially dangerous scenario, the beams need to be extracted quickly and in a controlled way. For this reason the LHC has dedicated beam extraction/dump systems that can safely dissipate the energy if required.

IR6 [124] contains the beam dump insertion whose goal is extract the beam in a safe way from each ring of the collider and to transport it to an external absorber, i.e. a beam stop block made of concrete and graphite composite with different densities.

Fast-pulsed kicker and septum magnets are employed for beam extraction, as they kick the circulating beam and deflect it towards the dump line respectively. A dilution magnet reduces the beam intensity by a factor of 100 000 before it collides with the block [125]. Each beam features an independent abort system (as can be seen in Figure 2.2).



# Appendix C

## Example of a request for radiation level studies

The monitoring and calculation working group (MCWG) performs continuous data analysis on its radiation monitors and FLUKA simulations to predict radiation levels throughout the CERN accelerator complex. On an individual basis, CERN users can request a more detailed and localized radiation level study that they are interested in. One such request that the simulations in this thesis supplied is given below.

### C.1 Quench protection system system

A larger number of failures in the quench protection system (QPS) [31] leading to beam dumps was observed in 2018 compared to previous years of Run 2 operation in the dispersion suppressor (DS) region of the high luminosity interaction points (IP1 and IP5). This observation triggered a request to the MCWG to analyse the radiation environment that was promptly found to be indeed different due to a change in the annual radiation levels mostly caused by a change in the nominal operational setting of the upstream target collimator long (TCL6) collimator.

Figure C.1 shows the annual total ionizing dose (TID) profile below the beamline in 2017 and 2018, as simulated using FLUKA for the different nominal collimator settings in each year, together with the corresponding radiation monitor (RadMON) TID measurements (in good agreement with the predictions) and showing the positions of the main LHC magnets and QPS racks. This observation is a clear example of the impact that the LHC settings can have on the beam losses and, as a result, on radiation-induced failures in the electronics systems. In addition, it highlights the importance of MCWG monitoring and data analysis, and it should be noted that, as highlighted in the thesis, FLUKA simulations are able to predict such patterns with good accuracy.

*Appendix C Example of a request for radiation level studies*

---

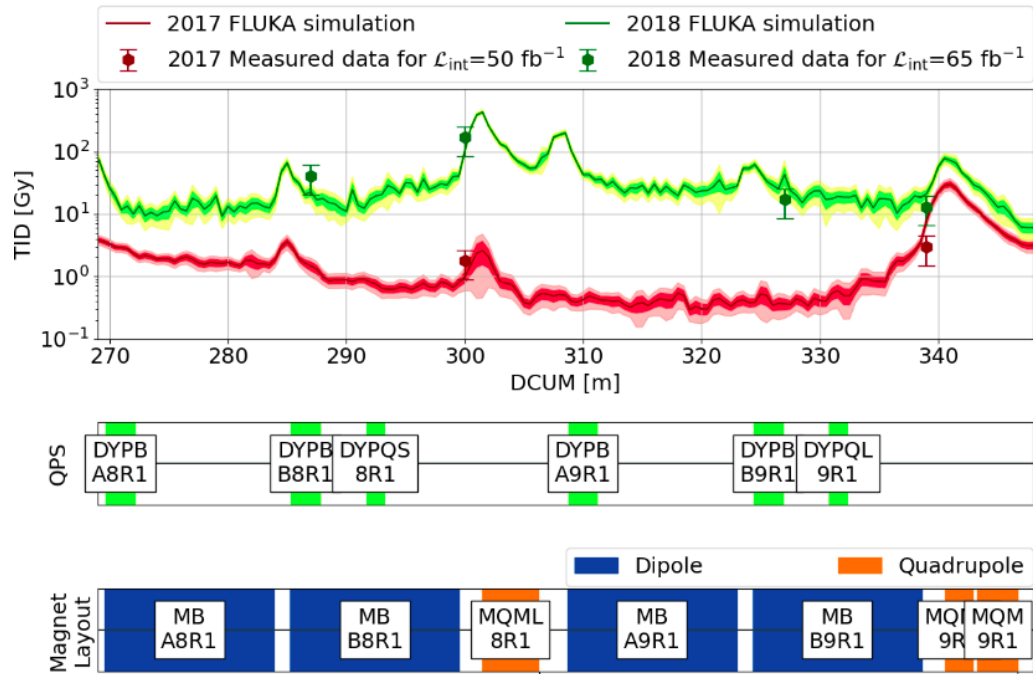


Figure C.1: Annual TID values vs longitudinal position below the beamline in the LHC tunnel in IP1 in 2017 and 2018, from FLUKA simulations and RadMON measurements.

# Bibliography

- [1] O. S. Brüning et al., »LHC Design Report«, CERN Yellow Report, 2004, URL: <https://cds.cern.ch/record/782076>.
- [2] E. Mobs, »The CERN accelerator complex«, 2019, URL: <https://cds.cern.ch/record/2684277>.
- [3] ATLAS Collaboration, »The ATLAS Experiment at the CERN Large Hadron Collider«, in: *JINST* 3 (2008), S08003.
- [4] ALICE Collaboration, »The ALICE Experiment at the CERN LHC«, in: *JINST* 3 (2008), S08002.
- [5] CMS Collaboration, »The CMS Experiment at the CERN LHC«, in: *JINST* 3 (2008), S08004.
- [6] LHCb Collaboration, »The LHCb Detector at the LHC«, in: *JINST* 3 (2008), S08005.
- [7] *ISOLDE website*, URL: <https://home.cern/science/experiments/isolde> (visited on 20th April 2021).
- [8] *ALPHA website*, URL: <https://alpha.web.cern.ch/> (visited on 20th April 2021).
- [9] *nTOF website*, URL: <https://ntof-exp.web.cern.ch/> (visited on 1st July 2021).
- [10] *CERN Annual report 2017*, URL: <http://cds.cern.ch/record/2624296>.
- [11] *CERN Annual report 2018*, URL: <https://cds.cern.ch/record/2671714>.
- [12] *LEP website*, URL: <https://home.cern/science/accelerators/large-electron-positron-collider> (visited on 20th April 2021).
- [13] T. Sykora, »Total, elastic and inelastic pp cross section at the LHC«, August 2016, URL: <https://indico.cern.ch/event/432527/contributions/1072410> (visited on 8th June 2021).
- [14] M. Hostettler, »LHC Luminosity Performance«, 21 June 2018, URL: <https://cds.cern.ch/record/2319396>.
- [15] M. Lamont, »LHC Report: playing with angles«, 2016, URL: <https://cds.cern.ch/journal/CERNBulletin/2016/38/News%5C%20Articles/2216373> (visited on 4th June 2021).
- [16] M. Lamont et al., »Functional specification: LHC MODES.«, in: Tech. rep. 865811 (October 2009), URL: <https://edms.cern.ch/ui/file/865811/1.1/LHC-OP-ES-0005-10-10.pdf>.
- [17] S. Morales Vigo, »Beam Loss Monitors in the Large Hadron Collider«, 8 July 2020, URL: <https://cds.cern.ch/record/2747978>.

- [18] C. Zamantzas, »The Real-Time Data Analysis and Decision System for Particle Flux Detection in the LHC Accelerator at CERN.«, 28 February 2006, URL: <http://cds.cern.ch/record/976628>.
- [19] W. Friesenbichler, »Development of the Readout Electronics for the Beam Loss Monitors of the LHC«, 1 June 2002, URL: <https://cds.cern.ch/record/570940>.
- [20] M. Giovannozzi, »Simple models describing the time-evolution of luminosity in hadron colliders«, June 2014, 5 p, URL: <https://cds.cern.ch/record/1742039>.
- [21] O. Stein et al., »A Systematic Analysis of the Prompt Dose Distribution at the Large Hadron Collider«, in: *Proc. 9th International Particle Accelerator Conference*, JACoW Publishing, 2018, pp. 2036–2038.
- [22] W. Herr and T. Pieloni, »Beam-Beam Effects«, CERN Accelerator School (CAS): Advanced Accelerator Physics Course, 18-29 August 2013, arXiv: 1601.05235, URL: <https://cds.cern.ch/record/1982430>.
- [23] *ATLAS experiment - Public Results - Luminosity*, URL: <https://twiki.cern.ch/twiki/bin/view/AtlasPublic/LuminosityPublicResults> (visited on 6th May 2021).
- [24] *CMS experiment - Public Results - Luminosity*, URL: <https://twiki.cern.ch/twiki/bin/view/CMSPublic/LumiPublicResults> (visited on 6th May 2021).
- [25] M. Karacson, »Evaluation of the Radiation Environment of the LHCb Experiment«, 12 December 2016, URL: <https://cds.cern.ch/record/2243499>.
- [26] M. Calviani, »Updated FLUKA simulations for P8 in support of R2E activities (UX85, US85 and UW85)«, 2011, URL: <https://edms.cern.ch/document/1099674/1.6>.
- [27] M. Oriunno et al., »The Roman Pot for LHC«, 2006, URL: <https://cds.cern.ch/record/1078513>.
- [28] C. Fabjan and K. Hübner, »The Intersecting Storage Rings (ISR): The First Hadron Collider«, in: *Adv. Ser. Direct. High Energy Phys.* 27 (2017), pp. 87–133, URL: <http://cds.cern.ch/record/2312567>.
- [29] ATLAS Collaboration, »The track-based alignment of the ALFA Roman Pot detectors of the ATLAS experiment«, Technical Report, August 2019, URL: <http://cds.cern.ch/record/2688036>.
- [30] *TOTEM website*, URL: <https://totem-experiment.web.cern.ch/> (visited on 20th April 2021).
- [31] L. Coull et al., »LHC magnet quench protection system«, February 1994, URL: <https://cds.cern.ch/record/259538>.
- [32] R. García Alía et al., »LHC and HL-LHC: Present and future radiation environment in the high-luminosity collision points and RHA implications«, in: *IEEE Trans. Nucl. Sci.* 65 (2018), pages 448–456. URL: <https://cds.cern.ch/record/2310128>.

- [33] R. García Alía, »Radiation Fields in High Energy Accelerators and their impact on Single Event Effects.«, 15 December 2014, URL: <https://cds.cern.ch/record/2012360>.
- [34] G. Battistoni et al., »FLUKA Capabilities and CERN Applications for the Study of Radiation Damage to Electronics at High-Energy Hadron Accelerators«, in: *Prog. Nucl. Sci. Tech.* 2 (2011), pp. 948–954.
- [35] A. Apollonio et al., »Lessons Learnt from the 2016 LHC Run and Prospects for HL-LHC Availability«, 2017, URL: <http://cds.cern.ch/record/2289684>.
- [36] Y. Aguiar et al., »Radiation to Electronics Impact on CERN LHC Operation: Run 2 Overview and HL-LHC Outlook«, in: *Proc. 12th International Particle Accelerator Conference* (2021).
- [37] M. Brugger, »R2E and Availability«, in: *Proc. of Workshop on LHC Performance*, CERN Yellow Report, 2014.
- [38] S. Uznanski et al., »Qualification of electronic components for a radiation environment: When standards do not exist — high-energy physics«, October 2017, CERN, URL: <http://cds.cern.ch/record/2765495>.
- [39] E. G. Stassinopoulos and J. P. Raymond, »The space radiation environment for electronics«, in: *Proc. IEEE* (1988), URL: <https://www.osti.gov/biblio/6042035>.
- [40] A. L. Bosser, »Single-event effects from space and atmospheric radiation in memory components«, December 2017, URL: <https://tel.archives-ouvertes.fr/tel-01952831>.
- [41] M. Cecchetto, »Impact of thermal and intermediate energy neutrons on the semiconductor memories for the CERN accelerators«, 10 July 2017, URL: <https://cds.cern.ch/record/2282268>.
- [42] A. Infantino, »FLUKA Monte Carlo Modelling of the CHARM Facility’s Test Area: Update of the Radiation Field Assessment«, September 2017, URL: <https://cds.cern.ch/record/2291683>.
- [43] R. Baumann and E. Smith, »Neutron-induced boron fission as a major source of soft errors in deep submicron SRAM devices«, February 2000, pp. 152–157.
- [44] C. Martinella, »High Energy Hadrons Fluence Measurements in the LHC during 2015, 2016 and 2017 Proton Physics Operations.«, December 2018, URL: <https://cds.cern.ch/record/2652458>.
- [45] A. Coronetti et al., »The Pion Single-Event Effect Resonance and its Impact in an Accelerator Environment«, in: *IEEE Trans. Nucl. Sci.* 67 (2020), pp. 1606–1613, URL: <http://cds.cern.ch/record/2725324>.
- [46] *The LHC Logging Service*, URL: <https://core.ac.uk/download/pdf/44153909.pdf> (visited on 20th April 2021).
- [47] *TIMBER*, URL: <https://twiki.cern.ch/twiki/bin/view/ABPComputing/LhcDataStorage> (visited on 20th April 2021).
- [48] *NXCALS*, URL: <http://nxcals-docs.web.cern.ch/> (visited on 20th April 2021).

- [49] K. Biłko, »Detailed analysis of the evolution and distribution of the total ionising dose in the LHC arc sections during the accelerator operation«, 18 December 2018, URL: <http://cds.cern.ch/record/2652979>.
- [50] E. B. Holzer et al., »Beam loss monitoring system for the LHC«, in: *IEEE Nuclear Science Symposium* 2 (November 2005), pp. 1052–1056.
- [51] M. Kalliokoski et al., »Beam Loss Monitoring for Run 2 of the LHC«, 2015, URL: <http://cds.cern.ch/record/2141806>.
- [52] V. Grishin et al., »A Family of Gas Ionization Chambers and SEM for Beam Loss Monitoring of LHC and Other Accelerators«, in: *Proc. 26th Russian Particle Accelerator Conference, 01-05 October 2018*, JACoW Publishing, pp. 44–48, URL: <http://jacow.org/rupac2018/papers/tuzmh03.pdf>.
- [53] K. Bilko and O. Stein, »Report on the Prompt Dose Distribution Along the LHC Based on BLM Data for proton-proton operation in Run 2«, September 2019, URL: <https://cds.cern.ch/record/2692574>.
- [54] E. Gschwendtner et al., »The Beam loss detection system of the LHC ring«, in: *8th European Particle Accelerator Conference*, June 2002, pp. 1894–1896.
- [55] D. Kramer et al., »Simulations and Measurements of Secondary Electron Emission Beam Loss Monitors for LHC«, in: *Nuclear Physics B - Proceedings Supplements* 172 (2007), Proc. of the 10th Topical Seminar on Innovative Particle and Radiation Detectors, pp. 246–249, URL: <http://www.sciencedirect.com/science/article/pii/S0920563207006056>.
- [56] G. Spiezja et al., »A New RadMon Version for the LHC and its Injection Lines«, in: *IEEE Transactions on Nuclear Science* 61.6 (2014), pp. 3424–3431.
- [57] G. Spiezja et al., »The LHC Radiation Monitoring System - RadMon«, in: *Pro. 10th International Conference on Large Scale Applications and Radiation Hardness of Semiconductor Detectors RD11* (2011).
- [58] C. Martinella et al., »Radiation levels in the LHC during the 2015 Pb-Pb and 2016 p-Pb run and mitigation strategy for the electronic systems during HL-LHC operation«, November 2018, URL: <https://cds.cern.ch/record/2647363>.
- [59] *GIS Machine Map*, URL: <https://gis.cern.ch/gisportal/Machine.htm> (visited on 11th June 2021).
- [60] *GIS Portal*, URL: <https://smb-dep.web.cern.ch/content/maps> (visited on 29th April 2021).
- [61] D. Di Francesca et al., »Distributed Optical Fiber Radiation Sensing in the Proton Synchrotron Booster at CERN.«, in: *IEEE Trans. Nucl. Sci.* 65 (2018), pp. 1639–1644, URL: <https://cds.cern.ch/record/2644042>.
- [62] *iXblue Photonics*, URL: <https://photonics.ixblue.com> (visited on 11th June 2021).
- [63] D. Di Francesca et al., »Radiation Hardened Architecture of a Single-Ended Raman-Based Distributed Temperature Sensor«, in: *IEEE Transactions on Nuclear Science* 64.1 (2017), pp. 54–60, URL: <https://hal.archives-ouvertes.fr/hal-02061611>.

- [64] D. Di Francesca et al., »Dosimetry Mapping of Mixed-Field Radiation Environment Through Combined Distributed Optical Fiber Sensing and FLUKA Simulation«, in: *IEEE Transactions on Nuclear Science* 66.1 (2019), pp. 299–305, URL: <https://ieeexplore.ieee.org/document/8540062>.
- [65] H. Henschel et al., »Fibre optic radiation sensor systems for particle accelerators«, in: *Nucl. Instrum. Meth. A* 526 (2004), pp. 537–550, URL: <https://inspirehep.net/literature/660318>.
- [66] *FLUKA website*, URL: <https://fluka.cern> (visited on 6th April 2021).
- [67] G. Battistoni et al., »Overview of the FLUKA code«, in: *Annals of Nuclear Energy* 82 (2015), pp. 10–18, URL: <http://www.sciencedirect.com/science/article/pii/S0306454914005878>.
- [68] T. T. Böhlen et al., »The FLUKA Code: Developments and Challenges for High Energy and Medical Applications«, in: *Nucl. Data Sheets* 120 (2014), pp. 211–214, URL: <https://cds.cern.ch/record/2109973>.
- [69] S. A. Dupree and S. K. Fraley, »A Monte Carlo Primer: a Practical Approach to Radiation Transport«, Berlin, 2002, URL: <https://cds.cern.ch/record/1100826>.
- [70] A. Capella et al., »Dual parton model«, in: *Phys. Rept.* 236 (1994), pp. 225–329, URL: <https://inspirehep.net/literature/33197>.
- [71] A. Ferrari et al., »The physics of high energy reactions.«, 1998, URL: [https://inis.iaea.org/search/search.aspx?orig\\_q=RN:29067414](https://inis.iaea.org/search/search.aspx?orig_q=RN:29067414).
- [72] A. Ferrari and P. R. Sala, »A new model for hadronic interactions at intermediate-energies for the FLUKA code«, in: *International Conference on Monte Carlo Simulation in High-Energy and Nuclear Physics - MC 93*, 1993, URL: <https://inspirehep.net/literature/367781>.
- [73] A Fasso et al., »FLUKA: performances and applications in the intermediate energy range«, 29 April 1994, URL: <http://cds.cern.ch/record/2724814>.
- [74] K. Haensgen et al., »Monte Carlo simulation of inelastic hadron-hadron reactions in the medium energy range ( $\sqrt{s} < 3$  GeV). Description of the model used and of the Monte Carlo code HADRIN«, 1979.
- [75] A. Ferrari et al., »The production of residual nuclei in peripheral high energy nucleus-nucleus interactions«, in: *Zeitschrift für Physik C: Particles and Fields* 71.1 (March 1996), pp. 75–86, URL: <http://dx.doi.org/10.1007/s002880050149>.
- [76] H. Bethe, »Zur Theorie des Durchgangs schneller Korpuskularstrahlen durch Materie«, in: *Annalen der Physik* 397.3 (1930), pp. 325–400.
- [77] W. H. Barkas et al., »Mass-Ratio Method Applied to the Measurement of  $L$ -Meson Masses and the Energy Balance in Pion Decay«, in: *Phys. Rev.* 101 (January 1956), pp. 778–795, URL: <https://link.aps.org/doi/10.1103/PhysRev.101.778>.
- [78] F. Bloch, »Zur Bremsung Rasch Bewegter Teilchen beim Durchgang durch Materie«, in: *Annalen Phys.* 408 (1933), pp. 285–320.

- [79] N. F. Mott, »The Scattering of Fast Electrons by Atomic Nuclei«, in: *Sir Nevill Mott – 65 Years in Physics*, 1929, pp. 13–30.
- [80] J. F. Ziegler et al., *The stopping and range of ions in solids*, English, Pergamon New York, 1985.
- [81] R. M. Sternheimer et al., »Density Effect for the Ionization Loss of Charged Particles in Various Substances«, in: *Atom. Data Nucl. Data Tabl.* 30 (1984), pp. 261–271.
- [82] M. Brugger et al., »LHC Accelerator Design Studies on the Example of Passive Absorbers«, in: *Nuclear Technology* 168.3 (2009), pp. 659–664.
- [83] K. Roeed et al., »Method for Measuring Mixed Field Radiation Levels Relevant for SEEs at the LHC«, in: *IEEE Transactions on Nuclear Science* 59.4 (2012), pp. 1040–1047.
- [84] V. Vlachoudis, »FLAIR: A powerful but user friendly graphical interface for FLUKA«, April 2009, URL: <https://cds.cern.ch/record/2749540>.
- [85] *FLAIR website*, URL: <https://flair.web.cern.ch/flair/> (visited on 29th April 2021).
- [86] *GEANT4 website*, URL: <https://geant4.web.cern.ch/node/1> (visited on 29th April 2021).
- [87] S. Agostinelli et al., »Geant4—a simulation toolkit«, in: *Nuclear Instruments and Methods in Physics Research Section A: Accelerators, Spectrometers, Detectors and Associated Equipment* 506.3 (2003), pp. 250–303, URL: <https://www.sciencedirect.com/science/article/pii/S0168900203013688>.
- [88] J. Allison et al., »Geant4 developments and applications«, in: *IEEE Transactions on Nuclear Science* 53.1 (2006), pp. 270–278.
- [89] J. Allison et al., »Recent developments in Geant4«, in: *Nuclear Instruments and Methods in Physics Research Section A: Accelerators, Spectrometers, Detectors and Associated Equipment* 835 (2016), pp. 186–225, URL: <https://www.sciencedirect.com/science/article/pii/S0168900216306957>.
- [90] Nuclear Energy Agency, *PENELOPE 2018: A code system for Monte Carlo simulation of electron and photon transport*, 2019, URL: <https://www.oecd-ilibrary.org/content/publication/32da5043-en>.
- [91] A. Mereghetti et al., »The FLUKA LineBuilder and Element DataBase: Tools for Building Complex Models of Accelerator Beam Lines«, in: *Proc. 3rd International Conference on Particle accelerator C1205201* (2012), pp. 2687–2689.
- [92] *CERN Drawing Directory website*, URL: <https://edms-service.web.cern.ch/cdd/> (visited on 29th April 2021).
- [93] *TWISS files website*, URL: <https://twiki.cern.ch/twiki/bin/view/Sandbox/20TwissFileProduction> (visited on 29th April 2021).
- [94] *CERN Layout Database*, URL: <https://layout.cern.ch/> (visited on 29th April 2021).

- [95] J. Mekki et al., »CHARM: A Mixed Field Facility at CERN for Radiation Tests in Ground, Atmospheric, Space and Accelerator Representative Environments«, in: *IEEE Trans. Nucl. Sci.* 63.4 (2016), pp. 2106–2114.
- [96] C. Cazzaniga et al., »Study of the Deposited Energy Spectra in Silicon by High-Energy Neutron and Mixed Fields«, in: *IEEE Trans. Nucl. Sci.* 67.1 (2020), pp. 175–180.
- [97] M. Cecchetto et al., »SEE Flux and Spectral Hardness Calibration of Neutron Spallation and Mixed-Field Facilities«, in: *IEEE Trans. Nucl. Sci.* 66 (2019), pp. 1532–1540, URL: <https://cds.cern.ch/record/2757331>.
- [98] T. Oyama et al., »Measurement and calculation of thermal neutrons induced by the 24GeV/c proton bombardment of a thick copper target«, in: *Nuclear Instruments and Methods in Physics Research Section B: Beam Interactions with Materials and Atoms* 434 (2018), pp. 29–36, URL: <https://www.sciencedirect.com/science/article/pii/S0168583X18304828>.
- [99] E. Lee et al., »Energy spectra of neutrons penetrating concrete and steel shielding blocks from 24 GeV/c protons incident on thick copper target«, in: *Nuclear Instruments and Methods in Physics Research Section A: Accelerators, Spectrometers, Detectors and Associated Equipment* 998 (March 2021), pp. 165–189.
- [100] T. Oyama et al., »Measurements of secondary-particle emissions from copper target bombarded with 24-GeV/c protons«, in: *Nuclear Instruments and Methods in Physics Research Section A: Accelerators, Spectrometers, Detectors and Associated Equipment* 990 (2021), URL: <https://www.sciencedirect.com/science/article/pii/S0168900220313747>.
- [101] A. Thornton, »CHARM Facility Test Area Radiation Field Description«, April 2016, URL: <https://cds.cern.ch/record/2149417>.
- [102] *CHARM Online Toolkit*, URL: <https://charmtoolkit.web.cern.ch/integral/> (visited on 13th July 2021).
- [103] R. Garcia Alia et al., »SEL Hardness Assurance in a Mixed Radiation Field«, in: *IEEE Trans. Nucl. Sci.* 62.6 (2015), pp. 2555–2562.
- [104] *X-Ray Mass Attenuation Coefficients*, URL: <https://www.nist.gov/pml/x-ray-mass-attenuation-coefficients> (visited on 29th April 2021).
- [105] P. G. Young and D. G. Foster Jr., »Evaluation of the neutron and gamma-ray production cross sections for nitrogen«, in: *Tech. Rep. Los Alamos Sci. Lab.* (1972).
- [106] E. Bougamont et al., »Neutron spectroscopy with the Spherical Proportional Counter based on nitrogen gas«, in: *Nucl. Instrum. Meth. A* 847 (2017), pp. 10–14.
- [107] M. Marzo et al., »RadFET dose response in the CHARM mixed-field: FLUKA MC simulations«, in: *EPJ Nuclear Sci. Technol.* 3 (2017), URL: <https://cds.cern.ch/record/2314945>.
- [108] I. Toccafondo, »Distributed Optical Fiber Radiation and Temperature Sensing at High Energy Accelerators and Experiments«, 15 October 2015, URL: <https://cds.cern.ch/record/2221650>.

- [109] A. Tsinganis, »LHC Collimation Working Group #216: Energy deposition from collision debris in the LHC and HL-LHC«, URL: <https://indico.cern.ch/event/629210/> (visited on 13th June 2021).
- [110] A. Tsinganis, »LHC Collimation Working Group #226: Impact of roman pot and TCL settings on radiation levels in the LHC matching section«, URL: <https://indico.cern.ch/event/677406/> (visited on 13th June 2021).
- [111] V. Boccone et al., »Beam-machine Interaction at the CERN LHC«, in: *Nuclear Data Sheets* 120 (2014), pp. 215–218, URL: <https://www.sciencedirect.com/science/article/pii/S009037521400502X>.
- [112] A. Lechner et al., »Validation of energy deposition simulations for proton and heavy ion losses in the CERN Large Hadron Collider«, in: *Phys. Rev. Accel. Beams* 22 (7 July 2019), URL: <https://link.aps.org/doi/10.1103/PhysRevAccelBeams.22.071003>.
- [113] H. Burkhardt and I. Efthymiopoulos, »Chapter 8: Interface with Experiments. Interface with Experiments«, May 2017, pp. 157–160. URL: <https://cds.cern.ch/record/2120714>.
- [114] A. Tsinganis and F. Cerutti, »Impact of Collision Debris in the HL-LHC ATLAS and CMS Insertions«, in: *Proc. 8th International Particle Accelerator Conference* (2017), URL: <https://cds.cern.ch/record/2289480>.
- [115] G. Battistoni et al., »FLUKA Capabilities and CERN Applications for the Study of Radiation Damage to Electronics at High-Energy Hadron Accelerators«, in: *Progress in Nuclear Science and Technology* 2 (October 2011), pp. 948–954.
- [116] W. Heisenberg, »Über den anschaulichen Inhalt der quantentheoretischen Kinematik und Mechanik«, in: *Zeitschrift für Physik* 43.3 (March 1927), pp. 172–198.
- [117] *Stanford Linear Accelerator (SLAC)*, URL: <https://www6.slac.stanford.edu/> (visited on 12th December 2020).
- [118] F. Hinterberger, »Electrostatic accelerators«, 2006, URL: <https://cds.cern.ch/record/1005042>.
- [119] W. Herr and B. Muratori, »Concept of luminosity«, 2006, URL: <http://cds.cern.ch/record/941318>.
- [120] *Magnetic field of an idealized quadrupole with forces*, URL: [https://en.wikipedia.org/wiki/File:Magnetic\\_field\\_of\\_an\\_idealized\\_quadrupole\\_with\\_forces.svg](https://en.wikipedia.org/wiki/File:Magnetic_field_of_an_idealized_quadrupole_with_forces.svg) (visited on 12th December 2020).
- [121] *Magnetic multipoles*, URL: [https://www.lhc-closer.es/taking\\_a\\_closer\\_look\\_at\\_lhc/0.magnetic\\_multipoles](https://www.lhc-closer.es/taking_a_closer_look_at_lhc/0.magnetic_multipoles) (visited on 12th December 2020).
- [122] S. Redaelli, »Beam Cleaning and Collimation Systems«, Joint International Accelerator School: Beam Loss and Accelerator Protection, 5-14 Nov 2014, URL: <http://cds.cern.ch/record/2207182>.
- [123] E. Skordis et al., »FLUKA coupling to Sixtrack«, CERN Yellow Report, 2020, URL: <http://cds.cern.ch/record/2694313>.

- [124] A. Verdier, »The LHC IR6 optics«, June 1998, URL: <https://cds.cern.ch/record/691998>.
- [125] L Bruno et al., »LHC Beam Dump Design Study - Part III : Off-normal operating conditions«, CERN, February 2000, URL: <https://cds.cern.ch/record/691838>.



# List of Abbreviations

**ATS** Accelerators and Technology Sector. 46

**BLM** Beam Loss Monitor. 33–35, 40, 43, 44, 46–49, 57, 61, 72–82, 89, 93, 97, 98, 125

**CALS** CERN Accelerators Logging Service. 33

**CCD** Charged-Coupled device. 24, 25

**CERN** European Organisation for Nuclear Research. iii, iv, 1, 3–5, 21, 25, 33, 35–37, 40, 41, 43, 101, 109, 125

**CHARM** CERN High Energy AcceleratoR Mixed-field. iv, 2, 37, 43, 44, 46, 47, 49, 52–56, 58, 75, 82, 83, 89, 93, 97

**CMOS** Complementary MOS. 24, 25

**COTS** Commercially Off-The-Shelf. 1, 18, 22, 25

**CPU** Central Processing Unit. 58

**DD** Displacement Damage. 25, 35

**DDD** Displacement Damage Dose. 25

**DPM** Dual Parton Model. 39

**DS** Dispersion Supressor. iv, 5, 11, 17, 18, 23, 37, 47, 61, 65, 66, 75, 79, 98, 109

**ELDRS** Enhanced Low Dose Rate Sensitivity. 25

**fedb** FLUKA Element DataBase. 40

**FLUKA** FLUkturiende KAskade. 1, 37–41, 43, 44, 46, 49–56, 58, 59, 61, 62, 66, 70, 72, 74–80, 82–86, 88, 89, 92, 94–98, 109, 110, 125

**GINC** Generalized IntraNuclear Cascade. 39

**HEH** High Energy Hadron. 26–29, 31, 37, 49, 97, 98

**HEHeq** High Energy Hadron equivalent. 29–31, 35–37, 51, 52, 61, 63, 66, 86, 89–91, 93

**HL-LHC** High Luminosity LHC. 21–23

**IC** Ionization Chamber. 35

**IP** Interaction Point. 1–3, 5, 7, 9, 11, 13, 14, 16, 17, 23, 33, 37–39, 47, 61, 62, 70, 72–80, 82–86, 88, 89, 92, 94, 96, 98, 105, 109, 110

**IR** Insertion Region. 3, 5, 6, 11, 16, 17, 19, 34, 93, 96, 105, 107

**ISR** Intersecting Storage Rings. 18

**IT** Inner Triplet. 16, 17, 77

**LB** LineBuilder. 40

**LDB** Logging DataBase. 33, 41

**LEP** Large Electron-Positron. 5, 100, 103

**LET** Linear Energy Transfer. 26

**LHC** Large Hadron Collider. iii, iv, 1–3, 5–7, 9–13, 15–19, 21–23, 26, 28, 30, 31, 33–38, 40, 43, 46, 47, 49, 53, 58, 61, 63, 64, 66–72, 74, 75, 78, 83, 86–88, 92, 93, 95–98, 100, 101, 103, 105–107, 109, 110

**LIC** Little Ionization Chamber. 35

**LS** Long Shutdown. 12, 19, 23

**LSS** Long Straight Section. iv, 5, 11, 16–18, 61, 66, 75–80, 98

**MC** Monte Carlo. 37, 38

**MCWG** Monitoring and Calculation Working Group. 1, 33, 94, 109, 125

**MOS** Metal Oxide Semiconductor. 24

**NMOS** N-channel MOS. 24

**NXCALS** New CALS. 33

**OF** Optical Fibre. 37, 43, 58, 61, 82, 83, 95

**PMOS** P-channel MOS. 24

**POT** Proton On Target. 46, 48

**PS** Proton Synchrotron. 37, 44

**PSB** Proton Synchrotron Booster. 36, 82

**QPS** Quench Protection System. 18, 22, 23, 109

**R2E** Radiation to Electronics. iii, 1, 10, 21–23, 28, 30, 33, 36, 40, 43, 46, 49–52, 61, 92, 94, 96, 125

**rad** radiation absorbed dose. 24

**RADFET** RADiation-sensitive metal-oxide-silicon Field-Effect Transistor. 53–56, 59, 84, 97, 98

**RadMON** Radiation Monitor. v, 33, 35, 36, 43, 44, 49–57, 61, 66, 73, 84–91, 93, 97, 98, 109, 110

**RF** Radio Frequency. 5, 105

**RHA** Radiation Hardness Assurance. 21, 23, 26

**RMS** Root Mean Square. 7

**RP** Roman Pot. 18, 70

**RS** Running Sum. 34

**SEE** Single Event Effects. 26, 28–31, 40, 43, 52, 66, 73, 88, 97

**SEM** Secondary Emission Monitor. 35

**SEU** Single Event Upsets. 35, 86

**SPS** Super Proton Synchrotron. 5, 17, 37, 40

**SRAM** Static Random-Access Memory. 28, 35

**STD** Standard Deviation. 75

**TCL** Target Collimator Long. 17, 18, 66, 70, 72, 73, 75–80, 85, 86, 90, 91, 109

**THN** Thermal Energy Neutrons. 30, 36, 37, 63, 86, 97

**TID** Total Ionizing Dose. 24–27, 34–37, 45, 46, 48, 49, 53–59, 61–64, 72–75, 77, 78, 82–86, 93, 95, 97, 98, 109, 110

**TIMBER** Timeseries Information Masteing: Browsing, Extraction and Rendering. 33

**TNID** Total Non-Ionizing Dose. 25

**TS** Technical Stop. 70



# Acknowledgements

First of all, I would like to thank Dr. Giuseppe Lerner, my CERN supervisor, for contributing with his knowledge and expertise to the preparation of this work. From the very beginning, he made me feel completely free to conduct my research as I wanted and encouraged me to expand my horizons. Our exchanges were always rewarding and helpful, especially when combined with his characteristic loquaciousness and a talent for storytelling.

My second humble thanks go Apl. Prof. Dr. rer. nat. habil. Hubert Kroha, who supported me with the official work required to the completion of my Master Thesis from the Technical University of Munich. I would also like to thank Prof. Dr. sc. nat. Peter Fierlinger for being my second reader. I am gratefully indebted for their very valuable comments on this thesis.

It goes without saying that the interactions with all the projects involved in this work would not have been possible if it had not been for Dr. Ruben Garcia Alia, the R2E project leader, who always knew where to direct me for more information and which exciting project to investigate next.

The weekly MCWG meetings provided me with valuable input on the measured data. In particular, Kacper Bilko for his help regarding the BLM data analysis and plotting the LHC layout and Diego Di Francesca for the optical fibre discussions and data.

On the FLUKA side, I would not have been able to progress as smoothly as I did without the valuable input from Marta Sabate Gilarte and Francesco Cerutti.

I would also like to acknowledge the CHARM team, in particular Matteo Brucoli and Salvatore Danzeca for the RadMON data, and the Radio Protection group, in particular Angelo Infantino, for the discussions about the CHARM modelling and thermal neutrons.

I would also like to thank my colleagues from the SY-STI-BMI section for making me feel at home and turning my stay at CERN into one of the best experiences I ever had. Amongst many, I cannot miss Andre, with whom I virtually shared the office for more than one year, and Mario, my trusty running buddy.

Gabriela is my greatest discovery at CERN, and no one knows me like you do. Thank you for being always there for me and for making my days more exciting. It would not have been the same without you and I am really fortunate to have you by my side.

Last, but not least, I would like to thank the most supportive family in the world, Adrian, Mărioara and Gheorghe Prelipcean. Despite the distance, I always knew that you were there if needed. My biggest wish is to share with you my enthusiasm for science.